TECHNISCHE UNIVERSITÄT
ILMENAU

Fakultät für Mathematik und Naturwissenschaften
Institut für Physik

Two-Dimensional Materials on Metal Surfaces: Impact on Molecular Frontier Orbitals, Vibrons and on the Moiré Effect

Dissertation zur Erlangung des akademischen Grades
Dr. rer. nat. (doctor rerum naturalium)

Eingereicht von:	Alexander Mehler geboren am: 15.09.1992
1. Gutachter:	Prof. Dr. Jörg Kröger
2. Gutachter:	Prof. Dr. Yuriy Dedkov
3. Gutachter:	Prof. Dr. Stefan Krischok

Eingereicht am:	10.03.2021
Tag der wissenschaftlichen Aussprache:	29.04.2021

urn:nbn:de:gbv:ilm1-2021000107

Abstract

This dissertation investigates the growth of the two-dimensional materials graphene and hexagonal boron nitride (h-BN) on the metallic substrates Pt(111) and Ru(0001), as well as the interaction of organic molecules with these respective surfaces, using a scanning tunneling microscope (STM).

First, the growth of the two-dimensional materials graphene and h-BN on the two metallic samples Pt(111) and Ru(0001) is investigated. Here, a chemical vapor deposition (CVD) method using ethylene as a precursor for graphene growth and an alternative temperature programmed growth (TPG) method for the growth of h-BN using ammonia borane as a precursor are explored. The observed structural properties of both two-dimensional materials on the metallic substrates are discussed.

On the basis of those findings a flexible method for the growth of graphene/h-BN heterostructures is presented. The heterostructure is analyzed and a model with distinct twist angles between the atomic layers is developed on basis of the experimental observations. Imaging the heterostructure with reduced tip-sample distance reveals an additional hexagonal superstructure. In order to validate the experimental results, density functional theory (DFT) calculations of the graphene/h-BN heterostructure are performed and compared to the STM data.

Subsequently, spectroscopic signatures of the frontier orbitals of the organic molecule dibenzotetraphenylperiflanthene (DBP) adsorbed on graphene and h-BN on Pt(111) and Ru(0001) are analyzed. Changes in the energetic position of the frontier orbitals of DBP are used to probe the work function modulation over different parts of the moiré on h-BN. For h-BN on Pt(111), DBP frontier orbital energies exhibit a common shift that leaves the gap between the orbitals invariant and reflects local work function changes of the h-BN lattice the molecule is weakly coupled to. In contrast, h-BN on Ru(0001) leads to a nonuniform behavior of the frontier orbital energies, which is tentatively attributed to additional charge transfer processes between the molecule and the surface. The efficient reduction in hybridization between DBP and the metallic substrates by the two-dimensional buffer layers graphene and h-BN is explored further. Both two-dimensional materials enable the observation of the Franck-Condon effect

in both frontier orbitals. On h-BN, vibronic progression with two vibrational energies gives rise to sharp orbital sidebands that are clearly visible up to the second order of the vibrational quantum number with different Huang-Rhys factors. In contrast, on graphene, orbital and vibronic spectroscopic signatures exhibit broader line shapes, with the second-order progression being hardly discriminable. Only a single vibrational quantum energy leaves its fingerprint in the Franck-Condon spectrum.

Zusammenfassung

In der vorliegenden Arbeit wird das Wachstum der zweidimensionalen Materialien Graphen und hexagonales Bornitrid (h-BN) auf den beiden metallischen Oberflächen Pt(111) und Ru(0001), sowie die Interaktion eines organischen Moleküls mit diesen Probenoberflächen, mit Hilfe eines Rastertunnelmikroskops untersucht.

Zuerst wird das Wachstum und die strukturellen Eigenschaften von Graphen und h-BN auf beiden metallischen Oberflächen beleuchtet. Dabei wird eine chemische Gasphasenabscheidungsmethode (CVD) mit dem Ausgangsstoff Ethen für das Graphenwachstum und eine alternative temperaturregulierte Wachstumsmethode (TPG) für das h-BN-Wachstum mit dem Ausgangsstoff Amminboran verwendet. Die beobachteten strukturellen Eigenschaften beider zweidimensionaler Materialen auf den jeweiligen Metalloberflächen werden diskutiert und verglichen.

Auf Grundlage dieser Ergebnisse wird ein Verfahren zum Wachstum von Heterostrukturen bestehend aus Graphen und h-BN entwickelt. Die Heterostruktur wird analysiert und ein Modell mit festgelegter Rotation zwischen den einzelnen atomaren Lagen auf der Basis der experimentellen Beobachtungen erstellt. Während der Aufnahme von STM-Bildern mit verringertem Spitzen-Proben-Abstand kann eine zusätzliche hexagonale Struktur abgebildet werden. Zum Vergleich mit den experimentellen Daten wurden Dichtefunktionaltheorierechnungen (DFT) der Graphen/h-BN-Heterostruktur durchgeführt.

Anschließend werden die spektroskopischen Signaturen der Molekülorbitale des organischen Moleküls Dibenzotetraphenylperiflanthen (DBP), welches auf Graphen bzw. h-BN auf Pt(111) und Ru(0001) adsorbiert wird, miteinander verglichen. Veränderungen der Energie der Molekülorbitale von DBP werden genutzt, um Austrittarbeitsveränderungen auf verschiedenen Teilen des h-BN-Moirés zu beschreiben. Die Lücke der beiden Molekülorbitale bleibt auf verschiedenen Adsorptionsplätzen auf h-BN-bedecktem Pt(111) unverändert, während sich die absolute Energie der Molekülorbitale gleichermaßen verschiebt. Im Gegensatz dazu ist die Energieveränderungen der Molekülorbitale auf h-BN-bedecktem Ru(0001) nicht gleichförmig, was mit einem möglichen Ladungstransfer

zu begründen sein könnte. Die effiziente Reduzierung der Hybridisierung zwischen DBP und den Metalloberflächen mit Hilfe der zweidimensionalen Pufferschichten Graphen und h-BN wird weiter untersucht. Beide zweidimensionalen Materialen sorgen dafür, dass Franck-Condon-Anregungen in beiden Molekülorbitalen zu beobachten sind. Auf h-BN sind Schwingungsprogressionen mit zwei Vibrationsenergien mit verschiedenen Huang-Rhys-Faktoren und scharfen Vibrationsseitenbändern bis zur zweiten Vibrationsordnung zu sehen. Im Gegensatz dazu sind die Orbital- und Vibrationsspektrallinien auf Graphen breiter, wodurch die zweite Vibrationsprogression nicht mehr zu erkennen ist. In diesem Fall trägt also nur eine Vibrationsmode zum Franck-Condon-Spektrum bei.

Contents

CHAPTER 1

Introduction

The development of the scanning tunneling microscope (STM) allows for the investigation of nature's building blocks which are single atoms and molecules [1]. Utilizing this technique, conductive sample surfaces can be imaged and manipulated with atomic precision, while scanning tunneling spectroscopy (STS) probes electronic properties on the nanoscale. Those technological advancements led to novel endeavors in the field of magnetism [2], superconductivity [3, 4], optical [5] and vibrational [6] properties investigated on the single atom and single molecule level.

The significance of those observations becomes clear by taking a look at the development of the size of transistors in electronic compounds, which is shrinking over the last decades from a few microns to 5 nm in recent commercially available microprocessors [7]. Therefore, surface, single atom and single molecule properties will become more and more relevant in the ongoing technical development in electronics down to the dimensions of a few atoms.

Another relevant field is the development of organic light emitting diodes (OLED) and energy storage devices, where surface properties become important due to an ongoing miniaturization. Different organic molecules have been explored as donor-acceptor molecules for technical applications in OLEDs, where the knowledge of the molecular energy landscape is an important prerequisite for the construction of efficient devices [8, 9]. In order to improve the performance of lithium-ion and sodium-ion batteries, carbonyl-based organic electodes

have been explored as they are flexible and cheap alternatives to commonly used inorganic materials [10].

As evident by the small selection of examples and ongoing miniaturization down to the nanoscale, it is important to understand the properties of single molecules and atoms for their utilization in technical applications. Genuine molecular characteristics often get quenched upon adsorption on the metallic surface and consequentially additional experimental considerations have to be made. To probe those single atom and single molecule properties in a nearly free state, *i.e.*, with reduced coupling to the sample surface, decoupling layers have been used extensively in recent years. Prominent examples are graphene [11, 12], hexagonal boron nitride (h-BN) [13–15], oxide layers [5, 16] and transition metal dichalcogenides (TMDC) [17, 18].

Graphene is characterized by a high electron mobility, a high thermal conductivity and a high tensile strength. Its first production in laboratory conditions sparked a huge research interest due to its unique properties [19–21]. The band structure of graphene consists of linear dispersing π-bands around the K-point of the Brillouin zone, resulting in a zero-bandgap semiconductor.

While in comparison to graphene, hexagonal boron nitride (h-BN) has the same honeycomb structure, albeit with a $\approx 1.6\,\%$ larger lattice constant [22], its electronic properties differ a lot as h-BN is an insulator with a bandgap of 6 eV [23, 24]. Due to its similar structural appearance, h-BN is sometimes refereed to as "white graphene" [25].

Besides its use as a buffer layer for molecues, h-BN is used as an insulating layer in field effect transistors [26]. Additionally, graphene has been utilized to improve the performance of lithium-ion and sodium-ion batteries [27–29]. Minaturized energy storage devices (MESD) have been developed out of stacked two-dimensional materials to create on-chip microsystems [30]. The field of stacked bilayers of graphene [31] and heterostructures of graphene and hexagonal boron nitride (h-BN) emerges in recent studies and will be of future research interest as their physical properties can be altered by introducing a twist angle between both layers [32].

This dissertation investigates the growth of the two-dimensional materials graphene and h-BN on the metallic substrates Pt(111) and Ru(0001) using a scanning tunneling microscope (STM). A flexible method for the growth of

graphene/h-BN heterostructures is explored. Further, an organic molecule adsorbed on graphene and h-BN is probed by comparing the changes in electronic and vibrational characteristics of the molecule on the different sample surfaces.

The outline of the thesis is as follows:

Chapter 2 explains the relevant basics of the experimental setup and also gives a brief overview of the used theoretical framework.

Chapter 3 explores the growth of the two-dimensional materials graphene and h-BN on the two metallic samples Pt(111) and Ru(0001). Here a CVD method using ethylene as a precursor and an alternative TPG method for the growth of h-BN with borazane as the precursor molecule is presented. The observed structural properties of both two-dimensional materials on the metallic substrates are discussed.

Chapter 4 displays a cheap and flexible method for the growth of heterostructures of graphene and h-BN. The heterostructure is analyzed and a model with different twist angles between the atomic layers is developed on basis of the experimental observations. In order to validate the experimental results, DFT calculations of the graphene/h-BN heterostructure were performed and compared to the STM data.

Chapter 5 presents spectroscopic measurements of the orbital structure of the organic molecule DBP adsorbed on graphene and h-BN on Pt(111) and Ru(0001). Changes in the energetic position of the frontier orbitals of DBP are used to probe the work function modulation over different parts of the h-BN moiré. The efficient reduction in hybridization between DBP and the metallic substrates by the two-dimensional buffer layers graphene and h-BN is investigated. Differences in vibrational excitations of DBP upon adsorption on graphene and h-BN are observed and discussed.

CHAPTER 2

Experimental Methods

2.1 Scanning Tunneling Microscopy

The scanning tunneling microscope (STM) is a very powerful tool to explore structural and electronic properties of surfaces and interfaces. Its main working principle originates from the quantum mechanical tunneling effect, where an electron can tunnel through a vacuum barrier between tip and sample as a result of the finite overlap of the wave function of the tip with states of the metallic substrate. A finite voltage is applied to the junction and the current response is controlled by an external feedback loop, as shown in Figure 2.1.

One-dimensional potential barrier

The vacuum barrier can be described by a one-dimension potential barrier of height V_0 and width d [33]. The stationary Schrödinger equation

$$\frac{\hbar^2}{2m}\frac{\partial^2}{\partial z^2}\Psi(z) = [V(z) - E]\Psi(z) \tag{2.1}$$

is then solved for the following wave functions in their respective regions of the barrier as shown in Figure 2.1(b):

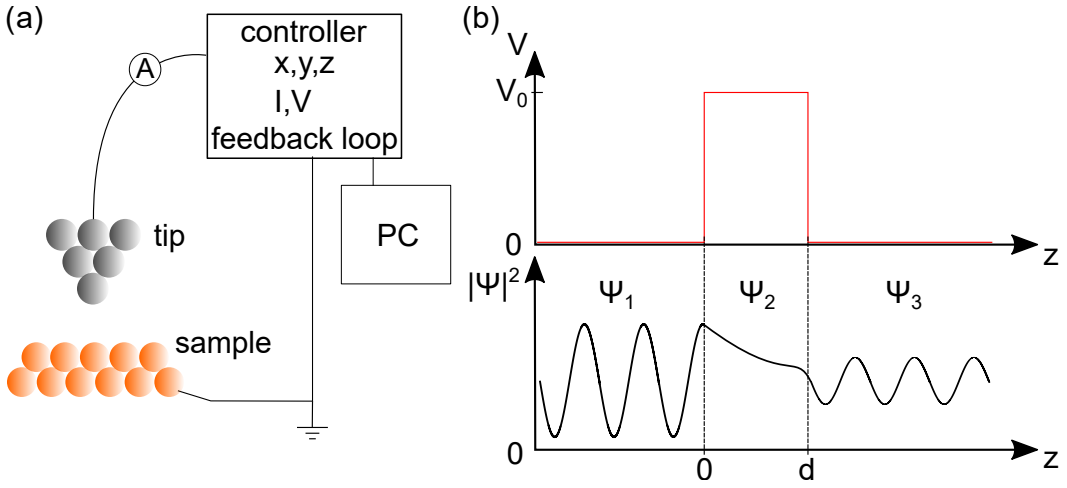

Figure 2.1: (a) Sketch of the basic working principle of the scanning tunneling microscope. The tip, the sample and the control unit are shown. The bias voltage is applied to the sample. During the scan the current is controlled via an automated adjustment of the tip-sample distance z by an external feedback loop. (b) Schematic representation of a one-dimensional vacuum barrier (red) with barrier height V_0. The evolution of the wave function of the electron Ψ_k ($k = 1, 2, 3$) is qualitatively shown in all three regions of the barrier.

$$\Psi_1(z) = Ae^{ikz} + Be^{-ikz} \qquad z < 0 \tag{2.2}$$

$$\Psi_2(z) = Ce^{i\kappa z} + De^{-i\kappa z} \qquad 0 \leq z \leq d \tag{2.3}$$

$$\Psi_3(z) = Fe^{ikz} \qquad z > d \tag{2.4}$$

With the wave numbers

$$k = \sqrt{\frac{2mE}{\hbar^2}} \tag{2.5}$$

$$\kappa = \sqrt{\frac{2m(V_0 - E)}{\hbar^2}} \tag{2.6}$$

The amplitude of the incoming wave A is set to unity. The coefficients B, C, D, F can be calculated through the continuity conditions at $z = 0$ and $z = d$. The transmission probability T for an electron tunneling through the

barrier is then given by

$$T = |F|^2 = \frac{4k^2\kappa^2}{(k^2+\kappa^2)^2 sinh^2(\kappa d) + 4k^2\kappa^2} \tag{2.7}$$

In the limit $\kappa d >> 1$ the probability of transmission can be approximated by

$$T \approx \frac{16k^2\kappa^2}{(k^2+\kappa^2)^2} e^{-2\kappa d} = \frac{16E(V_0-E)}{V_0^2} exp\left[-2d\sqrt{\frac{2m}{\hbar^2}(V_0-E)}\right] \tag{2.8}$$

The amplitude of the wave function of the electron $\Psi(z)$ with energy E is therefore exponentially decaying in the barrier.

Bardeen Model and Energy-Dependent Approximation

The schematic setup of an STM is shown in Figure 2.1(a). A bias voltage is applied to the junction in such way that for positive voltages electrons tunnel from the tip to the surface. As a consequence of the applied bias voltage the fermi levels of the two leads get shifted with respect to each other resulting in a flow of electrons between the two electrodes (Figure 2.2). Bardeen derived the transition rate between the two electrodes from an initial state i of the tip to a final state s of the sample using Fermi's golden rule [33, 34] as

$$\omega_{t,i\to s,f} = \frac{2\pi}{\hbar}|M_{fi}|^2 \delta(E_{s,f} - E_{t,i}) \tag{2.9}$$

with the matrix element M_{fi} calculated as

$$M_{fi} = \frac{\hbar^2}{2m}\int_{S_{t,s}} \left[\Psi_{t,i}(r)\nabla\Psi^*_{s,f}(r) - \Psi^*_{s,f}(r)\nabla\Psi_{t,i}(r)\right] dS \tag{2.10}$$

over an arbitrary tip-sample surface $S_{t,s}$. The current then can be found by summation over all pairs of initial and final states, multiplication with the electron charge and taking the factor 2 due to spin degeneracy into account:

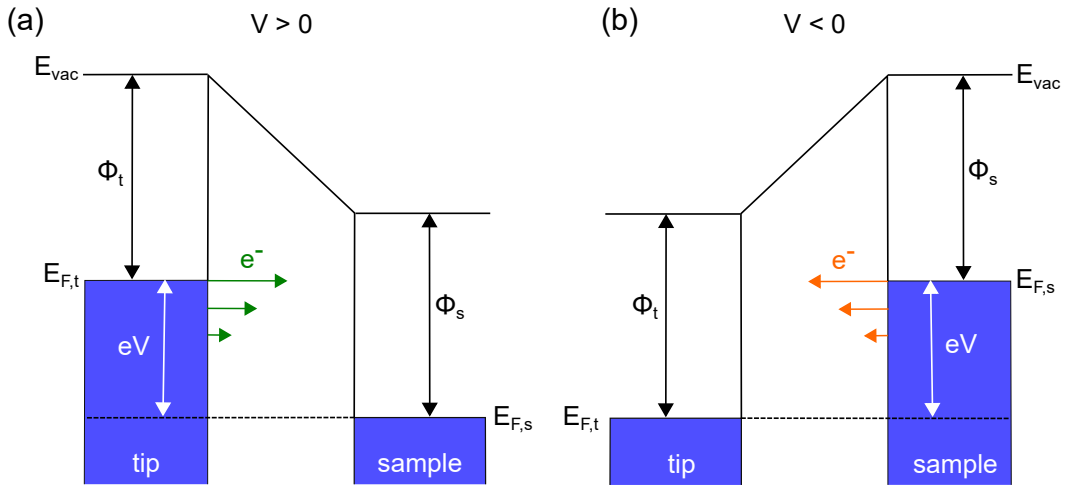

Figure 2.2: Representation of the STM tunneling junction at a bias voltage V. Tip and sample are separated by the vacuum barrier with trapezoidal shape. The work function $\Phi_{t,s}$ is the energy difference between vacuum energy E_{vac} and fermi level of tip and sample, respectively. The density of states for tip and sample are schematically shown as constant. The arrows indicate the direction of the tunneling electrons with their size indicating the contribution at certain energies. (a) At positive bias voltages $V > 0$ electrons tunnel from the tip to the sample. (b) At negative bias voltages $V < 0$ electrons tunnel from the sample to the tip.

$$I = \frac{4\pi e}{\hbar} \sum_{i,f} |M_{fi}|^2 \delta(E_{s,f} - E_{t,i}) \tag{2.11}$$

Replacing the dependence of the wave functions by a dependence on the energy and introducing the density of states ρ for the two electrodes the current can be written as:

$$I(V) = \frac{4\pi e}{\hbar} \int_0^{eV} \rho_s(\epsilon)\rho_t(\epsilon - eV)|M(\epsilon)|^2 d\epsilon \tag{2.12}$$

The tunneling matrix elements $|M(\epsilon)|^2$ describes the transmission probability T of the electron tunneling through the barrier. This transmission factor can be expressed in the one-dimensional Wentzel-Kramers-Brillouin approximation [35] as

$$T \approx |M(\epsilon)|^2 = exp\left[-2d\sqrt{\frac{2m}{\hbar^2}(\Phi + \frac{eV}{2} - \epsilon)}\right]. \tag{2.13}$$

Here, d describes the tip-sample distance, m the mass of the free electron and $\Phi = \frac{1}{2}(\Phi_s + \Phi_t)$ the average work function of sample and tip. The current is then described as

$$I(V) = \frac{4\pi e}{\hbar}\int_0^{eV} \rho_s(\epsilon)\rho_t(\epsilon - eV)T(\epsilon, V, d)d\epsilon \tag{2.14}$$

in the zero temperature limit. ρ_s and ρ_t denotes the local density of states at the tip and the sample, respectively.

Considering a finite temperature, the fermi distribution of both leads has to be included resulting in a current of tunneling electrons [33, 36] in the form of

$$I(V) = \frac{4\pi e}{\hbar}\int_{-\infty}^{\infty} [f(\epsilon - eV) - f(\epsilon)]\rho_s(\epsilon)\rho_t(\epsilon - eV)T(\epsilon, V, d)d\epsilon \tag{2.15}$$

with $f(E) = [1 + exp(\beta(E - E_F))]^{-1}$ and $\beta = (k_B T)^{-1}$. Here, T is the temperature of the system and k_B the Boltzmann constant.

Tersoff Hamann Approximation

The formalism Bardeen derived was considering two flat metallic electrodes seperated by an insulating layer, which does not represent the real geometry of the tunneling junction. To describe the STM junction, Tersoff and Hamann [33, 37, 38] calculated the Bardeen matrix element using wave functions for the tip and the surface. The tip wave function is approximated by an s-wave. Here, the current through the junction is only depending on the local density of states (LDOS) of the surface at energy E_F measured at the center of the tip apex r_t.

$$I(V) \propto \rho_{sample}(E_f, r_t) \tag{2.16}$$

For the interpretation of STM images the Tersoff Hamann approximation is widely used for ab initio calculations of STM images. However, the premise of an s-shaped tip is not always valid as adsorbates on the tip can change the

structure of the tip wave function, which reveal different structures in STM topography [39].

Operating modes

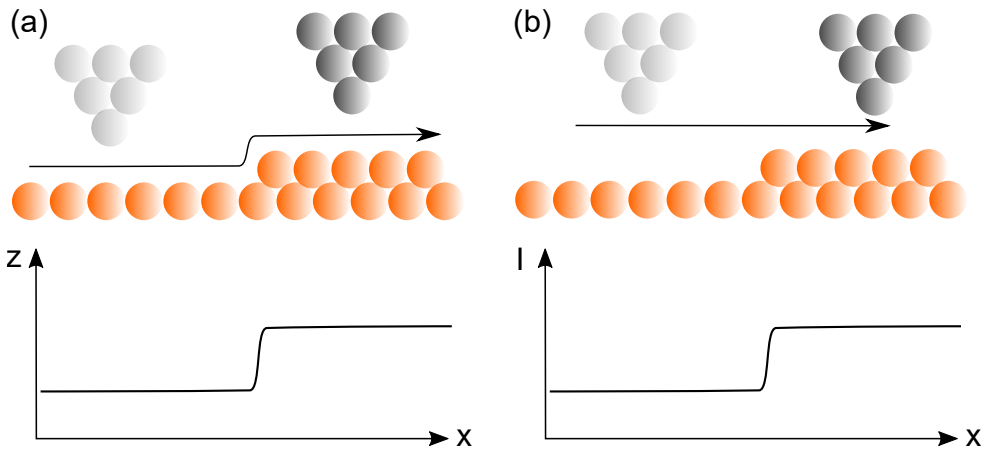

Figure 2.3: The two different operating modes of the STM are schematically shown. In (a) the constant current mode is represented and in (b) the constant height mode. The bias voltage and the (a) current or (b) tip-sample distance is set prior to image acquisition. In constant current mode the tip movement z is recorded, while in constant height mode the current I is recorded. Both representing the topographic information of the substrate.

The scanning tunneling microscope can be operated in two different modes, i.e., the constant current or constant height mode. In constant height mode the tip-sample distance z is set to a constant value and the current, representing the constitution of the surface, is recorded. In contrary, in constant current mode the current is kept constant by an external feedback loop adjusting the height of the tip. The change in tip-sample distance z can now be recorded over the scan area. A schematic drawing of the two modes is shown in Figure 2.3. The tip is mounted on a cylindrical piezoelectric actuator, which can move the metal tip in x, y and z direction over the sample substrate. Additionally, the sample is fixed on a slider mounted on piezoelectrics allowing a coarse movement of the sample with respect to the tip position. Typical scan areas using only the motion of the tip piezos are of the size of $\approx 400\,\mathrm{nm} \times 400\,\mathrm{nm}$ at temperatures of $5\,\mathrm{K}$.

2.2 Scanning Tunneling Spectroscopy

In addition to the recording of topographic information with atomic resolution, the scanning tunneling microscope can also be utilized for spectroscopic measurements of the local density of states of surfaces.

Considering small changes in bias voltages $dV = d\epsilon/e$, the change in current can be approximated by the integrand of equation 2.14. Further, the density of states of the tip and the transmission factor are assumed to be constant, leading to:

$$\frac{dI}{dV} = \frac{4\pi e^2}{\hbar}\rho_t(0)\rho_s(eV)T(eV, V, d) \propto \rho_s(eV) \tag{2.17}$$

As a consequence the acquisition of the differential conductance $\mathrm{d}I/\mathrm{d}V$ gives direct information of the local density of states of the substrate investigated in the scanning tunneling experiments [33]. The feedback loop is disabled during the recording of $\mathrm{d}I/\mathrm{d}V$ spectra resulting in a constant tip-sample distance z.

A common technique to measure the differential conductance is the use of a lock-in amplifier. One of the main advantage of a lock-in amplifier is the ability to recover signals with a low signal to noise ratio [33]. A small voltage modulation $V_m cos(\omega_m t)$ is sinusoidally applied with a modulation frequency ω_m to the bias voltage V.

A Taylor expansion of the tunnel current results in

$$I(V_0 + V_m\, cos(\omega t)) = I(V_0) + \left.\frac{\mathrm{d}I}{\mathrm{d}V}\right|_{V_0} V_\mathrm{m} cos(\omega t) + \left.\frac{\mathrm{d}^2 I}{\mathrm{d}V^2}\right|_{V_0} \frac{V_\mathrm{m}^2}{2} cos^2(\omega t) + \mathcal{O}(3) \tag{2.18}$$

The second term – the first harmonic – is proportional to the $\mathrm{d}I/\mathrm{d}V$ signal and therefore, following equation 2.17, proportional to the local density of states of the substrate, which now can be extracted from the amplitude of the signal of the first harmonic. For other applications the second derivative of the current can be extracted from the second harmonic which can be used to extract properties of the substrate like phonon excitations.

Additionally, maps of $\mathrm{d}I/\mathrm{d}V$ can be recorded by scanning over certain parts of the surface recording the $\mathrm{d}I/\mathrm{d}V$ signal at every point of the surface, combining

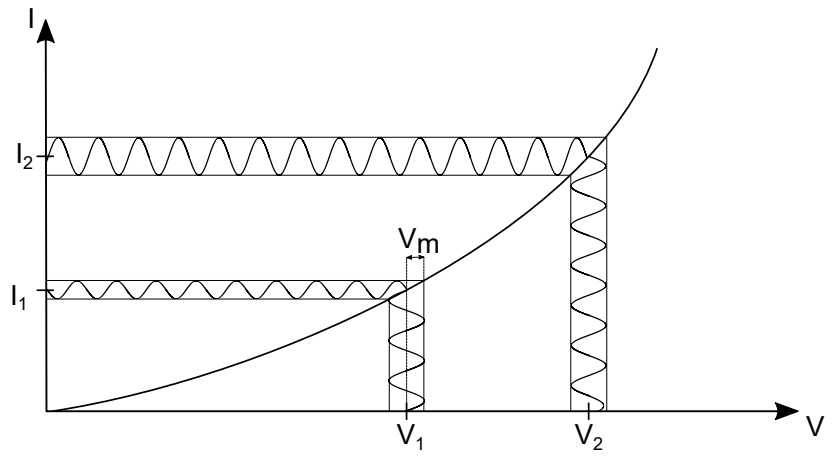

Figure 2.4: Model I(V) curve representing the current response to the small modulation V_m applied to the DC bias voltage V. Areas with a high slope result in a high amplitude of the current response.

the topographic data acquisition with spectroscopy. This allows to map the local density of states at a certain energy eV. Here, the tip can also be controlled in constant current or constant height mode. This technique can be used, *e.g.*, to measure the spatial distribution of molecular orbitals.

Inelastic Tunneling

While elastic tunneling electrons exhibit a constant energy tunneling through the junction depending on the applied bias voltage, it is also possible that the electron energy gets altered for example by excitation of phonons, molecular vibrations and spin flips during the tunneling process. These inelastic processes reduce (increase) the energy of the tunneling electron in the process of exciting (absorbing) , *e.g.*, a phonon. As soon as the energy of the tunneling electron exceeds the energy of a vibrational quanta $\hbar\omega$ a new tunneling channel is opened, which results in an increase of the recorded current. This increase of the conductance is visible as steps in the $\mathrm{d}I/\mathrm{d}V$ spectrum at the energy $\hbar\omega$ for positive and negative bias voltages. This process is schematically shown in Figure 2.5(a).

Inelastic electron tunneling spectroscopy (IETS) is often used for the investigation of phonons or off-resonant excitations of molecular vibrations. Molec-

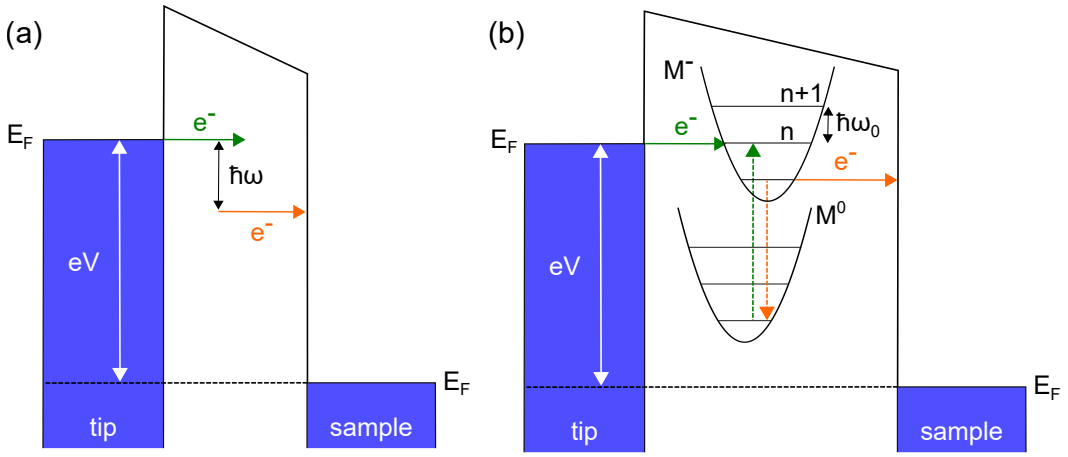

Figure 2.5: Representation of an electron tunneling through the vacuum junction considering inelastic processes at positive bias voltages. (a) The tunneling electron excites a vibration with the energy $\hbar\omega$ during the tunneling process and subsequently reaches the sample with reduced energy. (b) The tunneling electron excites a molecular vibration with the energy $\hbar\omega_0$ by transiently charging the molecule from its ground state M_0 to M^-. The charged molecule than relaxes into the ground state and the electron flows to the sample leaving the molecule in its unexcited and uncharged state M_0.

ular vibrations can also be observed as progression peaks, where the tunneling electrons resonantly couple to the electronic states of the molecule. Here, the tunneling electron transiently charges the molecule ($M^0 \rightarrow M^-$) and therefore is able to excite molecular vibrations with energy $n\hbar\omega_0$ (n denotes the order of the vibrational mode) directly in the molecular orbital. In this case the excitation of molecular vibrations is directly visible as peaks in the dI/dV spectrum. The peak intensity can be described in the Franck-Condon picture, as discussed in Chapter 2.8.

Broadening Mechanisms

Spectroscopic lineshapes are influenced by different broadening mechanisms. In STS the main broadening results of the temperature, the lock-in amplifier and the finite hybridization and therefore reduced lifetime of the electronic states. The temperature broadening is defined by $\chi_T(V) = \chi_T(0)cosh^{-2}\frac{eV}{2k_BT}$, which corresponds to a FWHM of $3.5k_BT$ [40]. However, the contribution to the ob-

served linewidth at 5 K is only 1.5 meV and therefore contributes only for a small percentage.

The instrumental broadening of the lock-in amplifier is given by the function

$$\chi_m = \begin{cases} \frac{2\sqrt{V_m^2 - V^2}}{\pi V_m^2} & \text{for } |V| \leq V_m \\ 0 & \text{for } |V| > V_m \end{cases} \tag{2.19}$$

where V_m is the modulation amplitude and ω the modulation frequency [40]. The FWHM of this function is $1.7V_m$. Typical values used as modulation amplitudes in the lock-in amplifier are $V_{m,rms} = 5\,\text{mV}$ and consequently $V_m = \sqrt{2}V_{m,rms} = 7.071\,\text{mV}$. The total instrumental broadening is then given by

$$\Delta E = \sqrt{(3.5k_BT)^2 + (1.7eV_m)^2} \tag{2.20}$$

The instrumental broadening, however, only has a comparably small contribution to the observed linewidth of, *e.g.*, molecular orbitals in scanning tunneling spectroscopy. As electrons are injected into the molecular orbitals they experience a distinct residence time τ in the molecule during the tunneling process. This residence time is mainly dependent on the extend of hybridization with the surface, which can be reduced by buffer layers on the metallic substrate. The lifetime limited resonances than result in Lorentzian line shapes for the orbital signatures with a width δ observed in $\mathrm{d}I/\mathrm{d}V$ spectra. The linewidth is inversely proportional to the residence time of the tunneling electron $\delta \sim \frac{1}{\tau}$.

2.3 Experimental Setup

The experiments were performed on a home-build STM, which consists of two separate vacuum chambers: the acquisition chamber (AC) and the preparation chamber (PC) with a base pressure of $1 \cdot 10^{-9}\,\text{Pa}$. The STM head is mounted in a liquid helium bath cryostat achieving temperatures of 5 K. The cryostat consists of two separated reservoirs. An inner one with a capacity of 4 l filled with liquid helium or nitrogen and the outer one with a capacity of 14 l filled with liquid nitrogen acting as a radiation shield for the environment. The standing time for one filling with liquid helium is $\approx 36\,\text{h}$ without sample transfers. Additionally, an

e-beam evaporator is mounted to the AC, allowing the deposition of molecules from a heated Mo-crucible directly on the cold sample ($\approx$ 10 K) through two connected holes in the radiation shields. The preparation of samples is done on the manipulator in the preparation chamber, where temperatures of up to 2500 K can be reached. Simultaneously, the sample can be exposed to the sputter gun or an molecular evaporator for additional preparation steps. The UHV chamber is pumped with turbomolecular and ion getter pumps. During the measurement, the vacuum is sustained only using the ion getter pumps to reduce the noise level by turning off the mechanical pumps. Further, it is possible to transfer samples or molecules into the chamber without breaking the vacuum using a separately pumped part of the preparation chamber, the load lock. It is convenient when working with different molecules, as they tend to be exchanged regularly. The whole chamber is mounted on an actively damped suspension. Additionally, the STM head is attached to a spring system, which significantly reduces the external noise during data acquisition. In the experiments tips cut from a Au wire (purity: 99.995 %, diameter: 0.25 mm) are used and are prepared *in-situ* by field emission and gentle contacts on the Au(100) surface prior to the experiments.

2.4 Sample Preparation

In order to achieve clean and monocrystalline metal surfaces, the samples used in the experiments were cleaned by repeated Ar^+ ion bombardments and subsequent annealing. Surfaces with a high amount of trapped bulk carbon have additionally been prepared with oxygen cycles to remove segregated carbon residues, which always is finished by a flash at higher substrate temperatures to make sure all created CO molecules are evaporated from the samples surface. In the following, the two dimensional materials graphene and hexagonal boron nitride are grown by chemical vapor deposition (CVD) and temperature programmed growth (TPG) using ethylene and ammonia borane. The growth procedure of two dimensional materials is explained in more detail in Chapter 3.1.

2.5 Calibration

The piezoelectric actuators, which move the tip above the sample, are contracted or expanded by an applied voltage. To convert this voltage into distances, a conversion factor and therefore a calibration on known surface structures has to be performed. In the present case the surface reconstruction of the Au(100) surface, as well as the atomic structure of graphene with its unique lattice constant has been used as a reference for calibration. Here, parallel lines of the Au(100) reconstruction have a distance of 144 pm and can be used to determine the piezo constants prior to the measurement (Figure 2.6).

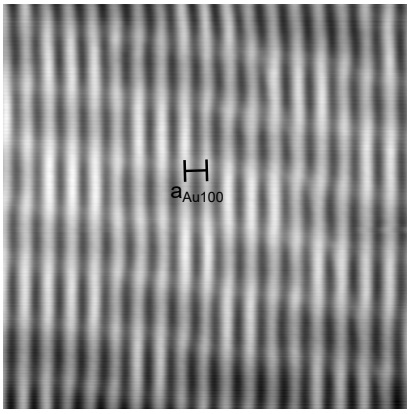

Figure 2.6: Surface reconstruction of Au(100) used to calibrate the scanning piezos before the experiment. The distance between adjacent rows is indicated.

2.6 The Moiré Effect

When two atomic layers with a small lattice mismatch are stacked on top of each other a so called moiré effect is observable, which is a spacial beat and the result of a different vertical stacking of the atoms in the two layers. In the presented experiments, graphene and hexagonal boron nitride (both with hexagonal symmetry) were grown on Pt(111) and Ru(0001), which in the used surface orientation also exhibit a hexagonal symmetry. This stacking of two hexagonal systems will result in a hexagonal moiré superstructure as shown in the model in Figure 2.7 (a). The system can be described in the reciprocal

space with their distinct wave vectors $\overrightarrow{k_s}$ and $\overrightarrow{k_{2D}}$, denoting the wave vectors of the substrate and the two-dimensional material, respectively [41, 42]. The wave vector of the moiré $\overrightarrow{k_m}$ follows as

$$\overrightarrow{k_m} = \overrightarrow{k_{2D}} - \overrightarrow{k_s} \tag{2.21}$$

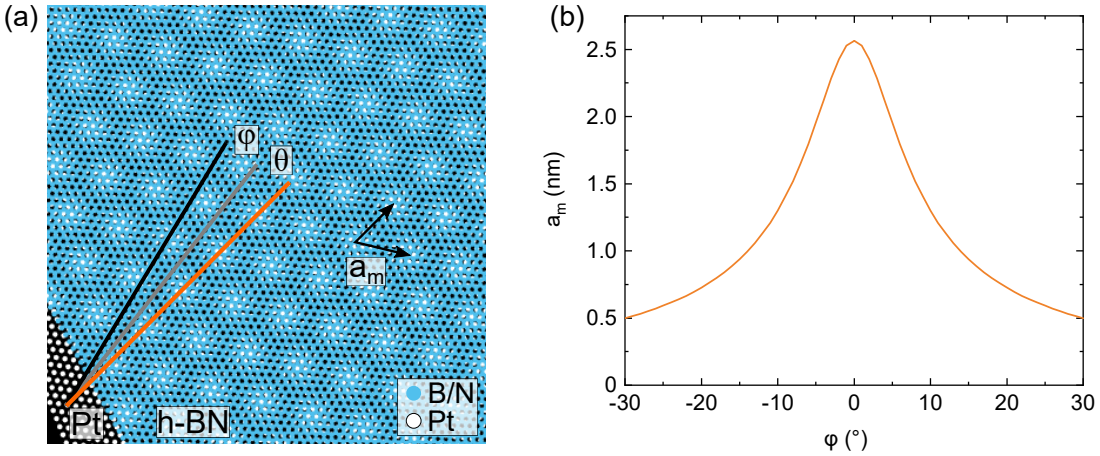

Figure 2.7: (a) Moiré effect as a result of the lattice mismatch and twist angle (φ) between h-BN (light blue) and the Pt(111) (white) surface. (b) Calculated moiré periodicity a_m for different twist angles φ between h-BN and the Pt(111) surface following equation 2.22 with $a_{2D} = a_{h-BN} = 2.5\,\text{Å}$ and $a_s = a_{Pt} = 2.77\,\text{Å}$.

The size of the moiré periodicity a_m in real space is an important property for comparison with the STM experiments. It can therefore be calculated using the following equation

$$a_m = \left(\sqrt{\frac{1}{a_{2D}^2} + \frac{1}{a_s^2} - \frac{2 \cdot cos\varphi}{a_{2D} \cdot a_s}} \right)^{-1} \tag{2.22}$$

where a_{2D} and a_s denotes the lattice constants of the two dimensional material, the substrate and φ the rotation angle between the two lattices. The relative rotation angle θ of the moiré pattern with respect to the substrate lattice is then given by

$$sin(\theta) = \frac{a_m}{a_{2D}} sin(\varphi) \tag{2.23}$$

2.7 Molecular Adsorption on Surfaces

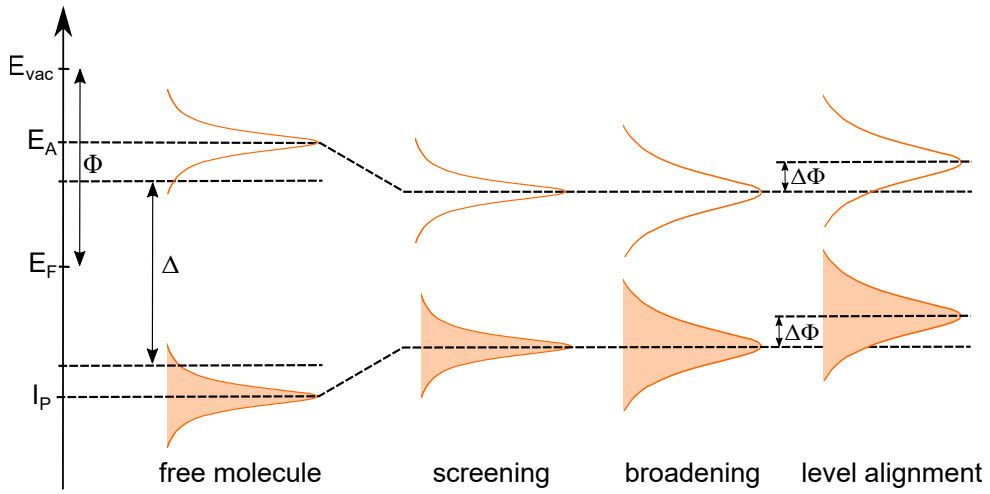

Figure 2.8: Energy level alignment upon adsorption on a metal surface. The HOMO-LUMO gap of the free molecule Δ is increased by the Coulomb energy U and decreased due to screening of the transient charged molecule in the metal surface. The effect of the lifetime broadening on the molecular states and the energy level alignment is also shown. The figure is adapted from [43, 44].

The investigation of molecules with the exchange of electrons results in the change of the on-site energy of the molecule, which modifies its energy levels compared to the simple 'one-particle' picture of the free molecule. This additional energy U, which increases the HOMO-LUMO gap Δ of the free molecule, has to be considered in the evaluation of its energetic levels [43]. In the free case, the energy of the highest occupied molecular orbital (HOMO) observed in scanning tunneling spectroscopy is defined by the ionization potential I_p, i.e., the energy an electron needs to exceed in order to leave the molecule. The energy of the lowest unoccupied molecular orbital (LUMO) is described by the electron affinity E_A, i.e., the energy to add one electron to the molecule.

The transient charged molecule is now in close contact with the metallic substrate. A screening of the charged molecule due to a redistribution of electrons in the surface region can effectively reduce the Coulomb repulsion and therefore the observed HOMO-LUMO gap, as shown in Figure 2.8. Additionally, the observed peaks are broadened due to a reduced lifetime of the electronic states, as the tunneling rate into the metal is very high. This results in a broadening

of the observed peaks of several hundred meV considering a tunnel lifetime of a few femtoseconds [44, 45].

The energetic position of the observed orbitals can be influenced by the electronic structure of the surface. Charge transfer or local work function variations ($\Delta\Phi$) are able to shift the molecular orbitals varying the observed HOMO-LUMO gap. In the case of a charge transfer to (from) the molecule, a shift of only one orbital energy can be observed. Local work function changes on the other hand result in a rigid shift ($\Delta\Phi$) of both molecular orbitals as HOMO and LUMO are shifted to the same extend due to their vacuum level alignment if the coupling to the metallic substrate is reduced, for example by the use of efficient buffer layers like graphene or h-BN [46].

2.8 Franck-Condon Principle

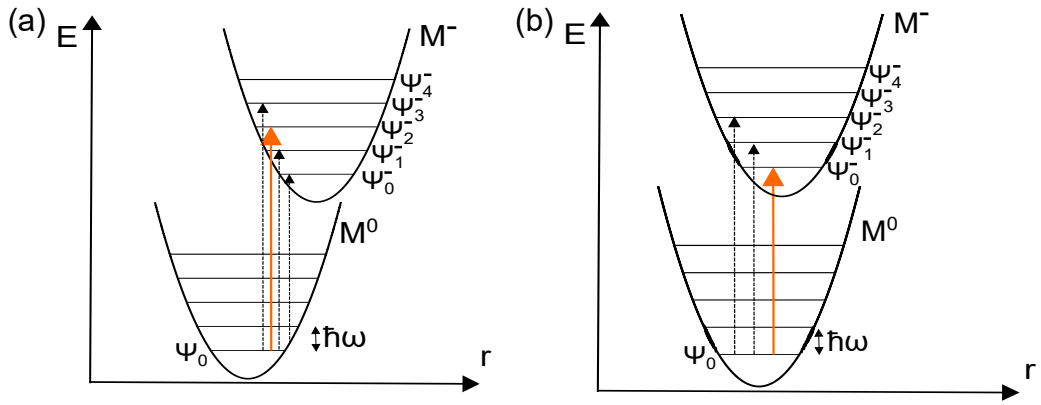

Figure 2.9: Schematic transitions according to the Franck-Condon principle. Transitions between Ψ_0 and Ψ_n^- are indicated. The most likely transition is indicated with a bold orange arrow. The lateral displacement of both parabolic potentials depends on the strength of the electron-phonon coupling S_ν ((a)$S_\nu \geq 1$, (b)$S_\nu \leq 1$).

Reducing the hybridization between molecules and the metallic substrate by introducing a buffer layer often leads to the observation of vibrational resonances in the molecular orbitals investigated with STS. Those resonances are best described in the Franck-Condon picture [47–49]. The probability amplitude P of the ground state Ψ_0 of the molecule and its excited state Ψ_n^- is described by

$$P = \left\langle \Psi_n^- | \mu | \Psi_0 \right\rangle \tag{2.24}$$

The transition dipole moment consists of nuclei μ_n and electron μ_e interactions, respectively. In the Born Oppenheimer approximation the total wave function can be separated into contributions of the electrons Ψ_e and the vibrations Ψ_ν. The spin of the the particles is not considered.

$$\begin{aligned} P &= \left\langle \Psi_n^- | \mu | \Psi_0 \right\rangle = \left\langle \Psi_{n,e}^- \Psi_{n,\nu}^- | \mu_e + \mu_n | \Psi_{0,e} \Psi_{0,\nu} \right\rangle & (2.25) \\ &= \left\langle \Psi_{n,e}^- | \mu_e | \Psi_{0,e} \right\rangle \left\langle \Psi_{n,\nu}^- | \Psi_{0,\nu} \right\rangle + \left\langle \Psi_{n,e}^- | \Psi_{0,e} \right\rangle \left\langle \Psi_{n,\nu}^- | \mu_n | \Psi_{0,\nu} \right\rangle & (2.26) \end{aligned}$$

The electron wave functions are orthogonal. Therefore, equation 2.26 can be written as

$$P = \left\langle \Psi_{n,e}^- | \mu_e | \Psi_{0,e} \right\rangle \left\langle \Psi_{n,\nu}^- | \Psi_{0,\nu} \right\rangle \tag{2.27}$$

Here, the second integral $\left\langle \Psi_{n,\nu}^- | \Psi_{0,\nu} \right\rangle$ describes the overlap of the vibrational wave functions and is the Franck-Condon factor. The intensity of vibronic transitions can be described by a Poisson distribution [50–52]:

$$| \left\langle \Psi_n^- | \Psi_0 \right\rangle |^2 = \exp(-S_\nu) \frac{S_\nu^n}{n!} \tag{2.28}$$

S_ν is the Huang-Rhys factor for the respective vibrational mode ν and is a measure for the strength of the electron-phonon coupling.

CHAPTER 3

Two-Dimensional Materials

Partly reproduced from J. Vac. Sci. Technol. A 37, 061404, 2019, with permission from AIP Publishing.

3.1 Preparation and Properties of Graphene and h-BN

Creating monoatomically thin and uniform layers of two-dimensional materials, such as graphene and hexagonal boron nitride (h-BN), is a challenging task. Several *ex situ* methods like the exfoliation of bulk graphite [19] and h-BN [53] or epitaxial growth of bulk graphite [54] have been used. In UHV applications, the chemically assisted growth via chemical vapor deposition (CVD) is most commonly present [55]. Here, the vacuum chamber is backfilled with a gaseous precursor and the pristine crystal is annealed to temperatures favoring the thermal catalysis and the growth of the respective two-dimensional material. The growth mechanism is schematically shown in Figure 3.1. The precursor is exposed to the heated crystal at temperatures of $1000 - 1200\,\mathrm{K}$ and in the following hydrogen is separated from the substrate, while boron, nitrogen or carbon remain on the crystal to form hexagonal boron nitride or graphene. Here, large layers are achievable depending on the amount of precursor molecules used, while the growth is self-limited to one monolayer as the availability of the metal catalyst

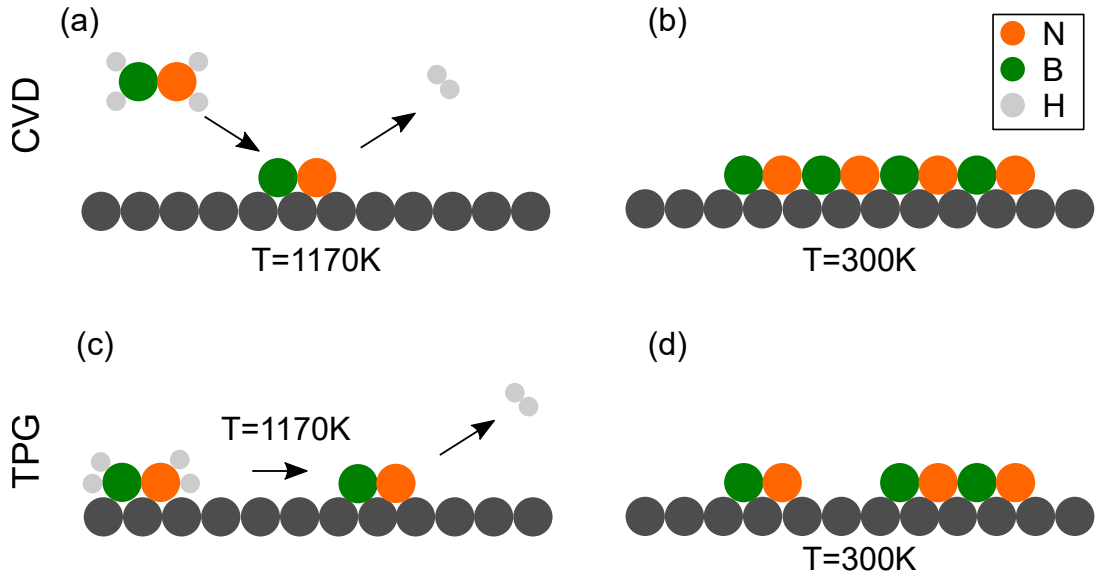

Figure 3.1: Schematic representation of the growth of h-BN on metal surfaces. The growth of graphene is analogous with ethene as the precursor molecule. (a) The precursor molecule aminoborane is evaporated on the hot surface in the approach via chemical vapor deposition (CVD). In the case of h-BN growth only boron (green) and nitride (orange) remain on the surface (dark grey), while hydrogen is transferred to the gas phase. (b) Formation of a single layer of h-BN on the metal surface. (c) During the temperature programmed growth (TPG) aminoborane is first adsorbed on the surface before the sample is annealed subsequently and the precursor molecule decomposes. (d) Formation of h-BN flakes on the metal surface.

surface is the limiting growth parameter [56, 57].

Another similar growth method is temperature programmend growth (TPG), where the precursor in a first step is adsorbed on the surface held at room temperatue and the crystal is annealed in the following. Here, the limiting factor of the layer size is the amount of adsorbed molecules, which can form flakes of two-dimensional materials [56].

While both methods are successfully used for the growth of two dimensional materials, the technical difficulty is the exposure of the gaseous precursor to the surface. For graphene growth it is rather straight forward as ethene, which is a gas at room temperature and thus can directly be induced into the vacuum chamber, can be used as a carbon source. Ethene will decompose on the surface at sufficient temperatures, releasing its hydrogen into the gas phase and the

remaining carbon atoms will start to form graphene at surface temperatures of around 1000 K [58]. The growth of hexagonal boron nitride is commonly done using borazine [59–62]. When using borazine as a precursor some technical challenges have to be solved. Borazine has a melting point of −58 °C and is very unstable in air at room temperature. To this end it has to be stored in the freezer and also cooled when installed at the vacuum chamber [57].

To counter those difficulties, ammonia borane (borazane) was used in the h-BN growth process. Borazane is a solid at room temperature, has a melting point of 104 °C and is most commonly used in low pressure CVD processes [57]. The elevated melting point makes storage at room temperature easier. Borazane is known to trap a lot of hydrogen and water, as it is commonly used in hydrogen storage devices [63–65]. Therefore, the borazane powder was stored in an desiccator to limit the trapping of hydrogen. Nevertheless it is important to degas the molecular powder thoroughly in the load-lock before transferring it to the preparation chamber in order to keep the chamber free of hydrogen contamination. In all cases borazane had to be kept in the load lock for two days until a reasonable pressure of 10^{-6} Pa was achieved.

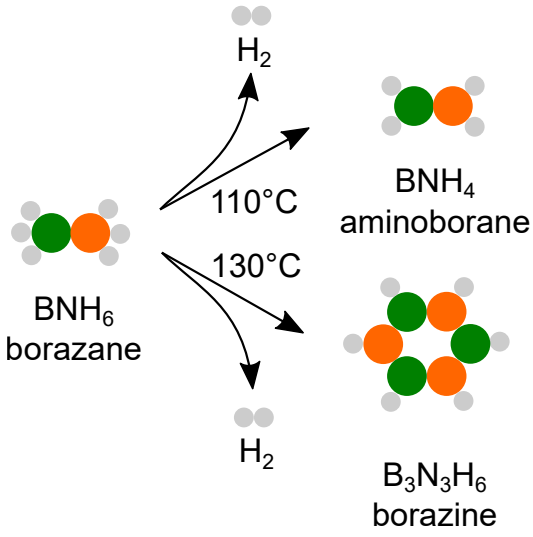

Figure 3.2: Decomposition of borazane (BNH_6) during the evaporation from a heated Ta crucible as described in Ref. [66, 67]. Borazane decomposes to aminoborane and borazine upon loosing hydrogen at the indicated temperatures.

During the annealing, borazane sublimes and decomposes into molecular aminoborane slightly above its melting point at 110 °C. At 130 °C borazine is also formed via intermediate polymeric polyaminoborane, while losing hydrogen [66, 67]. In the solid phase polyaminoborane and polyiminoborane – polymeric derivates of ammonia borane – are formed, which in principle at higher temperatures also could form hexagonal boron nitride. The decomposition into the polymeric phase did not limit the ability to grow h-BN on the substrate using the same powder of precursor molecules for more than five growth cycles. In the preparation procedure borazane was heated in a Ta crucible at temperatures of $\approx 110\,°C$ using a resistive button heater to mainly evaporate aminoborane from the crucible as the precursor for the following h-BN growth procedure. Both described growth methods, TPG and CVD, are possible using the direct evaporation of ammonia borane. After waiting for stable evaporation conditions for $\approx 30\,\text{min}$, the surface is exposed to a steady flow of aminoborane molecules evaporated from the Ta crucible. The exact evaporation rate of molecules onto the sample could not be determined during the experiment. The evaporation time has to be chosen in a way that a sufficiently large amount of molecules is adsorbed to promote the growth of large h-BN flakes with a diameter of up to 100 nm. The sample was held at room temperature and exposed to the sublimated aminoborane molecules for $2 - 3$ min and annealed in the following at temperatures of 1170 K for 5 min to promote the growth of h-BN. A longer evaporation time and therefore an increased adsorption of precursor molecules did not increase the size of h-BN flakes significantly, due to the equilibrium of molecules evaporated from the sample and the ones thermally decomposed in the growth process. Only the evaporation on the preheated substrate (CVD) led to closed monolayers of h-BN on the sample, as a steady flow of precursor molecules contributes to a prolonged fabrication of h-BN until the limit of one closed monolayer is achieved. During several test cycles, the TPG growth method yielded a more uniform and defect free h-BN structure with a distinct moiré pattern, whereas the CVD growth resulted in closed monolayers, with a worse uniformity and most probably residual adsorbates remaining on the Pt surface, which makes the availability of a well ordered moiré structure scarce.

3.2 Structure on Pt(111) and Ru(0001)

The two metal surfaces Ru(0001) and Pt(111) are used in the experiments, as they are the most strongly and most weakly interacting surfaces regarding the graphene and h-BN sheets, respectively, resulting in different extends of corrugation [68, 69]. A comparison of graphene and hexagonal boron nitride on both surfaces will be discussed in the following.

3.2.1 Pt(111)

Figure 3.3(a) shows the h-BN-covered Pt(111) surface prepared using the aforementioned TPG growth method. Using this technique, flakes of h-BN are formed on the metal substrate. The moiré pattern is visible as a periodic modulation of the h-BN layer. This periodic modulation results from the lattice mismatch between h-BN and Pt(111), where 10 BN atoms cover only 9 Pt surface atoms [69, 70]. The coincidence lattice directly determines the different sites of B and N atoms within the supercell on the Pt(111) surface, which lead to a corrugation of the h-BN layer as a consequence of attractive and repulsive h-BN–Pt interactions in the different stacking regions. Compared to the strong corrugation of h-BN on Ru(0001) [71, 72] and Rh(111) [73], which is generally refered to as the nanomesh [61], the corrugation for h-BN on Pt(111) is very low.

The different stacking regions on the nanomesh are named wire and pore sites and, consequently, in the following the periodic modulation on Pt(111) will also be named as wire and pore. Wire regions are characterized by B atoms residing at on-top Pt sites and N atoms at hexagonal close-packed (hcp) stacking sites of the Pt(111) lattice, furthermore, symmetrically unequal wire regions are composed of B atoms at hcp and N atoms at face-centered cubic (fcc) Pt(111) sites. Regions of the nanomesh with B atoms adsorbed at fcc and N atoms at on-top Pt sites are entitled as wires. Wire and pore regions are characterized by their increased and reduced h-BN–metal distance, respectively, as unraveled by DFT calculations [70]. It was also shown for h-BN on Pt(111) that only 34 % of the N atoms encounter a distance to the surface below the average distance, resulting in rather small pore regions [70]. To facilitate a comparison of experimental with calculated data, the average apparent height within the moiré lattice unit cell

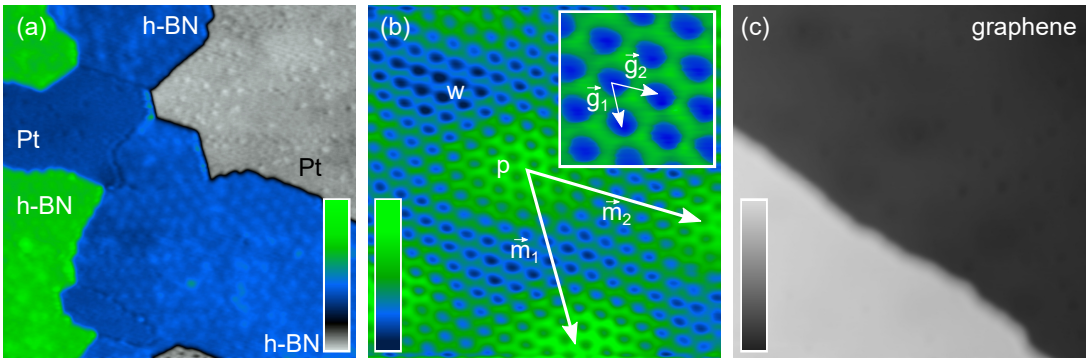

Figure 3.3: (a) STM image of h-BN-covered Pt(111) (1.7 V, 100 pA, 54 nm × 54 nm). The color scale ranges from 0 pm (light gray) to 637 pm (green). (b) Atomically resolved STM image of h-BN on Pt(111) (10 mV, 600 nA, 5 nm × 5 nm). The color scale ranges from 0 pm (dark blue) to 86 pm (green). Lattice vectors $\vec{m}_1$, $\vec{m}_2$ span the unit cell of the moiré superlattice. Wire (w) and pore (p) regions of the moiré pattern are indicated. Inset: Close-up view of the h-BN layer with $\vec{g}_1$, $\vec{g}_2$ spanning the honeycomb lattice. The color scale ranges from 0 pm (blue) to 26 pm (green). (c) STM image of graphene-covered Pt(111) (2 V, 100 pA, 40 nm × 40 nm). The color scale ranges from 0 pm (black) to 295 pm (gray).

was determined, revealing that the area with a larger apparent height than the average value is ≈ 30 % of the unit cell area. Consequently, areas within the unitcell with elevated apparent height are assigned to the pore regions, whereas the neighboring regions with a lower apparent height are designated to the wire sites. Therefore, the geometrically lower (higher) regions of the h-BN moiré are assigned as pore (wire) and appear higher (lower) in STM images. Similar findings were previously reported for h-BN on Rh(111), using non-contact atomic force microscopy [74].

Below a specific separation between the tip and the surface, tip-induced elastic deformations of the h-BN sheet have been investigated, where pores appear higher than wires reaching a certain threshold tip-sample distance. A similar mechanism cannot be excluded for the STM images of h-BN on Pt(111), albeit the same contrast for pores and wires was present in STM images acquired with different orders of tunneling currents in the range from 100 pA to 600 nA and therefore different tip-sample distances. As a consequence, the tip-induced elastic deformations of h-BN would have to already appear at ele-

vated tip-sample distances. However, the effect may tentatively be accredited to the electronic structure of h-BN on Pt(111). A comparable inversion was reported for graphene on Ir(111), where geometric hill regions of the moiré appeared lower than the surrounding valley sites [41]. Later this effect was explained by the electronic structure of graphene on Ir(111) [75]. Graphene on Ir(111) exhibits a contrast inversion in constant-current STM images at a certain bias voltage. For h-BN on Pt(111) no inversion in the shape of the moiré structure was found in the bias voltage range $|V| \leq 2.5\,\mathrm{V}$. The moiré lattice is spanned by the lattice vectors $\vec{m}_1$ and $\vec{m}_2$ as shown in Figure 3.3(b) with $m_1 = |\vec{m}_1| = 2.6 \pm 0.1\,\mathrm{nm} = |\vec{m}_2| = m_2$. This moiré period can be assigned to a rotation angle of 0° of the h-BN lattice relative to Pt(111). The inset to Fig. 3.3(b) unravels the atomic h-BN lattice with the honeycomb lattice vectors $\vec{g}_1$ and $\vec{g}_2$ where $g_1 = |\vec{g}_1| = 0.26 \pm 0.02\,\mathrm{nm} = |\vec{g}_2| = g_2$. Similar parameters have been previously reported for h-BN on Ir(111) [55]. The amplitude of the corrugation of the moiré superstructure is 40 pm for $V \geq 1.5\,\mathrm{V}$, which is a relatively small value and signals a weak h-BN–Pt(111) interaction [70, 76]. Indeed, h-BN on Pt(111) was reported to be physisorbed [77, 78], which was assigned to a reduced mixing of Pt s, d with h-BN π bands [69, 76].

However, the h-BN moiré pattern was not always as pronounced as shown in Figure 3.3(b). In some areas of the h-BN flakes the moiré pattern was interrupted (shown in the lower part of the STM image in Fig. 3.3(a)). This finding can be explained by the presence of defects, like atom sized protrusions or residual adsorbates, on the Pt(111) surface that locally delaminate h-BN from the surface, which reduces the already weak h-BN–Pt(111) hybridization even further, resulting in a lowering or complete vanishing of the moiré corrugation.

After investigating the structural properties of h-BN on Pt(111), the properties of graphene on the same substrate should be discussed. As can be noticed in the STM image 3.3(c), a nearly uniform grown monolayer of graphene spanning over several Pt(111) terraces was grown using a CVD growth method. A moiré modulation is scarcely visible on the graphene layer, hinting a very weak interaction between the graphene layer and the Pt(111) substrate. Due to weak interaction, a multitude of rotational domains with different faint moiré periodicities have been reported, which however are not present in this case after using the described CVD method [79]. Moreover, in the case of a visible moiré lattice,

its corrugation is significantly lower than on Ru(0001), which reflects the low graphene–Pt hybridization [80, 81]. Irregularly distributed depressions can most likely be atributed to Pt(111) lattice vacancies [82] or C impurities embedded in the Pt(111) surface [83].

3.2.2 Ru(0001)

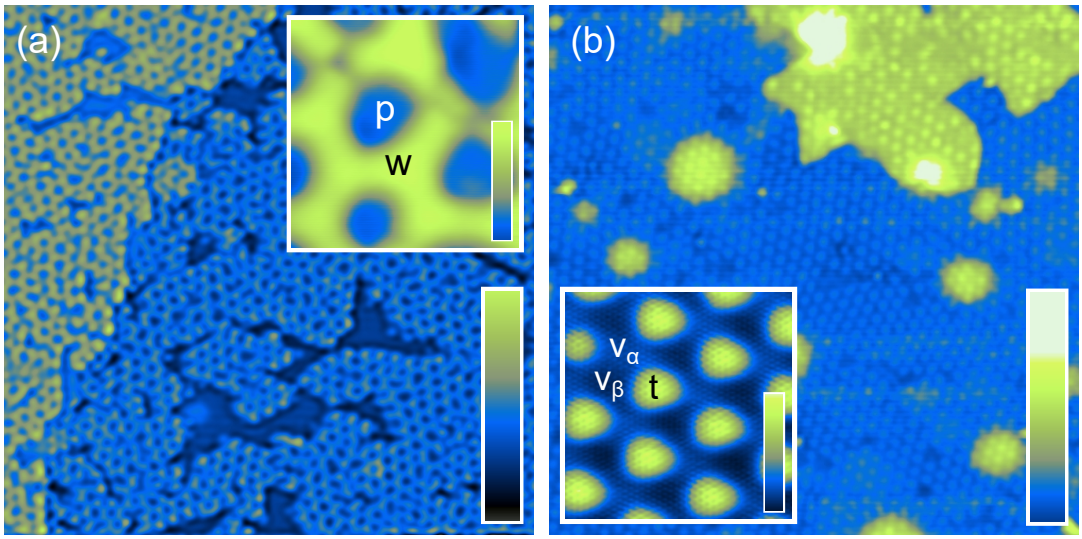

Figure 3.4: (a) STM image of h-BN-covered Ru(0001) (0.46 V, 100 pA, 120 nm × 120 nm). The color scale ranges from 0 pm (dark blue) to 704 pm (green). Inset: Close-up view of (a) showing the h-BN mesh in more detail (0.2 V, 100 pA, 7.2 nm × 7.2 nm). The color scale ranges from 0 pm (blue) to 147 pm (yellow). Wire and pore sites are marked as w and p. (b) STM image of graphene-covered Ru(0001) (1 V, 100 pA, 111 nm × 111 nm). The color scale ranges from 0 pm (dark blue) to 489 pm (white). Inset: Atomically resolved close-up view of (b) (1.27 V, 50 pA, 10 nm × 10 nm). The moiré superlattice is visible as protrusions (t) and depressions (v_α, v_β). The color scale ranges from 0 pm (dark blue) to 124 pm (light yellow).

In Figure 3.4(a) a representative STM image of h-BN on Ru(0001) following the TPG growth process is shown. In comparison to h-BN on Pt(111) (Figure 3.3(a)), a pronounced and strongly corrugated nanomesh moiré pattern is discernible with clearly visible wire (w) and pore (p) regions (inset to Figure 3.4(a)). This periodic modulation with a strong corrugation similar to the h-BN

nanomesh was first observed on Rh(111) [61]. The supercell formed for h-BN on Ru(0001) consists of 12×12 B/N atoms covering 13×13 Ru atoms [84]. Wires are formed when B/N atoms reside at top and hexagonal close-packed (hcp) or hcp and face-centered cubic (fcc) sites of the Ru surface, while the strongly bound pores are formed when arranging at fcc and top sites [84]. The STM experiments showed that the average corrugation amplitude of the moiré pattern depends on the bias voltage. For $0\,\mathrm{V} < V \leq 0.5\,\mathrm{V}$ a corrugation amplitude of $\approx 100\,\mathrm{pm}$ was measured, which decreased to $\approx 60\,\mathrm{pm}$ at $\approx 1\,\mathrm{V}$ and nearly vanishes for $V \geq 2\,\mathrm{V}$. At negative bias voltage ($V < 0\,\mathrm{V}$) the corrugation was most pronounced with a nearly constant value of $\approx 130\,\mathrm{pm}$. Because of the elevated corrugation, atomic resolution of the h-BN lattice was not achieved, even though using several tips with different microscopic structures and diverse sets of tunneling parameters.

The graphene moiré on Ru(0001) (Figure 3.4(b)) also exhibits an enhanced corrugation with three different regions labeling the protrusions t and the depressions v_α and v_β, resulting in different stacking regions of graphene regarding the Ru(0001) substrate. The supercell consists of 23×23 C atoms on 25×25 Ru atoms [84–86]. The period of protrusions of the moiré superstructure is $\approx 3\,\mathrm{nm}$, which is also reported in the literature [86–89]. Protrusions (t) are due to graphene-Ru stacking regions where C atoms occupy fcc and hcp hollow sites of Ru(0001). The depressions of the moiré pattern result from stackings where C atoms reside at and close to top and fcc (v_α, dark contrast) or top and hcp (v_β, darkest contrast) sites of the substrate lattice [88, 90]. The corrugation is found to be $110 \pm 6\,\mathrm{pm}$ which is comparable to a corrugation of 150 pm found using DFT calculations of graphene-covered Ru(0001) and results from a geometric buckeling of the graphene layer [85]. Compared to h-BN, no voltage dependency of the graphene moiré in the investigated voltage range was present. Due to the extended exposure to ethene during the growth process, also bilayer graphene areas are found on the surface, which emerge from the segregation of bulk carbon. The moiré structure is very similar to the one on the monolayer, hinting the origin of the moiré to the interaction of the bottom graphene layer with the Ru(0001) surface [91].

3.3 Conclusions

The two possible routes for the growth of the two-dimensional materials graphene and h-BN have been discussed. Depending on the growth method, flakes or closed monolayers are achieved on the metal substrates Pt(111) and Ru(0001). The different strength of interaction results in weakly and strongly corrugated surfaces on Pt(111) and Ru(0001), respectively.

CHAPTER 4

Growth of a Graphene/h-BN Heterostructure

Theoretical support was provided by Prof. Yuriy Dedkov and Prof. Elena Voloshina from Shanghai University (China), Physics Department.

Besides the growth of monoatomically thin two-dimensional monolayers, the field of stacked bilayers of graphene [90, 92–96] and heterostructures of graphene grown on hexagonal boron nitride emerges in recent studies [97–109].

As discussed before, the growth of graphene and h-BN is catalytically activated on the metal surface, making a direct CVD approach feasible [56, 57]. However, after the completion of the first monolayer, the catalytic properties of the metal are suppressed by the grown two-dimensional material, making the growth of heterostructures a challenging endeavour. The absence of a metallic catalyst can be overcome with higher precursor pressures in the range of 10^2 Pa and long growth times of up to severeal hours, as reported in previous works [110–115].

As those parameters are not feasible for the direct use in UHV applications, an efficient alternative route to grow heterostructures of graphene and h-BN will be explored in the following. Here, graphene was grown via a two-step *in-situ* CVD approach, which is similar to the previously reported growth for bilayer graphene on Pt(111) [116]. First, h-BN was directly grown on the Pt(111) surface and subsequently buried by several layers of evaporated Pt atoms. This process recovers the catalytic metal surface properties, which allows to grow an additional layer of graphene on top of the intermediate Pt layer via CVD. The following

intercalation of Pt below h-BN results in a stacked structure of graphene on h-BN.

4.1 Pt Intercalation below h-BN and Growth Protocol

Similar to the approach to grow bilayer graphene on Pt(111) by sequential chemical vapor deposition [116], graphene has been grown on top of hexagonal boron nitride by the intermediate evaporation of Pt. In a first step, h-BN was grown on the Pt(111) substrate using the procedure described in Chapter 3.1. Subsequently, Pt was deposited via a hot filament, where a W wire (thickness $d = 0.2\,\mathrm{mm}$) was resistively heated to anneal a thin Pt wire (thickness $d = 0.2\,\mathrm{mm}$, purity $\geq 99,99\,\%$), which is wrapped around the W wire (Figure 4.1) and consequently evaporates Pt. To ensure the evaporation of Pt, the current through the filament was increased until a flux of Pt atoms was detected on a quartz microbalance mounted inside the preparation chamber. Typical currents used are in the range of $5 - 5.3\,\mathrm{A}$, depending on the contact to the electrodes and the tightness of the wrapping of the Pt wire around the W wire.

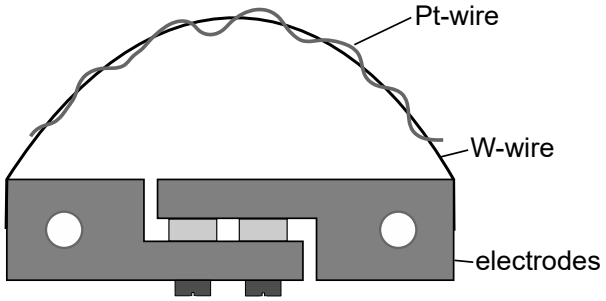

Figure 4.1: Sketch of the filament used for the evaporation of platinum. The W wire (black, thickness $d = 0.2\,\mathrm{mm}$) is spot-welded to the two metallic contacts, which are isolated by ceramics (light gray). A current is applied between both metallic contacts. The Pt wire (gray, thickness $d = 0.2\,\mathrm{mm}$, purity $\geq 99,99\,\%$) is wrapped around the W wire as a filament, which is heated by the W wire.

As the Pt melting point of $1760\,^{\circ}\mathrm{C}$ is relatively high [117] and the vapor pressure is comparably low, high temperatures had to be reached to ensure the

evaporation of a sufficient amount of Pt onto the sample, which was indeed possible by using the hot W filament.

As a preliminary test, Pt was evaporated onto the h-BN-covered surface, which was subsequently annealed to ensure the intercalation of Pt beneath the h-BN layer (Figure 4.2(b-d)). It was previously shown that metals like Ag [118], Au [97, 119–121], Co [122], K [123], Mn [124], Ge [125] and Ir [126] can be intercalated below a single h-BN sheet, which makes the intercalation of Pt very likely, too.

Figure 4.2(a) shows the Pt(111) surface covered with a single layer of h-BN. In the schematically shown representation of the reported growth protocol the h-BN layer is drawn in orange. The subsequently evaporated Pt covers the surface in clusters of different sizes (Figure 4.2(b)). For this test Pt has been evaporated for 15 min. Exemplary bigger clusters with diameters of up to 20 nm are marked with dashed yellow circles in the STM image, while the whole surface is also covered with smaller clusters, which arrange in a random pattern. The total thickness of those three dimensional clusters can only be estimated as the clusters cover the surface uniformly, only allowing the measurement of the relative corrugation. Clusters with heights of up to 3 nm are found, corresponding to a stacking of more than ten Pt atoms. After the evaporation of Pt, the sample was annealed at a temperature of 1170 K for 10 min resulting in the intercalation of most of the adsorbed Pt clusters below the h-BN flakes, which are now visible again at the top of the surface (Figure 4.2(c)). The atomically resolved h-BN lattice is shown in the inset to Figure 4.2(c). To ensure the full intercalation a second heating cycle at 1170 K was performed for 10 min, in which the h-BN flakes remain mostly invariant (Figure 4.2(d)). Comparing the nearly closed monolayer in Figure 4.2(a) with h-BN after the Pt intercalation (Figure 4.2(c,d)) it is to note that the monolayer of h-BN gets destroyed into smaller flakes during the intercalation. This process was also reported for the Pt intercalation on graphene, as defects and domain boundaries represent favored intercalation sites for the adsorbed Pt atoms, promoting a disruption of the monolayer [116, 127].

The successful intercalation of Pt below the h-BN layer now allows for a route to grow heterostructures of graphene and h-BN starting from h-BN flakes covered by the evaporated Pt (Figure 4.2(b)), which can be used as a platform to promote the CVD growth of graphene. Figure 4.2(e,f) illustrates the steps used

in the sequential growth of graphene on h-BN. After the growth of h-BN, several layers of Pt were evaporated from the hot filament onto the sample, as shown in Figure 4.2(b). Typical durations of Pt evaporation for the growth of graphene on h-BN have been $45-60$ min. As the Pt clusters are quite rough, an additional annealing period at 1170 K was performed for 3 min to flatten the intermediate Pt layers before performing the growth of graphene via CVD directly afterwards. The chamber was backfilled with ethylene at a pressure of $3 \cdot 10^{-5}$ Pa for 4 min. During this process the intercalation of Pt below h-BN already started. For the success of this growth it is important that a sufficiently large amount of layers of Pt $(30-50)$ are covering the surface, as the flattening process before the CVD growth otherwise will result in h-BN on the sample surface, impeding the catalytic growth of graphene on the intermediate Pt layer. As shown in Figure 4.2(e), parts of the surface are covered with graphene, while others already show a new moiré structure. To ensure a sufficient intercalation of Pt below h-BN, the sample is kept at an elevated temperature of 1170 K for an additional 10 min.

As shown in Figure 4.2(f), after completion of the described growth method a new structure with a distinct moiré period was found on large areas of the surface, which will be discussed in the following.

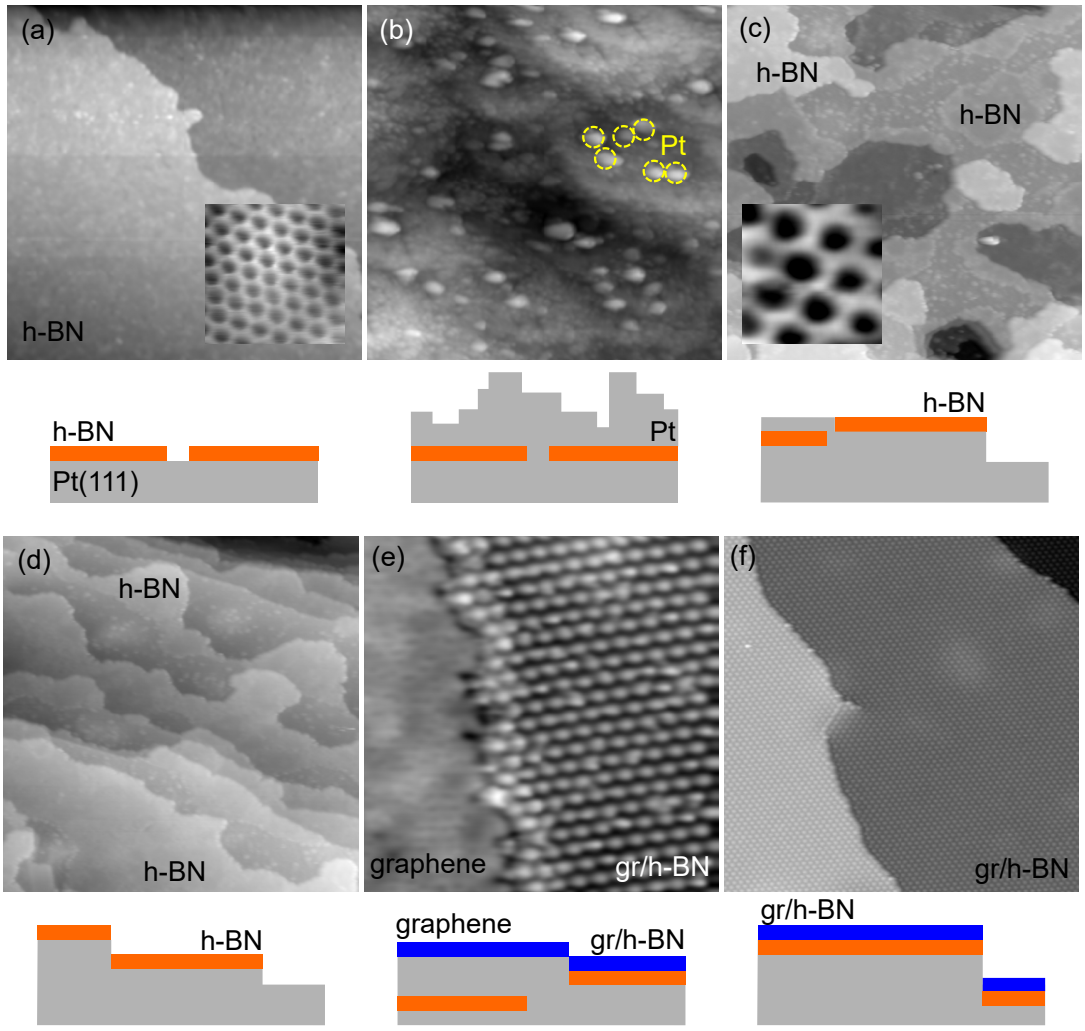

Figure 4.2: STM images and sketches of the growth protocol for the stacked growth of graphene on top of h-BN on a Pt(111) surface. (a) Monolayer of h-BN on Pt(111) (2.4 V, 100 pA, 100 nm × 100 nm). The inset shows the atomically resolved h-BN lattice (10 mV, 600 nA, 2 nm×2 nm). Sketch: h-BN flakes (orange) are grown on the Pt(111) surface (gray). (b) h-BN layer buried below Pt clusters (1.15 V, 100 pA, 100 nm × 100 nm). Sketch: h-BN buried below Pt evaporated from a hot filament. (c) h-BN flakes after intercalation of Pt. The sample was annealed at 1170 K for 10 min (2.1 V, 100 pA, 80 nm × 80 nm). The inset shows the atomically resolved h-BN lattice (10 mV, 100 nA, 1 nm×1 nm). Sketch: h-BN on the sample surface after partial intercalation of Pt. (d) h-BN flakes after an additional annealing cycle at 1170 K for 10 min (1.4 V, 100 pA, 80 nm × 80 nm). Sketch: h-BN on the sample surface after intercalation of Pt. (e) STM image of graphene and the graphene/h-BN heterostructure on Pt(111) (0.5 V, 100 pA, 30 nm × 30 nm). Sketch: Graphene (blue) grown on top of the slightly smoothed Pt layer. (f) STM image of the graphene/h-BN heterostructure on Pt(111) (1 V, 100 pA, 100 nm × 100 nm). Sketch: Stacking of graphene on top of h-BN after intercalation of Pt.

4.2 Analysis of the Moiré Pattern

The structure of the observed moiré pattern (M) will be analyzed in the following (Figure 4.3(a)). First, the average moiré periodicity is found to be $|\vec{m_1}| = |\vec{m_2}| = 1.65 \pm 0.04\,\mathrm{nm}$.

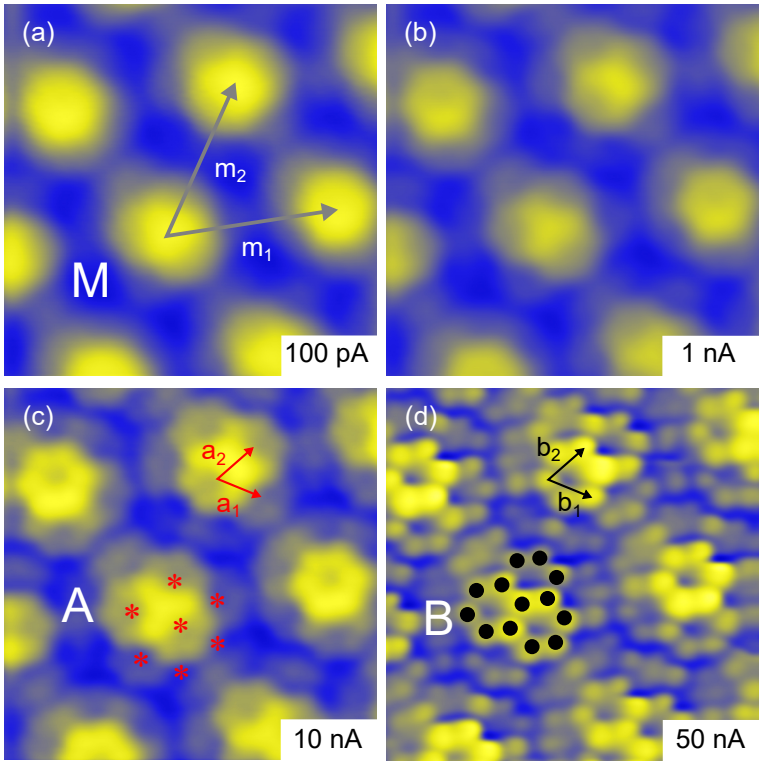

Figure 4.3: (a) STM images of the moiré of the graphene/h-BN heterostructure with different tunneling currents of (a) 100 pA, (b) 1 nA, (c) 10 nA, (d) 50 nA. The other tunneling parameters are 10 mV and 3.6 nm × 3.6 nm for all images. Depressions (protrusions) are marked with red asterisks (black dots) in (c,d). The lattice vectors of (a) the moiré $(\vec{m_1}, \vec{m_2})$, (c) structure A (red asterisks, $\vec{a_1}, \vec{a_2}$) and (d) structure B (black dots, $\vec{b_1}, \vec{b_2}$) are indicated.

Reducing the tip-sample distance by increasing the tunneling current usually results in an atomically resolved imaging of the surface structure revealing the hexagonal arrangement of, *e.g.*, graphene, as described in Chapter 3.1. However, for the investigated system a hexagonal structure marked with red asterisks in Figure 4.3(c) with a distinct periodicity of $|\vec{a_1}| = |\vec{a_2}| \approx 0.45\,\mathrm{nm}$ emerges. This hexagonal structure will be referred to as A in the following. Upon further reduc-

tion of the tip-sample distance, the edges of structure A change their shape and are now visible as a honeycomb of protrusions with the same lattice parameter as A of $|\vec{b_1}| = |\vec{b_2}| = |\vec{a_1}| = |\vec{a_2}| \approx 0.45\,\text{nm}$. This honeycomb will be named B and is marked with black dots in Figure 4.3 (d). Comparing the periodicity of B with the lattice constant of graphene of $|\vec{g_1}| = |\vec{g_2}| = 0.246\,\text{nm}$ (Figure 4.4), a factor of $\approx \sqrt{3}$ is discernible giving a hint that the dots emerge from the graphene lattice at the top of the heterostructure due to its hexagonal symmetry. Therefore, the honeycomb structure B is a direct result of the graphene honeycomb with a $(\sqrt{3} \times \sqrt{3})R30°$ regarding the graphene unitcell. The hexagonal arrangement of structure A does coincide in different ways with the maxima of the moiré, *e.g.*, either a depression of structure A or a protrusion of structure B are close to the maximum of the moiré pattern. However, no long range commensurable structure is discernible between the moiré pattern and structure A or B over the range of $\approx 10\,\text{nm}$.

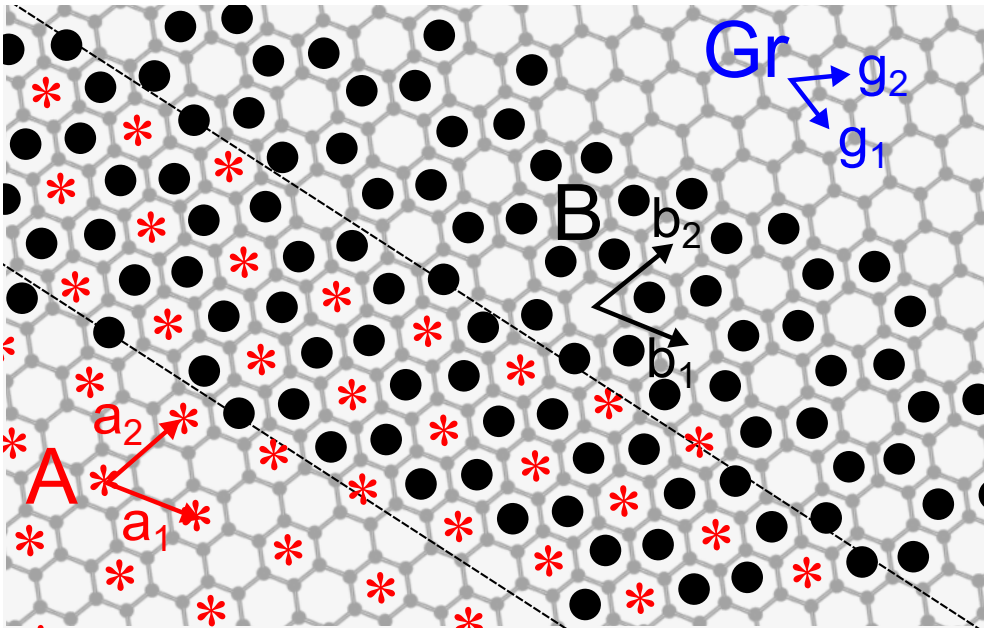

Figure 4.4: Sketch of the two superstructures A (red asterisks, $\vec{a_1}, \vec{a_2}$) and B (black dots, $\vec{b_1}, \vec{b_2}$) regarding the graphene lattice (black dots, $\vec{g_1}, \vec{g_2}$), which can be observed simultaneously at high tunneling currents.

Following the results derived above, superstructures A and B are schematically shown with respect to the graphene lattice in Figure 4.4. Here, the emergence from both the depressions (A, red asterisks) and protrusions (B, black

dots) can be directly linked geometrically to the graphene lattice on top of the heterostructure.

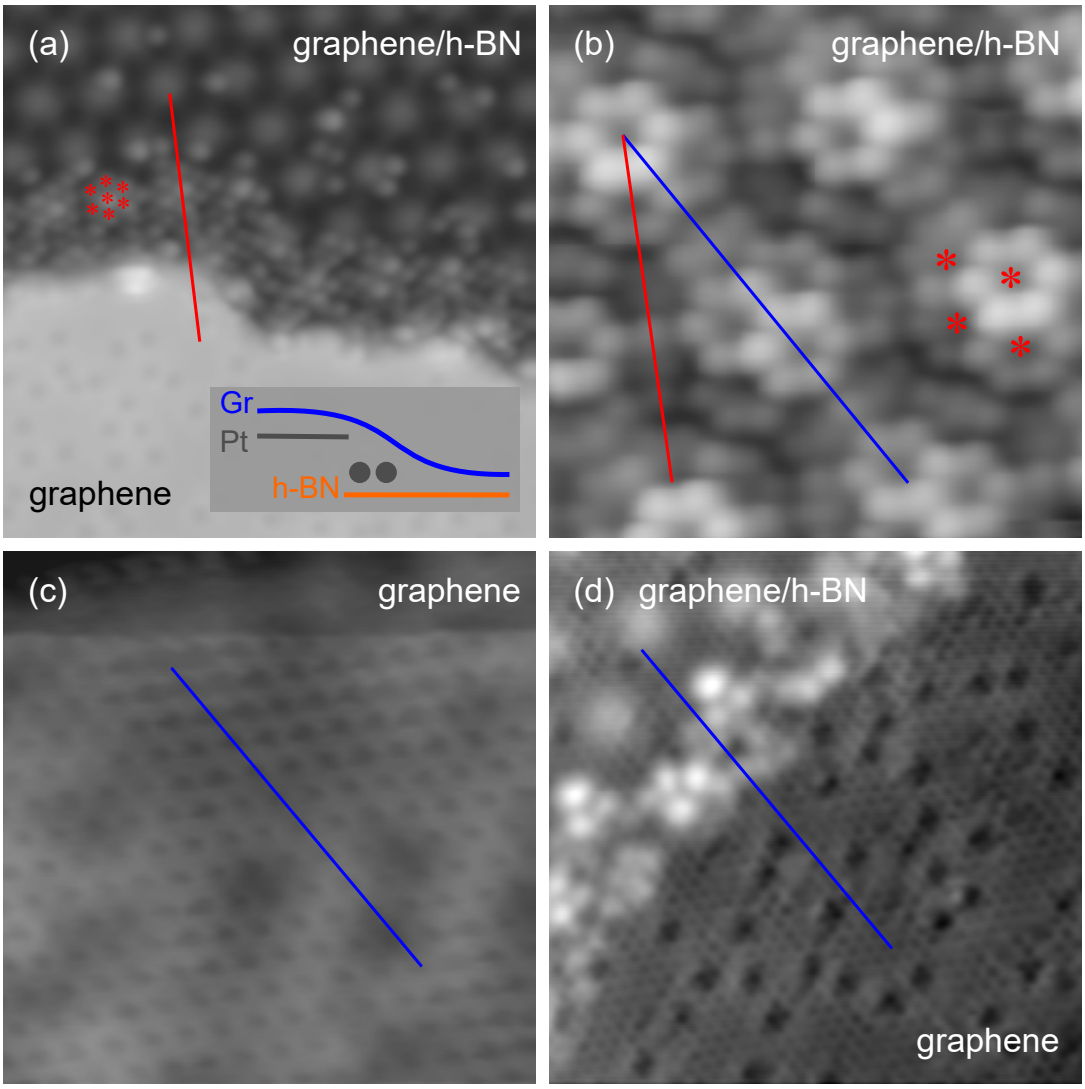

Figure 4.5: (a) STM image of the transition area of the graphene/h-BN heterostructure (top) to monolayer graphene (bottom) (100 mV, 100 pA, 13.5 nm × 13.5 nm). The direction of structure A is indicated with a red line. Red asterisks are superimposed on exemplary protrusions at the edge of the heterostructure. Inset: Sketch of the graphene and h-BN layer over the transition region, with possible residual Pt atoms marked as dots. (b) Close-up STM image of the graphene/h-BN heterostructure with structure A (10 mV, 50 nA, 3.6 nm × 3.6 nm). Lattice directions of graphene (blue) and A (red) are indicated. (c) Atomically resolved monolayer graphene recorded in the lower half of the transition region shown in (a) (10 mV, 10 nA, 3.6 nm × 3.6 nm). The graphene orientation is indicated with a blue line. (d) STM image of the transition region between graphene/h-BN and monolayer graphene (100 mV, 200 pA, 9 nm × 9 nm). Atomic resolution over both areas is most probably achieved due to functionalization of the tip with an adsorbed species. The direction of the graphene lattice is shown as guide to the eye with a blue line.

Further evidence for the graphene layer on top of the heterostructure can be found by investigating adjacent regions of monolayer graphene on Pt(111) and comparing those with the findings on the heterostructure in Figure 4.5. In contrast to the results on the moiré, atomic resolution of the complete honeycomb carbon lattice could be achieved on the monolayer graphene regions, allowing for comparison of the lattice directions of the graphene lattice with structure B found on the moiré and therefore the graphene direction on the heterostructure as they are rotated by 30 ° with respect to each other (Figure 4.5(c)). Indeed, the monolayer graphene and the graphene direction on the heterostructure share the same orientation as indicated with the blue lines in Figure 4.5 (b,c). On monolayer graphene,the inner part of the graphene C_6 hexagons are visible as depressions.

In rare cases it was possible to image the atomically resolved graphene lattice on the heterostructure with elevated tip-sample distances (Figure 4.5(d)). This can be achieved by accidentally picking up an adsorbed species, which consequently functionalizes the tip, revealing the same orientation for the graphene lattices on the monolayer and on the heterostructure. These findings together with the comparable lattice constant of structure B with a $(\sqrt{3} \times \sqrt{3})R30°$ superstructure with respect to the graphene lattice, strongly indicate the origin of structure B in a continuous top graphene layer spanning from the heterostructure to adjacent regions of monolayer graphene.

Additionally, at the edge of the heterostructure a transition region of $\approx 2\,\mathrm{nm}$ width emerges, where additional protrusions (red asterisks) are visible (Figure 4.5 (a)). The protrusions share the same periodicity of $\approx 0.45\,\mathrm{nm}$ and orientation as structure A, which is only observed on parts of the heterostructure, where a clear moiré is present. While structure A is only imaged with increased tunneling currents, the protrusions in the transition area are discernible at standard tunneling currents of 100 pA. One explanation for the protrusions could be the presence of additional Pt atoms, which are residuals of the growth process. The inset shows a side-view of the transition region, with a continuous graphene layer at the edge of an h-BN flake up to the next Pt(111) terrace. A possible partial delamination of the graphene sheet at edges of the heterostructure will become important later in the observation of phonons in the transition region.

Performing a 2D-FFT of an STM image of the heterostructure with reduced

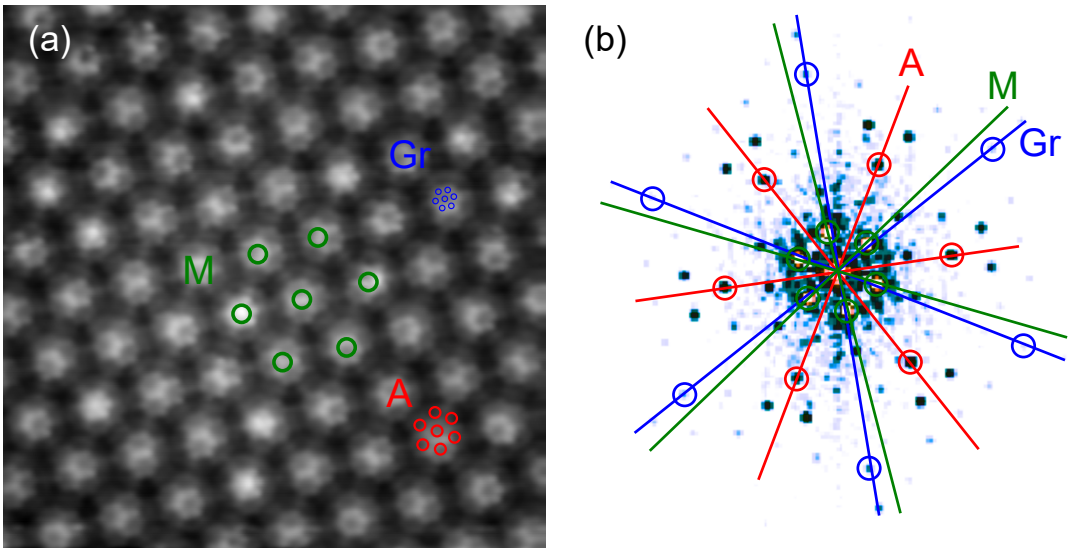

Figure 4.6: (a) STM image of the hetereostructure with decreased tip-sample distance. The image has been rescaled according to STM images of the atomically resolved graphene lattice (10 mV, 200 nA, 13.5 nm × 13.5 nm). (b) 2D-FFT of the STM image in (a). Spots for the moiré M (green circles), structure A (red circles) and graphene (blue circles) are marked, as well as lines indicating the direction of each individual hexagonal structure. Additional spots around the marked spots are replica of the moiré structure M.

tip-sample distance in Figure 4.6 (a) reveals the relative twist angles of structures A/B, graphene and M. The twist angle between A/B and the graphene lattice is found to be 30°, while structure alpha has a $\sqrt{3}$ times larger lattice constant compared to the graphene lattice, revealing the $(\sqrt{3} \times \sqrt{3})R30°$ superstructure of A/B regarding the graphene lattice, as described above. The moiré on the heterostructure is twisted by $\approx -5 \pm 2°$ with respect to the graphene lattice, revealing an approximately $(6.7 \times 6.7)R - 5°$ superstructure.

While the inner part of most graphene C_6 hexagons are imaged as protrusions on the heterostructure, not all graphene C_6 hexagons are imaged in such way in the STM experiments. The additional superstructure A with a $(\sqrt{3} \times \sqrt{3})R30°$ geometry with respect to the graphene lattice is only visible on the heterostructure, which is a surprising observation and will be examined after discussing the role of the h-BN layer on the observed structure by developing a model of the presented system.

4.3 Model and Calculations

To achieve a better understanding of the experimental observations, a model consisting of the Pt(111) substrate as well as a single h-BN and graphene layer stacked on top of each other is developed in the following. The successful intercalation of Pt(111) below h-BN as well as the presence of monolayer graphene in adjacent regions to the observed moiré pattern gives a rationale that the investigated system is indeed a heterostructure composed of a bottom layer h-BN and a top layer graphene.

Two possible origins of the moiré can be considered. First, the moiré could result from the interaction of the top graphene layer with the underlying h-BN sheet. A geometric model of both atomic lattices with a twist angle of $\varphi = 8.5°$ (Figure 4.7(a)) and $\varphi = -8.5°$ (Figure 4.7(b)) between graphene and h-BN is presented, which is the calculated twist angle for the observed moiré periodicity of $\approx 1.65\,\mathrm{nm}$ (see also Chapter 2.6). The orientation of the graphene lattice is modeled according to the experimental results. The resulting moiré lattice is twisted by $\theta \approx -20°$ in Figure 4.7(a) and by $\theta \approx 20°$ in Figure 4.7(b) with respect to the graphene $\langle 11\bar{2}0 \rangle$ direction, which is not in agreement with the experimental observed twist angle of $\theta_{exp} \approx 5°$. A 2D-FFT of the modeled structures is shown in the respective insets in Figure 4.7(a) and Figure 4.7(b) and does not match the observed moiré structure (green circles). Therefore the emergence of the moiré is not the result of the interaction of graphene and h-BN.

Another possible explanation for the observed moiré structure is, second, the interaction of the h-BN layer with the Pt substrate. Here, twist angles of $\varphi = 7°$ (Figure 4.7(c)) and $\varphi = -7°$ (Figure 4.7(d)) between h-BN and Pt have been used to model the experimentally observed heterostructure. Again, the twist angles have been chosen to represent the moiré periodicity of $\approx 1.65\,\mathrm{nm}$. The Pt$\langle 110 \rangle$ direction has been selected to align the calculated and experimentally observed moiré pattern while keeping the Pt direction in the experimentally observed range (Appendix A). Here, the 2D-FFT of the modeled structure in Figure 4.7(c) with a twist angle of $\varphi = 7°$ does not coincide with the observed moiré structure, while the model in Figure 4.7(d) with a twist angle of $\varphi = -7°$ indeed matches the experimental findings. Small deviations ($\leq 4°$) between the measured angles of the moiré were present comparing different heterostructures

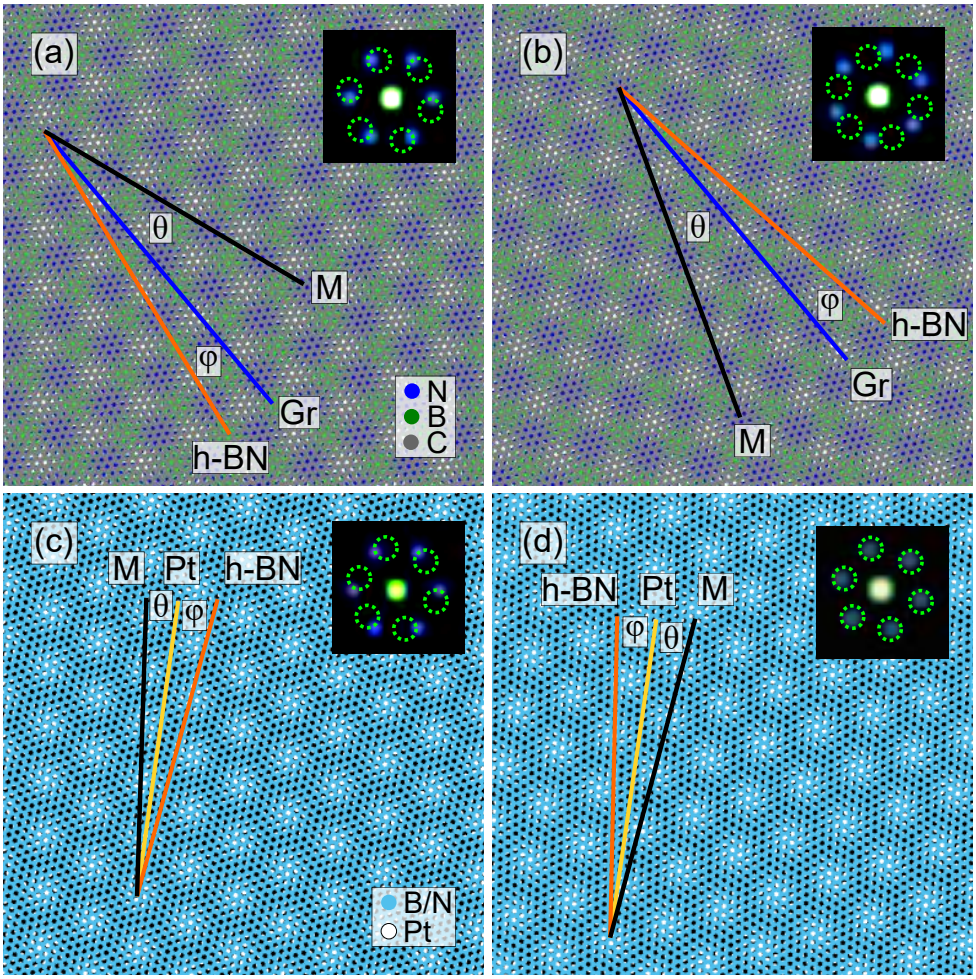

Figure 4.7: Geometric model of the two possible origins of the observed moiré pattern. (a) Graphene on h-BN with a twist angle of $\varphi = 8.5°$. The colors of the individual atoms are indicated. (b) Graphene on h-BN with a twist angle of $\varphi = -8.5°$. (c) h-BN on Pt with a twist angle of $\varphi = 7°$. The colors of the individual atoms are indicated. (d) h-BN on Pt with a twist angle of $\varphi = -7°$. The size of the images is 14 nm × 14 nm. The lattice directions of each moiré as well as the graphene and h-BN $\langle 11\bar{2}0 \rangle$ and Pt $\langle 110 \rangle$ directions are indicated.

on the sample surface, which can be explained by a possible small strain in the h-BN lattice, which is not considered in the presented geometric model, as well as the influences of neighboring areas, which can lead to small distortions of the observed moiré structure in the STM images by small changes in the atomic stacking.

The described thoughts lead to the conclusion that the moiré of the heterostructure originates from the h-BN/Pt(111) interface, with a relative twist angle of $\approx -7^\circ$ between the h-BN and the Pt(111) lattices. Indeed, it was previously reported for bilayer graphene on Pt(111) [116] and Ru(0001) [91] that the observed moiré stems from the interaction of the bottom graphene layer with the metallic substrate.

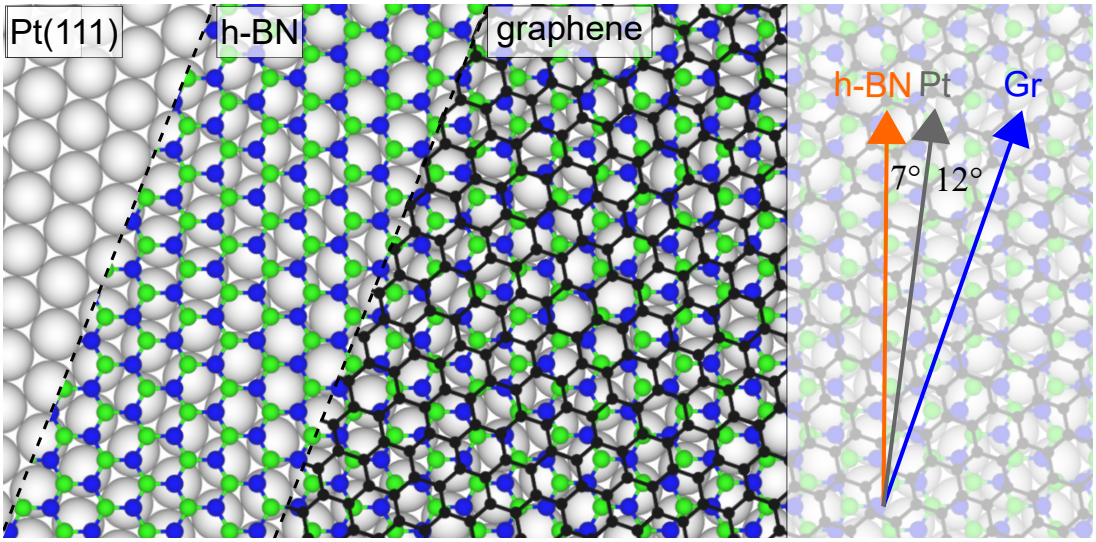

Figure 4.8: Model of the presented system depicted from the aforementioned STM results. The Pt(111) substrate (light grey) as well as a single layer h-BN (green/blue) covered by a single graphene sheet (black) are shown with their relative twist angles.

As the twist angle of h-BN and graphene regarding the Pt(111) substrate are now known, the model of the complete heterostructure can be generated as shown in Figure 4.8. The Pt(111) substrate (light grey) as well as a single layer h-BN(blue/green) covered by a single graphene sheet (black) are shown with their relative twist angles.

This model can now be used to perform DFT calculations, which are compared with the results of the STM experiment (Figure 4.9).

DFT calculations based on plane-wave basis sets of 400 eV cutoff energy were performed with the Vienna *ab initio* simulation package (VASP) [128, 129]. The Perdew-Burke-Ernzerhof (PBE) exchange-correlation functional [130] was employed. The electron-ion interaction was described within the projector augmented wave (PAW) method [131] with C ($2s$, $2p$), B ($2s$, $2p$), N ($2s$, $2p$)

and Pt ($5d$, $6s$) states treated as valence states. The Brillouin-zone integration was performed on Γ-centered symmetry reduced Monkhorst-Pack meshes using a Methfessel-Paxton smearing method of first order with $\sigma = 0.2\,\mathrm{eV}$. The k mesh for sampling the supercell Brillouin zone are chosen to be as dense as 6×6. Dispersion interactions were considered by adding a $1/r^6$ atom-atom term as parametrised by Grimme ("D2" parametrisation) [132].

The system studied in the present work was considered in the supercell geometry due to the relative lattice size mismatch between graphene and the underlying metal. This supercell is constructed from a slab of five layers of metal, a BN layer and a graphene layer adsorbed on one (top) side of a metal slab and a vacuum region of approximately 20 Å. The lattice constant in the lateral plane was set according to the optimized value of free-standing graphene ($a_{gr} = 2.464\,\mathrm{Å}$). The positions ($x$, y, z coordinates) of C, B, N atoms as well as z-coordinates of the two topmost layers of the substrate were fully relaxed until forces became smaller than $0.02\,\mathrm{eVÅ}^{-1}$. The STM images are calculated using the Tersoff-Hamann formalism [38].

The DFT results give rise to a moiré pattern with a very similar periodicity (Figure 4.9(a)) and orientation to the moiré structure found in the STM results (Figure 4.9(b)).

To underline those findings, line scans (yellow line) were performed across both images (Figure 4.9(c,d)). The line scan shows clear peaks of the moiré spots (marked with green dashed lines) as well as smaller peaks between the moiré spots, which will be referred to as "bridge" sites (orange lines in Figure 4.9(b)). Minima between moiré and bridge sites are marked with a orange dashed line in the linescan. Corresponding sites have been marked with green/orange dots in the DFT and STM images. For comparison the dashed lines from Figure 4.9(d) have been superimposed to the line scan of the DFT calculations (Figure 4.9(c)) revealing a good agreement of the experimental data with the calculated results.

The DFT calculations show a good agreement for the moiré observed on the heterostructure in the STM experiment using the described model, which was developed on the basis of the h-BN/Pt(111) interaction as the origin of the moiré pattern.

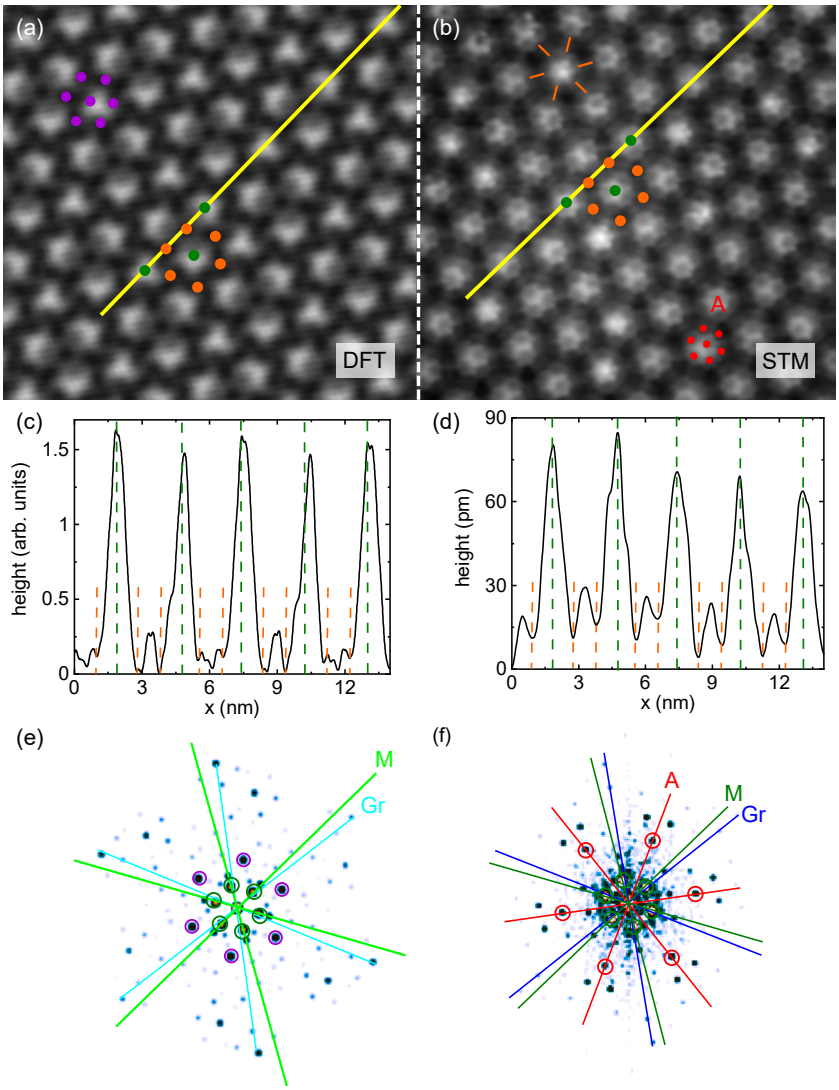

Figure 4.9: Comparison of the DFT calculations on basis of the presented model (Figure 4.8) with the STM data. (a) DFT calculations for the model presented in Figure 4.8 (50 meV, high smearing, 12.7 nm × 13.5 nm). Green (orange) dots indicate maxima (minima) on the moiré. The additional superstructure, which most likely is a result of the graphene/h-BN moiré is represented with purple dots. (b) STM image of the heterostructure with decreased tip-sample distance (10 mV, 200 nA, 12.7 nm × 13.5 nm). Green (orange) dots indicate maxima (minima) on the moiré. Bridge sites are shown as an orange line. (c) Linescan along the yellow line in (a). (d) Linescan along the yellow line in (b). Green (orange) dashed lines indicate maxima (minima) along the linescan. (e) 2D-FFT of the DFT calculations with less smearing. Directions of the moiré (green) and graphene (blue) are indicated. The additional superstructure is marked with purple circles. (f) 2D-FFT of the STM image. Directions of the moiré (green), Structure A (red) and graphene (blue) are indicated.

However, also an additional structure with a periodicity of $\approx 0.75\,\mathrm{nm}$ is visible in the DFT calculations. The structure is marked with purple circles in the FFT of the DFT (Figure 4.9(e)) and is a $(3 \times 3)R16^\circ$ superstructure with respect to the graphene lattice. Calculating the moiré periodicity of graphene and h-BN with their relative twist angle of 19° results in a periodicity of 0.75 nm, which is in agreement with the additional superstructure found in the DFT calculations and therefore most likely a result of the graphene/h-BN interaction. Comparing the graphene/h-BN moiré with the STM images, only a partial match is found in the depressions between the h-BN/Pt(111) moiré sites marked with dashed orange lines in the linescans (Figure 4.9(c,d)). Small deviations could again be explained by small strains and by deviating orientations in the atomic stacking observed in the experiments.

The graphene/h-BN moiré is also visible on the h-BN/Pt(111) moiré spots in the DFT calculations, but it does not coincide with structure A found in the STM experiments, which is only visible while imaging with a reduced tip-sample distance.

As the graphene lattice appears to be continuous over adjacent regions of the heterostructure and monolayer graphene, additional considerations have to be taken into account to explain the observed structures in the STM experiment. At the time of writing this dissertation, the following explanations are considered:

First, a reconstruction of the intercalated Pt on the Pt(111) surface was tested as a possibility to explain the observed results. In that case the moiré structure would be due to different stacking regions of Pt adatoms on the Pt(111) surface separated by soliton walls. Different Pt reconstructions were reported previously on pristine metal substrates, where line and star shaped structures are formed by evaporated Pt atoms [133–136]. Additionally, a large Pt reconstruction under monolayer graphene has been reported on Pt(111) using the same sequential CVD growth method with intermediate Pt layers as described in this chapter for the growth of bilayer graphene [89]. The same reconstruction below regions of monolayer graphene has also been found on the surface used in the present experiment for the growth of graphene on h-BN. However, the moiré on the heterostructure has a ≈ 5 times smaller periodicity than the observed reconstruction of Pt below monolayer graphene. This would lead to very small transition regions from hcp to fcc stacking of the surface atoms inducing a lot of strain. Indeed,

this proposed model was not stable in attempts to perform DFT calculations, making this possible mechanism unlikely.

Second, another possible route to explain structure A could be found in the observation at the edge regions of the observed moiré (Figure 4.5 (a)). The visible protrusions have the same periodicity and orientation as structure A, which are marked with red asterisks in Figure 4.5 (a,b), and could therefore be single Pt atoms between the graphene and h-BN layers. Due to the used sequential growth by Pt intercalation it can not be fully excluded that single Pt atoms are arranged between the h-BN and the graphene layer in such way that they form a $(\sqrt{3} \times \sqrt{3})R30°$ superstructure with respect to the graphene lattice. Therefore, the interaction between the Pt atoms and graphene changes its electronic structure in such way that C_6 rings above a Pt atom are imaged as depression and as a conclusion could be the origin of structure A in the graphene lattice. Another hint for this theory is that depressions of structure A in some rare cases appear as protrusions like in B as can be seen in Figure 4.6 (a), which could indicate a missing Pt atom between graphene and h-BN. A similar $(\sqrt{3} \times \sqrt{3})R30°$ intercalation geometry with respect to the graphene lattice was previously reported for other intercalants like Li below graphene on Ir(111) [137] and SiC [138]. However, this possible explanations seems to be unlikely as well, as the preliminary experiment already showed the complete Pt intercalation below the h-BN layer.

4.4 Phonons at the Domain Boundaries

As discussed before, at the edge of the heterostructure regions an area of $\approx 2\,\mathrm{nm}$ width emerges, in which protrusions with a periodicity of $\approx 0.45\,\mathrm{nm}$ in a hexagonal arrangement are visible (asterisks in Figure 4.5(a)). These protrusions share the same orientation and periodicity as structure A, which is observed for increased currents on the heterostructure. While A only appears with increased tunneling currents, the protrusions in the transition area are discernible at standard tunneling currents of 100 pA.

Spatially resolved $\mathrm{d}I/\mathrm{d}V$ spectra (Figure 4.10(b,c)) recorded over the boundary regions between the graphene/h-BN heterostructure and monolayer graphene reveal steps in the differential conductance at bias voltages corresponding to phonon excitations. The position of the STM tip prior to opening the feedback loop and spectra acquisition is indicated with colored dots in the STM image (Figure 4.10(a)). Comparing the spectra taken directly in the transition region with the ones farther away, the strongest change in intensity

$$\Delta\left(\frac{\mathrm{d}I}{\mathrm{d}V}\right) \equiv \frac{\left(\frac{\mathrm{d}I}{\mathrm{d}V}\right)_{\max} - \left(\frac{\mathrm{d}I}{\mathrm{d}V}\right)_0}{\left(\frac{\mathrm{d}I}{\mathrm{d}V}\right)_0}$$

of the $\mathrm{d}I/\mathrm{d}V$ signal is found directly on the transition regions with an increase in signal strength of $\approx 10\,\%$. The intensity change is reduced to $\approx 5\,\%$ ($\approx 8\,\%$) placing the tip at greater distance to the transition region on the monolayer graphene (heterostructure). Conclusively, the phonon signal strength is reduced by up to 50 % on monolayer graphene.

Stronger phonon signals have been reported for graphene nanobubbles on Pt(111) [139] and blisters of graphene on Ir(111) [140]. A possible increased distance of the graphene layer in the transition regions could be explained by intercalated Pt atoms, as discussed above and could therefore lead to an increased phonon signal in the $\mathrm{d}I/\mathrm{d}V$ spectra.

The energy of the phonons can be extracted by performing the second derivative of the $\mathrm{d}I/\mathrm{d}V$ spectra. A selection of $\mathrm{d}^2I/\mathrm{d}V^2$ spectra, representing the transition region (green), the heterostructure (yellow) and monolayer graphene (dark gray), is shown in Figure 4.10(d). The resulting peaks and dips reveal phonon signatures at energies of $6 \pm 1\,\mathrm{meV}$ and $41 \pm 1\,\mathrm{meV}$, respectively.

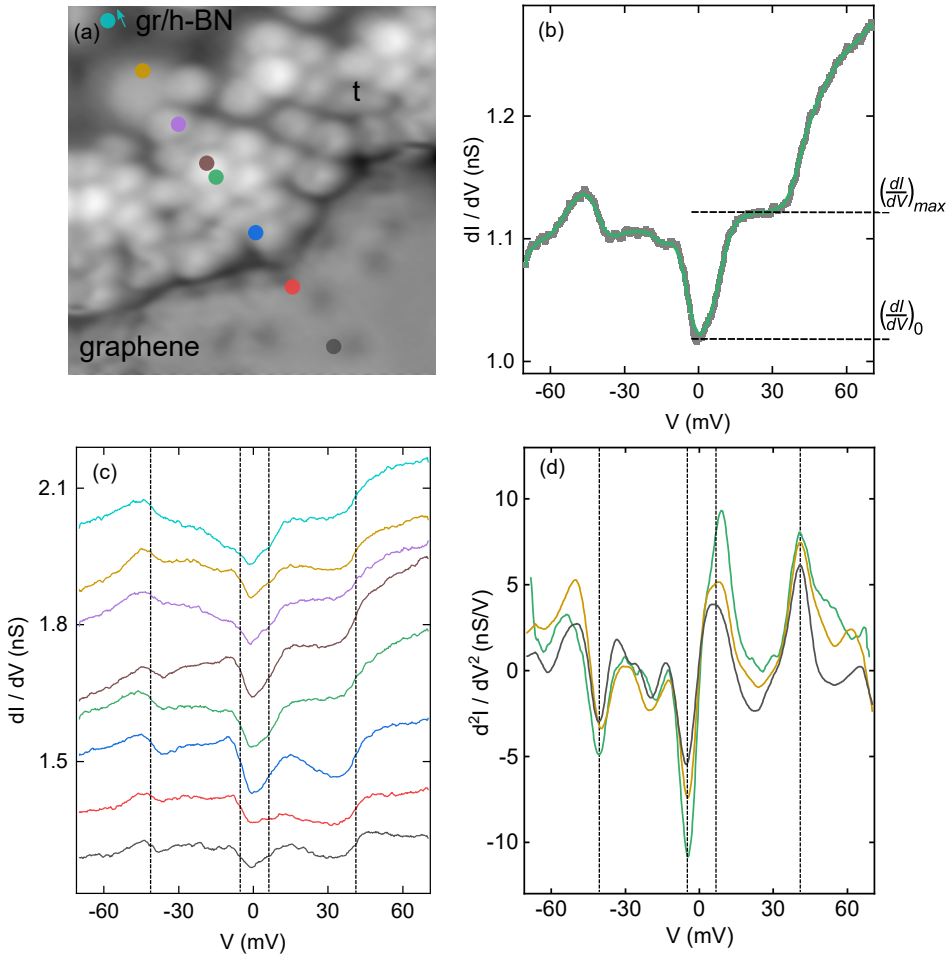

Figure 4.10: (a) STM image of the transition region from monolayer graphene to the heterostructure (70 mV, 100 pA, 8 nm × 8 nm). The tip position prior to spectra acquisition is indicated with colored circles corresponding to the respective spectrum. (b) Smoothed $\mathrm{d}I/\mathrm{d}V$ spectrum recorded in the transition region (t) indicated by the green dot (tunneling parameters before opening the feedback loop: 70 mV, 100 pA, 5 mV, 754 Hz). Raw data is shown as dots. (c) Spatially resolved $\mathrm{d}I/\mathrm{d}V$ spectra across the transition region from the graphene/h-BN heterostructure to monolayer graphene (tunneling parameters before opening the feedback loop: 70 mV, 100 pA, 5 mV, 754 Hz). The spectra are offset for clarity and phonon excitations are marked with dashed lines. (c) Smoothed $\mathrm{d}^2I/\mathrm{d}V^2$ spectra as the result of the numerical derivative of selected spectra shown in (c). The phonon excitations are marked with dashed lines.

Those experimental findings are compared to other IETS experiments, as well as calculations, on graphene and graphene/h-BN heterostructures in the following.

First principle calculations by Slotman *et al.* [141] for graphene, h-BN and graphene/h-BN heterostructures reveal phonon branches with distinct energies. The main results of these DFT calculations for monolayer (solid red line) and bilayer (blue dashed line) graphene/h-BN are shown in Figure 4.11(a,b). The lowest phonon branch of h-BN is almost flat over the M-K range, while for graphene the lowest mode at the K-point is fourfold degenerated. In the case of h-BN, the degeneracy is lifted because of the two different atoms in the h-BN unit cell.

In Figure 4.11(c) the phonon dispersion of the heterostructure of graphene and h-BN is shown. The heterostructure is nearly the superposition of the results obtained for h-BN and graphene. Phonon branches with contributions of either h-BN or graphene are marked according to the colorscale in Figure 4.11(c). The respective modes are localized at each layer with exception of the acoustical modes at the Γ-point.

Phonons at the K-point within the graphene/h-BN heterostructure with an energy of 37.1 meV correspond to out-of-plane displacements of the nitrogen and boron atoms, which are more likely to couple to the graphene layer on top of the h-BN layer [141].

The combination of the flat phonon dispersion at the K-point and the out-of-plane displacement are likely contributing factors to the observed phonon in the $\mathrm{d}I/\mathrm{d}V$ spectra.

The experimentally observed phonon excitations (marked with green horizontal lines in Figure 4.11) in the $\mathrm{d}I/\mathrm{d}V$ spectra can now be compared to the calculations. The mode at ≈ 6 meV could correspond to the Γ-point LA mode of graphene or h-BN, which anticross due to the coupling close to the Γ-point. A similar observation has previously been made on graphene-covered Ir(111), where the ZA mode of graphene at the Γ-point shifts to an energy of ≈ 6 meV [142].

The second phonon mode at ≈ 41 meV is in close vicinity to the flat band of the out-of-plane K-point LA phonons with an energy of 37.1 meV, which is the most likely h-BN mode to couple to graphene due to its out-of-plane displacement and therefore can be probed by the STM tip above the top graphene layer.

In another study of graphene/h-BN heterostructures a shift of the h-BN K-point phonon up to a higher energy of ≈ 46 meV has been reported [143]. Here,

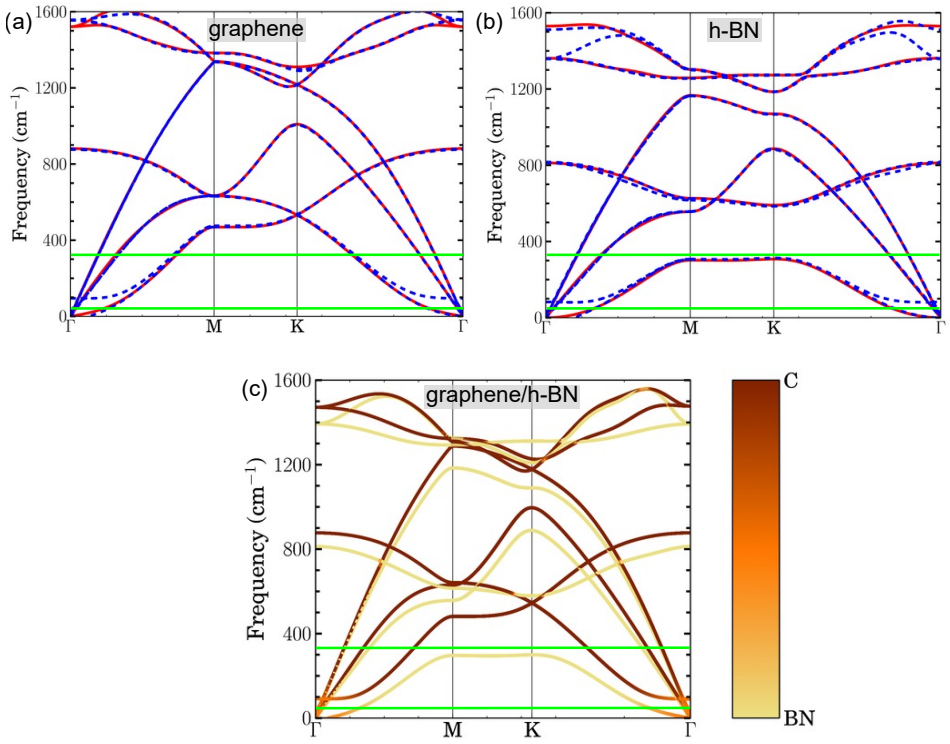

Figure 4.11: Calculated phonon spectra of (a) graphene single-layer (red, solid) and bilayer (blue, dashed), (b) h-BN single-layer (red, solid) and bilayer (blue, dashed), (c) Phonon dispersion of a graphene/h-BN bilayer. The experimentally observed phonon modes are marked with green lines. Figure adapted from *Annalen der Physik, Volume: 526, Issue: 9-10, Pages: 381-386, First published: 15 September 2014, DOI: (10.1002/andp.201400155)* [141].

an upward shift of the ZA Γ-point graphene phonon to ≈ 36 meV is also observed. A comparison between AA and AB stacked graphene/h-BN heterostructures reveals a stronger influence on the out-of-plane phonons for the AA stacked heterostructure in comparison to the AB stacking.

Additionally, the twist angle could influence the energy of the observed phonons. It has been previously reported that the twist angles of bilayer graphene or graphene/h-BN heterostructures can influence the observed phonon energies [144–149]. As the graphene layer is rotated by ≈ 19° with respect to h-BN, a change of the phonon energies therefore could be expected.

Taking the theoretical considerations for the graphene/h-BN heterostructure into account, the experimentally observed value of ≈ 41 meV lies well within the reported range of h-BN phonons and can be assigned to the out-of-plane phonon

of h-BN at the K-point, while the mode at 6 meV can be assigned to either a graphene or h-BN mode at the Γ-point.

While the occurrence of hybrid graphene/h-BN phonon modes on the stacked heterostructure is reasonable, the observation of such spectroscopic signatures is unexpected on graphene alone. The spatially resolved spectra of Figure 4.10 reveal that distances of ≈ 5 nm from the transition region (t) are required in order to push the hybrid-phonon signal below the detection limit.

At the time of writing the dissertation a clear-cut explanation to this surprising experimental finding remains elusive. A tentative rationale, however, can be offered in the light of recent non-equilibrium electron transport calculations [150] where the signal strength of graphene phonons reflects the balance between inelastic and elastic transport channels. To efficiently excite graphene phonons the inelastic tunneling electron propagates in the graphene lattice before it hops to the hosting metal substrate. This picture may be transferred to the present situation where the tunneling electron injected into graphene travels to surface regions with the graphene/h-BN stacking and excites hybrid phonons.

Another possible explanation resorts to the transport of information mediated by the substrate electronic structure. A spectacular example is the quantum mirage effect observed in elliptical atom corrals on a substrate that hosts a Shockley surface state [151]. In this seminal publication it was shown that the Abrikosov-Suhl-Kondo resonance of a Co atom adsorbed at one focus of the elliptical corral is likewise observed at the other unoccupied focus. Very recently a Kondo-free mirage effect has experimentally been demonstrated for Fe and Ag atoms in atomic corrals on Ag(111) [152]. The electronic structure of an atom in one focus can be reproduced in the other focal point even in a wide energy range. A possible focus-to-focus transport of vibrational signatures of a Kondo impurity was previously conjectured by revealing line shape variations of the Abrikosov-Suhl-Kondo resonance at the empty focal point of an atomic corral [153].

In the present case of a graphene/h-BN layer transitioning into a monolayer of graphene, the information of hybrid phonon modes may be communicated by a surface-state-electron propagation. It is well known that in the vicinity of step edges or other scattering centers standing electron wave patterns form and help propagate spectroscopic information to distant positions. More detailed

experiments must be carried out in order to confirm this scenario. In particular, a dense line of point spectroscopy will enable to unveil a possible oscillation of the phonon signal strength as a function of the distance from the transition region. The natural spatial period of such oscillations is the Fermi wavelength of involved surface-state electrons.

4.5 Conclusions

A possible method to fabricate heterostructures of graphene and h-BN by the sequential growth on an intermediate Pt layer has been developed. The successful intercalation of Pt beneath h-BN as well as the presence of graphene on the surface indicate the suitability of this preparation technique. Additional to a moiré resulting from the h-BN and Pt(111) interaction, an unexpected hexagonal structure emerges on the heterostructure by lowering the tip-sample distance. At the time of writing this thesis different reconstructions of residual Pt atoms were considered to explain this observed structures. In the transition regions of the heterostructure to monolayer graphene phonon signals have been observed, which most likely originate from out-of-plane h-BN phonons at the K-point and subsequently couple to the top graphene layer.

CHAPTER 5

Molecular Adsorbates on Buffer Layers

Partly reproduced from J. Vac. Sci. Technol. A 37, 061404, 2019, with permission from AIP Publishing,
and from J. Phys. Chem. Lett. 11, 5204-5211, 2020, with permission from ACS Publications.

The use of intermediate buffer layers has been proven successful in retaining atomic and molecular quantum states which otherwise would inevitably be quenched due to hybridization with the substrate. Oxide and nitride thin films, alkali halide and alkane layers, molecular platforms and two-dimensional materials have so far been used as buffer layers for probing genuine vibronic [11, 12, 14–17, 154–161], electronic [162–170], magnetic [171–177], optical [5, 178–188] and chemical [88, 189–193] properties of single atoms and molecules.

However, some finite coupling of the adsorbed atom or molecule to the buffer layer and to the substrate surface remains. How does the residual interaction manifest itself? Very often the degree of decoupling is judged by comparing resonance energies and widths of the adsorbed species with their counterparts of the free object [162, 163, 167–170, 194, 195], by scrutinizing details of the spectroscopic line shape of vibrational excitations [196] or analyzing the molecular adsorption configuration [197, 198]. To further characterize the buffer functionality, investigations into the decoupling behavior of a buffer layer on different surfaces as well as into a possible site-dependent decoupling are desirable.

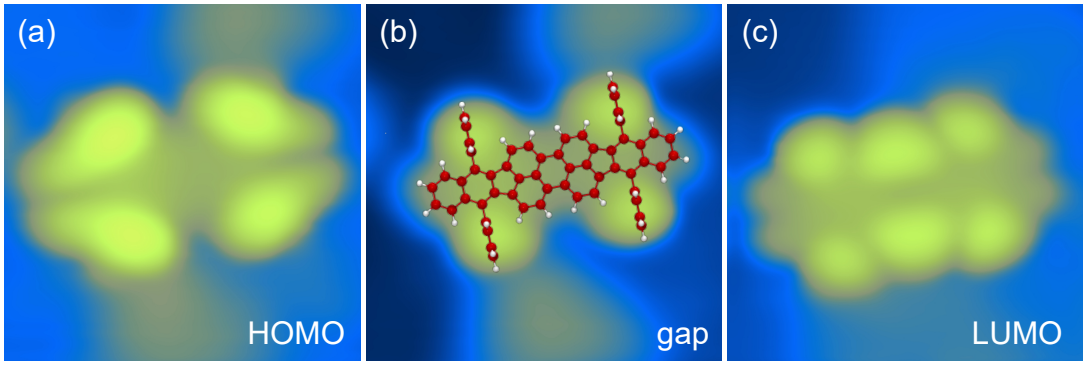

Figure 5.1: STM images of DBP adsorbed on graphene-covered Ru(0001) at the bias voltage corresponding to the energetic position of the (a) HOMO (−2.5 V, 60 pA, 3.5 nm × 3.5 nm) (b) HOMO-LUMO gap (−1 V, 60 pA, 3.5 nm × 3.5 nm) (c) LUMO (1 V, 50 pA, 3.5 nm × 3.5 nm). A ball-and-stick model of DBP is superimposed in (b).

In this chapter the influence of different buffer layers on the extend of hybridization of the organic molecule DBP ($C_{64}H_{36}$, 5,10,15,20-tetraphenylbisbenz[5, 6]-indeno[1, 2, 3−cd:1′, 2′, 3′−lm]perylene) and the two metal substrates Pt(111) and Ru(0001) will be explored. The discussion will be presented in two parts. The first part will be restricted to the energetic position of the DBP frontier orbitals and the effect of its different adsorption positions on the h-BN layer compared between Pt(111) and Ru(0001). Subsequently, the change of vibrational properties of DBP adsorbed on graphene and h-BN will be compared, unraveling different extends of coupling to the two metal substrates.

Due to the spatially localized nature of the HOMO at the four phenyl groups of the DBP molecule (Figure 5.1(a)) and the LUMO at the side of the molecular backbone (Figure 5.1(c)) both frontier orbitals can be probed individually ($\mathrm{d}I/\mathrm{d}V$ maps of DBP recorded in constant height mode are shown for comparison in Appendix C). In the gap region the molecular backbone appears darker than the four phenyl groups of DBP and exhibits a uniform contrast, hinting a parallel adsorption of DBP [199, 200].

5.1 Molecular Orbitals upon Adsorption on Two-Dimensional Materials

The two-dimensional materials hexagonal boron nitride (h-BN) and graphene are investigated on Pt(111) and Ru(0001) to demonstrate that the extent of decoupling depends on the metal surface and in the case of h-BN on the specific h-BN moiré site. To this end, the frontier orbitals – highest occupied molecular orbital (HOMO) and lowest unoccupied molecular orbital (LUMO) – of single adsorbed DBP are used. Their signatures in spectra of differential conductance ($\mathrm{d}I/\mathrm{d}V$) exhibit energy shifts depending on the adsorption site of the molecule. While for h-BN on Pt(111) a rigid shift of HOMO and LUMO with an invariant HOMO–LUMO gap is observed, h-BN-covered Ru(0001) gives rise to a nonuniform shift of the frontier orbitals. Additionally, the energy of HOMO and LUMO, as well as their linewidths, are compared for DBP adsorbed on both two-dimensional materials.

5.1.1 Experimental Details

The preparation of the metallic crystals is described in Chapter 2.4. The growth procedure for hexagonal boron nitride using borazane and for graphene using etylene on Pt(111) and Ru(0001) is explained in Chapter 3.1. DBP molecules were deposited at a low temperature of $\approx 10\,\mathrm{K}$ by directing a molecular beam to the sample mounted in the STM. The molecules were sublimated from a Mo crucible heated by an electron beam.

5.1.2 h-BN- and Graphene-covered Pt(111)

The adsorption of DBP molecules on the cold ($\approx 10\,\mathrm{K}$) h-BN-covered Pt(111) surface leads to single adsorbed molecules (Figure 5.2) with the same characteristic orbital structure explained before. Comparing the STM data of DBP on h-BN-covered Pt(111) with the data obtained for DBP on graphene-covered Ir(111) similar shaped topografic signatures are found [12]. In the analysis of several STM images of various DBP molecules, no preferred adsorption sites or orientations were present. This observation can partly be explained by the

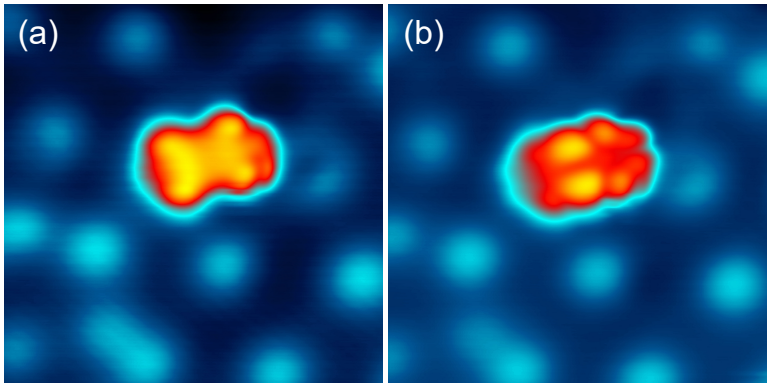

Figure 5.2: STM images of DBP adsorbed on h-BN-covered Pt(111) at the bias voltage corresponding to the energetic position of the (a) HOMO-LUMO gap (1.9 V, 50 pA, 8.5 nm × 8.5 nm) and the (b) LUMO (2.2 V, 50 pA, 8.5 nm × 8.5 nm)

frequent absence of the h-BN moiré superstructure as well as the lack of simultaneous imaging of DBP and the atomic h-BN lattice.

While topographic STM data alone indicate an indifference of the properties of DBP toward h-BN sites, $\mathrm{d}I/\mathrm{d}V$ spectra reveal characteristic changes for different DBP molecules that likely reside at different adsorption sites.

The spectroscopic signatures of HOMO−1, HOMO and LUMO of a specific DBP molecule appear as sharp peaks in $\mathrm{d}I/\mathrm{d}V$ data (Figure 5.3(a)). The reduced linewidth of the molecular orbital signatures and therefore prolonged lifetime of the transient charged molecular state hints at the efficient decoupling of DBP from Pt(111) by the intermediate h-BN layer, which is in agreement with previous work on free-base porphins and Co-phthalocyanines [46, 158]. The spectra recorded for HOMO−1 and HOMO exhibit the strongest signature on the phenyl groups of DBP (left arrow in the ball-and-stick model of DBP in Figure 5.3(a)) while the LUMO is most pronounced recording spectra at the sides of the DBP backbone between the phenyl rings (right arrow). Similar observations were reported for DBP on graphene-covered Ir(111) [12]. Analyzing the difference in energy of the HOMO and LUMO resonances in $\mathrm{d}I/\mathrm{d}V$ spectra, the HOMO–LUMO gap is found to be $\approx 3\,\mathrm{eV}$. This gap is comparable with the value reported for DBP on graphene-covered Ir(111) [12] and lower than the 3.8 eV found for DBP on NaCl-covered Ag(111) [185]. The gap width that reflects the difference in ionization potential and electron affinity and, thus, considers final-state Coulomb effects is expected to be even larger. Adsorption of

a molecule on a surface tends to reduce this gap width due to the polarization of the environment and to the interaction with the molecular image charge (see also Chapter 2.7).

Figure 5.3(b) shows a collection of $\mathrm{d}I/\mathrm{d}V$ spectra obtained from different DBP molecules, where each color used for the (smoothed) $\mathrm{d}I/\mathrm{d}V$ data is assigned to an individual molecule. The molecular resonances HOMO−1, HOMO and LUMO exhibit virtually identical shifts. The maximum (minimum) LUMO energy is $\approx 2.22\,\mathrm{eV}$ ($\approx 1.81\,\mathrm{eV}$), giving rise to a shift of $\approx 0.41\,\mathrm{eV}$. The minimum (maximum) HOMO−1 and HOMO energy is $\approx -2.16\,\mathrm{eV}$ ($\approx -1.74\,\mathrm{eV}$) and $\approx -1.17\,\mathrm{eV}$ ($\approx -0.74\,\mathrm{eV}$), which corresponds to a shift of $\approx 0.42\,\mathrm{eV}$ and $\approx 0.43\,\mathrm{eV}$, respectively. These virtually equal molecular orbital shifts give rise to a rigid shift of each entire spectrum. Spectra of all other DBP molecules, two of which are shown as B and C in Figure 5.3(b), show their molecular orbital resonances within these extremal molecular orbital energies (groups A and D).

The energy shift is comparable to a molecular orbital shift reported from perylenetetracarboxylic-dianhydride (PTCDA) superstructures on Au surfaces [201]. In that report, LUMO and LUMO+1 of a single PTCDA molecule shifted by $\approx 0.35\,\mathrm{eV}$, depending on the molecular superstructure the PTCDA molecule was embedded in [201]. In the present case, however, neighboring molecules reside at large distances, which effectively suppress intermolecular coupling. A Stark shift [202, 203] of the molecular resonances in the electric field between tip and sample can likewise be excluded since all DBP molecules are imaged with the same apparent height at the feedback loop parameters V and I used for spectroscopy.

A justification for the shift becomes evident by comparison to previous studies that reported variations of the local work function of $\approx 0.5\,\mathrm{eV}$ for h-BN on Ir(111) [204], where the highest (lowest) work function was found at the wire (pore) region of the h-BN moiré pattern. Pt(111) and Ir(111) are similar surfaces with respect to their low interaction with h-BN [70, 76]. Therefore, a similar work function variation could apply to h-BN-covered Pt(111) as well. In the case of a weak DBP–surface coupling, which is reasonable because of the absence of preferred adsorption sites on h-BN and sharp molecular resonances in $\mathrm{d}I/\mathrm{d}V$ spectra, molecular energy levels are expected to align with the vacuum energy [205].

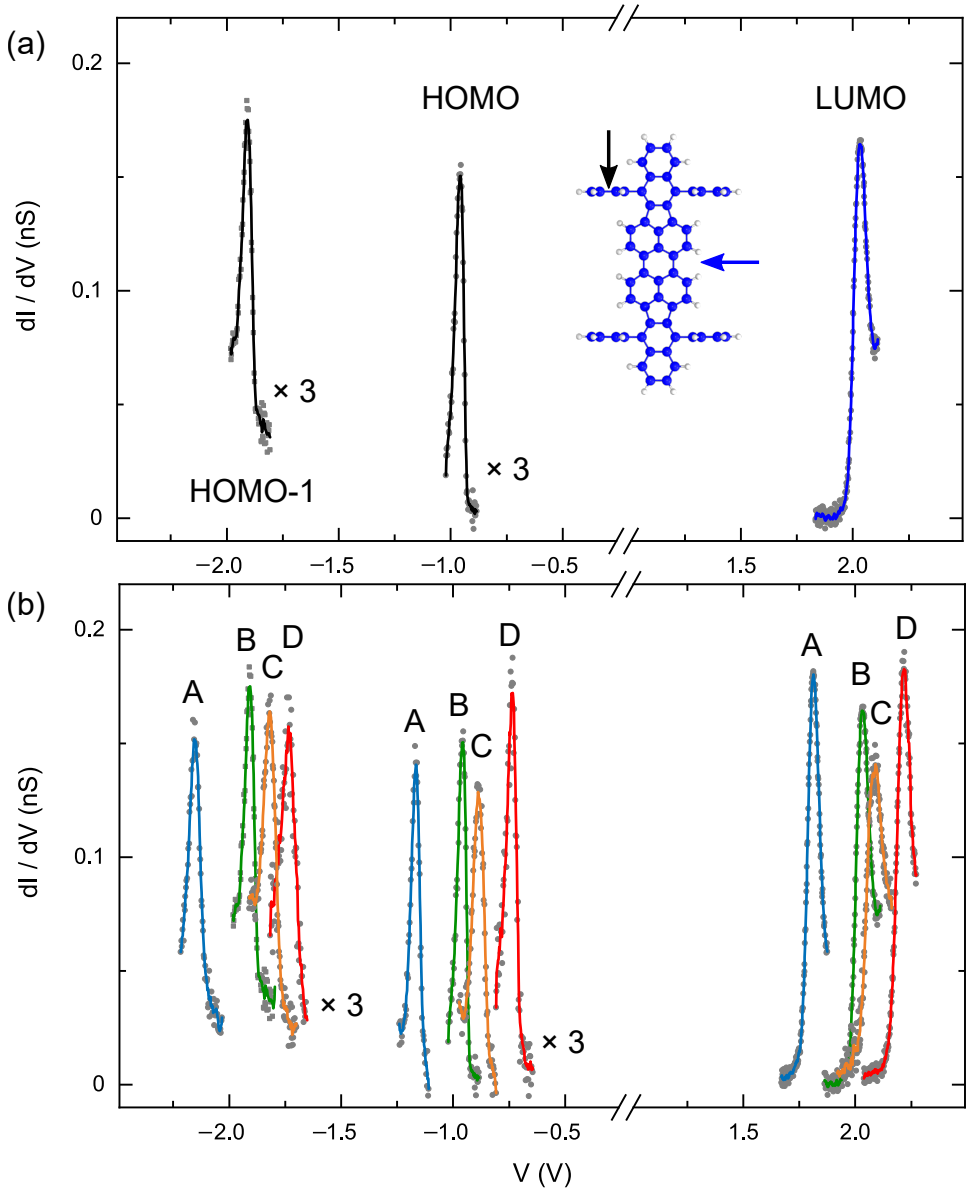

Figure 5.3: (a) $\mathrm{d}I/\mathrm{d}V$ signatures of HOMO−1, HOMO and LUMO for a single DBP on h-BN-covered Pt(111) (feedback loop parameters: −2.5 V, 50 pA for the HOMO−1, HOMO and 2.8 V, 50 pA for the LUMO). The signatures of HOMO−1 and HOMO are dominant on the phenyl groups (left arrow of the sketch), while the LUMO peak appears on the sides of the molecular backbone (right arrow). (b) Collection of $\mathrm{d}I/\mathrm{d}V$ spectra of various DBP on h-BN-covered Pt(111). Orbital resonances of the same molecule are labeled with the same capital letter. In both graphs, raw (smoothed) data appear as dots (solid lines).

The weak hybridization with the surface leads to the invariance of the molecular ionization potential and electron affinity, which allows the molecular orbital energy levels to be sensitive to changes in the vacuum energy, *i. e.*, to changes in the work function. Therefore, the observed rigid shift of the entire $\mathrm{d}I/\mathrm{d}V$ spectra is likely to reflect the local work function changes of h-BN on Pt(111). In particular, $\mathrm{d}I/\mathrm{d}V$ spectra with extremal molecular orbital energies may be attributed to DBP molecules residing at moiré sites with extremal work functions. The group of peaks labeled D (A) in Figure 5.3(b) with the highest (lowest) molecular orbital energies corresponds to DBP molecules adsorbed at the wire (pore) region of the h-BN moiré lattice where the work function is highest (lowest) [204]. Moreover, the presence of molecules with molecular orbital energies in between the extremal energies shows that DBP on h-BN-covered Pt(111) adopts many different sites without preference.

Before discussing the results obtained for h-BN- and graphene-covered Ru(0001), spatial work function changes of h-BN on Pt(111) shall be discussed. A work function map, such as for h-BN on Ir(111) [204], has not been reported for h-BN-covered Pt(111). The measured shifts of frontier orbital energies in $\mathrm{d}I/\mathrm{d}V$ spectra (Figure 5.3) represent the first evidence for local variations of the work function for h-BN-covered Pt(111). Additionally, calculated shifts of the N p_{xy} and B p_{xy} density of states of h-BN on Pt(111) for wire and pore regions were reported as $\approx 0.6\,\mathrm{eV}$ and related to the different charge transfer at these stacking sites, which likewise hints at different local work functions.

For comparison of the DBP properties the other prominent two-dimensional material graphene has been grown on Pt(111). Graphene on Pt(111) (Figure 5.9(c)) exhibits irregularly distributed depressions that are most likely due to Pt(111) lattice vacancies [82] or C impurities embedded in the Pt(111) surface [83]. Moiré patterns are scarcely observed, which reflects the dominance of graphene domains with large rotation angles with respect to the Pt(111) lattice [116, 206, 207]. Moreover, in the case of a visible moiré lattice, its corrugation is significantly lower than on Ru(0001), which reflects the low graphene–Pt hybridization [80, 81]. Preferred adsorption sites of DBP on the graphene covered Pt(111) surface could not be determined due to the weakly visible moiré pattern. For graphene on Pt(111) the HOMO and LUMO spatial distributions of DBP (Figure 5.4(a)) are akin to the data obtained for the molecule on h-BN-

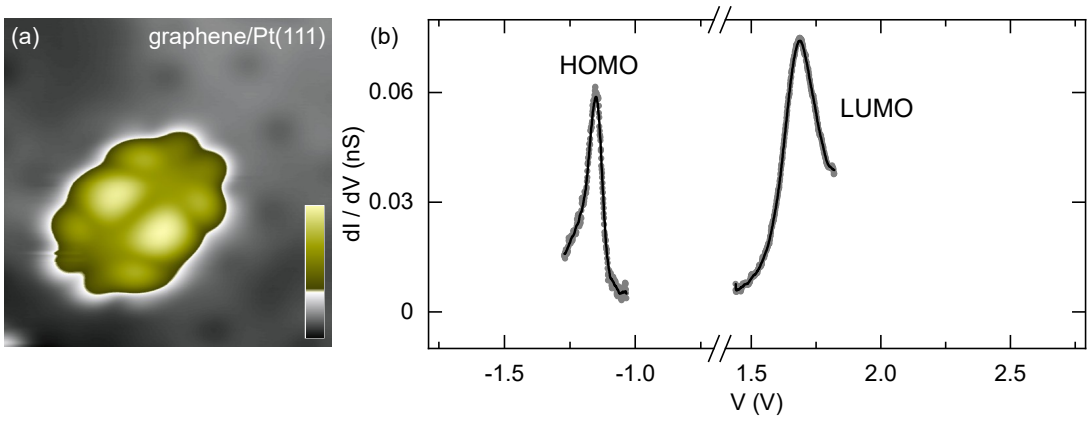

Figure 5.4: (a) STM image of DBP adsorbed on Pt(111) covered with graphene (2.10 V, 15 pA, 5 nm × 5 nm). The color scale ranges from 0 pm (black) to 229 pm (yellow). (b) dI/dV spectra of HOMO and LUMO of DBP adsorbed on graphene-covered Pt(111) (feedback loop parameters: −1.80 V, 20 pA (HOMO); 2.30 V, 20 pA (LUMO); modulation: 5 $\mathrm{mV_{rms}}$, 754 Hz).

covered Pt(111). The dI/dV spectra reveal sharp resonances for the HOMO and LUMO signatures of DBP. The energy of the HOMO (LUMO) is ≈ −1.2 eV (≈ 1.7 eV), which correspond to a HOMO-LUMO gap width of ≈ 2.9 eV. Before comparing the energetic position of HOMO and LUMO of DBP between h-BN and graphene, as well as their linewidths, the results obtained on h-BN- and graphene-covered Ru(0001) are discussed next.

5.1.3 h-BN- and Graphene-covered Ru(0001)

DBP molecules evaporated at low temperatures on the cold (≈ 10 K) h-BN-covered Ru(0001) surface show a clear preference for wire and pore adsorption sites (Figure 5.5). At an applied bias voltage of 0.7 V (Figure 5.5(a)), only DBP at the pore site exhibits the submolecular contrast of the LUMO, while DBP occupying the wire site does not show an intramolecular structure, but instead represents the aforementioned gap structure of DBP. Additionally, at elevated bias voltages of 1.2 V (Figure 5.5(b)) both DBP molecules show the topographic signature of the LUMO. This observation points to a different electronic structure of DBP at the different moiré lattice sites and was investigated by single-molecule dI/dV spectroscopy, as will be discussed below (Figure 5.6).

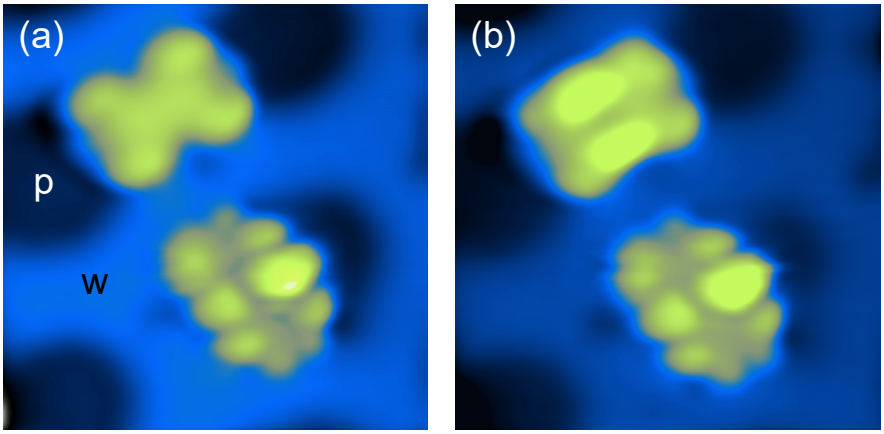

Figure 5.5: STM images of DBP adsorbed on wire (w) and pore (p) sites of h-BN-covered Ru(0001). The molecules appear with different submolecular structure depending on their adsorption position. (a) DBP adsorbed on the wire shows the gap structure while DBP in the pore exhibits the topographic signature of the LUMO. (0.7 V, 50 pA, 6 nm × 6 nm) (b) Both molecules appear with the submolecular structure of the LUMO (Tunneling parameters: 1.2 V, 50 pA, 6 nm × 6 nm).

DBP molecules trapped in the pore regions do not exhibit preferred orientations, while the molecular backbone of DBP atop the wire sites is oriented virtually perpendicular to the wire direction. The trapping of atoms and molecules by the moiré pores of h-BN on Rh(111), which has similar properties to Ru(0001) [76], was previously assigned to their electrostatic anchoring caused by polarization-induced bonding [208]. Statistics of wire and pore adsorption using large-scale STM images of different surface regions revealed no preferred adsorption site of molecules for either wire or pore sites. DBP molecules residing at the wire site were rather immobile, while imaging of DBP at pores was often accompanied by small translations and rotations of the molecule.

Figure 5.6 shows HOMO and LUMO $\mathrm{d}I/\mathrm{d}V$ signatures of DBP adsorbed at wire (Figure 5.6(a)) and pore (Figure 5.6(b)) sites. Additionally, Figure 5.6(b) presents maps of normalized [209] $\mathrm{d}I/\mathrm{d}V$, depicting the approximate spatial distribution of the HOMO and the LUMO, which is similar to results for DBP on h-BN-covered Pt(111) (shown in Appendix C) and in agreement with previous reports for DBP on NaCl-covered Ag(111) [185] and graphene-covered Ir(111) [12]. In particular, the HOMO is characterized by antinodes of its charge density

in the vicinity of the four DBP phenyl groups. It exhibits two nodal lines, one coinciding with the long mirror axis of the molecule and the other oriented along the short mirror axis. The LUMO shows two additional antinodes of its charge density in the DBP center. While a nodal line along the molecular backbone is preserved, two additional nodal lines perpendicular to the long mirror axis separate the central antinodes from the antinodes that are almost centered at the four phenyl groups.

Prior to data aquisition of the $\mathrm{d}I/\mathrm{d}V$ spectra the STM tip was placed at the same intramolecular positions as for DBP on h-BN-covered Pt(111) (Figure 5.3(a)). Correspondingly, different energies for HOMO and LUMO resonances are likewise present for DBP at the different adsorption sites on the h-BN nanomesh. However, HOMO and LUMO resonances shift by an unequal amount. Molecules residing at the wire (pore) exhibit HOMO and LUMO peaks at energies $\approx -1.85\,\mathrm{eV}$ and $\approx 1.2\,\mathrm{eV}$ ($\approx -2\,\mathrm{eV}$ and $\approx 0.7\,\mathrm{eV}$), respectively, which corresponds to a HOMO (LUMO) shift of $\approx 0.15\,\mathrm{eV}$ ($\approx 0.5\,\mathrm{eV}$). The dissimilar shift of HOMO and LUMO energies toward lower values represents a reduction of the HOMO–LUMO gap from $\approx 3\,\mathrm{eV}$ at wire sites to $\approx 2.65\,\mathrm{eV}$ at pore sites, *i. e.*, by $\approx 0.35\,\mathrm{eV}$.

The calculated work function difference of $0.35\,\mathrm{eV}$ between wire and pore regions [210] matches the LUMO shift of $\approx 0.5\,\mathrm{eV}$ reasonably well. However, the unequal shift of the DBP HOMO is no longer compatible with a local variation of the work function alone since in this case, a rigid shift of the entire spectrum and a invariance of the HOMO–LUMO gap is expected, as observed for DBP on h-BN-covered Pt(111) (Figure 5.3(b)). For a qualitative explanation of the dissimilar shift, charge transfer processes between DBP and the h-BN-Ru(0001) surface must be considered as well.

Pore regions of h-BN on Rh(111) were previously demonstrated to exhibit an extended electron transfer from h-BN to Rh(111) compared to wire regions [70]. Assuming a similar situation for h-BN on Ru(0001) and considering that DBP is a donor molecule [211–215], electron-depleted pore regions are likely to accept negative charge from DBP. This charge transfer process would explain a partial depletion of the HOMO and, thus, its shift toward the Fermi energy, *i. e.*, toward $V = 0\,\mathrm{V}$ in $\mathrm{d}I/\mathrm{d}V$ spectra. Therefore, the HOMO and LUMO of DBP on h-BN-covered Ru(0001) may both be subject to a shift induced by local work function

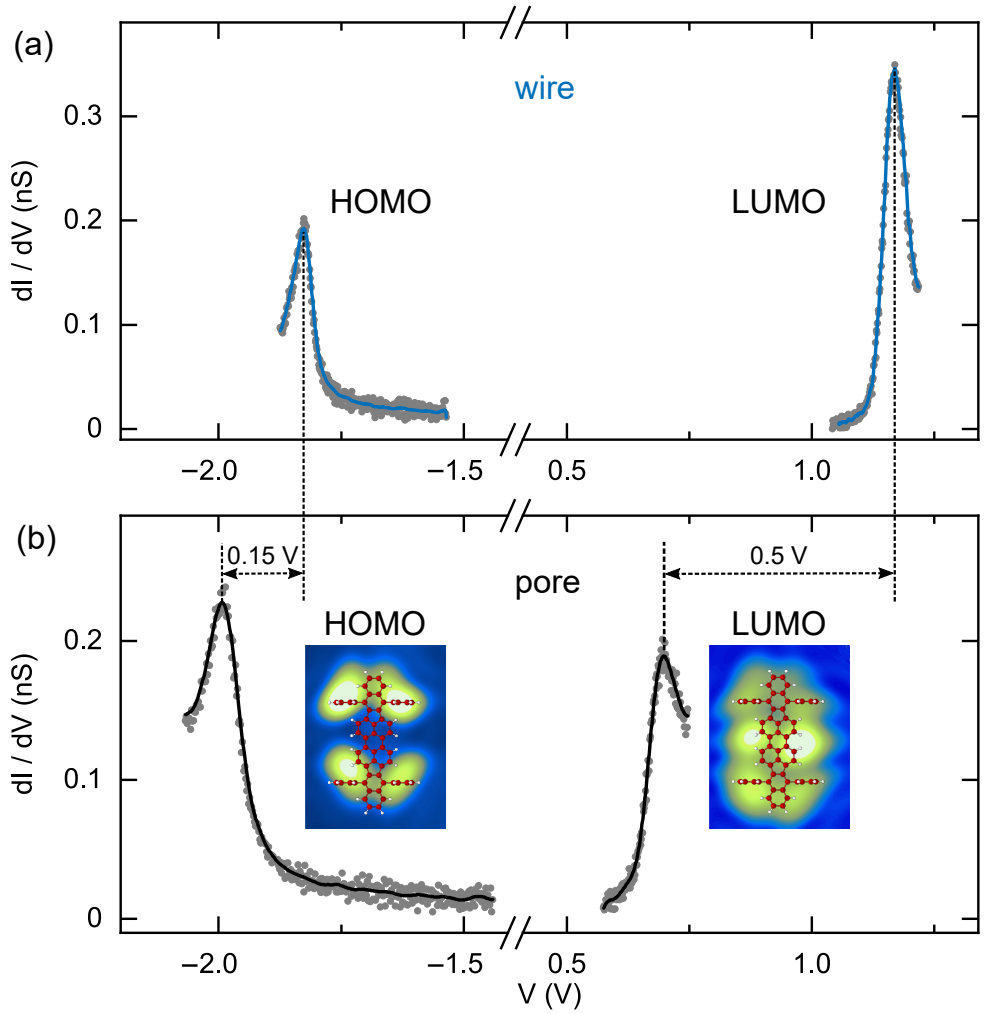

Figure 5.6: $\mathrm{d}I/\mathrm{d}V$ signatures of HOMO and LUMO of DBP adsorbed at the (a) wire and (b) pore regions of h-BN on Ru(0001). Feedback loop parameters: (a) −2.4 V (HOMO) and 1.9 V (LUMO); (b) −2.5 V (HOMO) and 1.3 V (LUMO). The current was set to 50 pA in all cases. The HOMO and LUMO shifts of, respectively, 0.15 V and 0.5 V are marked. Insets: Maps of $\mathrm{d}I/\mathrm{d}V$ recorded with 50 pA and −2 V (HOMO), 0.7 V (LUMO). The maps have a size of 3 nm × 2.3 nm.

changes, which is partially compensated for the HOMO due to electron transfer from DBP to h-BN-Ru(0001). This interpretation is in agreement with studies of 7,7′,8,8′-tetracyanoquinodimethane (TCNQ) on graphene-covered Ru(0001) [216], where charge transfer between TCNQ and the surface was only present at the strongly bonded valley regions of the graphene moiré lattice, while it was absent at top regions.

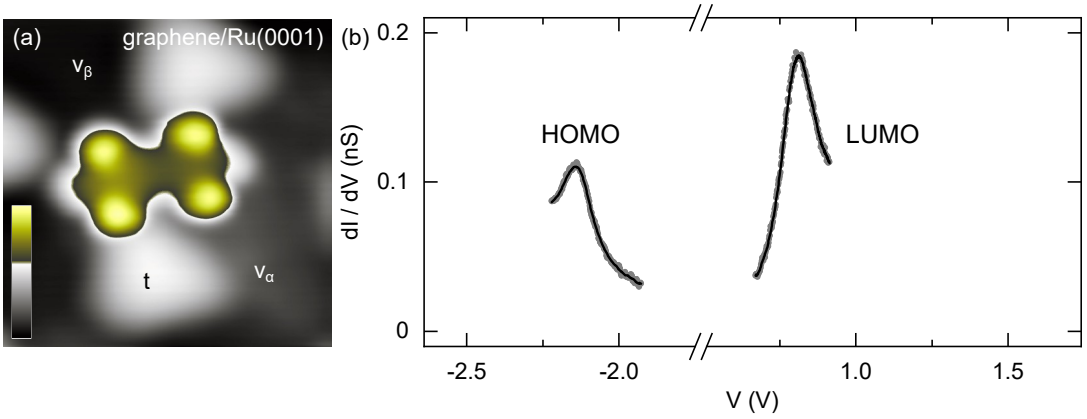

Figure 5.7: (a) STM image of DBP adsorbed on Ru(0001) covered with graphene (-1 V, 60 pA, 5 nm $\times$ 5 nm). The color scale ranges from 0 pm (black) to 253 pm (yellow). Moiré sites with high (low) contrast are indicated with t (v_α, v_β). (b) $\mathrm{d}I/\mathrm{d}V$ spectra of HOMO and LUMO of DBP adsorbed on graphene-covered Ru(0001) (feedback loop parameters: -2.68 V, 50 pA (HOMO); 1.47 V, 50 pA (LUMO); modulation: 5 $\mathrm{mV_{rms}}$, 754 Hz).

The different LUMO energies of DBP at wire (≈ 1.2 V) and pore (≈ 0.7 V) therefore also explain the topographic difference of the molecule at a bias voltage of 0.7 V (Figure 5.5(a)). At this bias voltage, DBP at wire sites lies well within the HOMO–LUMO gap and the STM data is not representing the topographic structure of HOMO or LUMO. In contrast, the chosen bias voltage matches the LUMO peak for DBP at pore sites and gives rise to the spatial resolution of the LUMO structure across the molecule. At elevated bias voltages of ≈ 1.2 V, both molecules exhibit the submolecular contrast of the LUMO as the required energy is reached for DBP adsorbed in the pore as well as on the wire (Figure 5.5(b)).

Comparing the properties of the DBP molecule on graphene-covered Ru(0001) with the one on h-BN covered Ru(0001), some differences, which will be discussed next, emerge. Graphene on Ru(0001) exhibits a pronounced moiré pattern with protrusions (t) and depressions (v_α, v_β), reflecting different graphene–Ru stacking regions [88, 90], as explained in Chapter 3.2. DBP prefers adsorption at the valley regions of the moiré lattice marked with v_α and v_β in Figure 5.7(a). A prefered adsorption in valley regions was previously reported for low coverages of FePc adsorbed on graphene-covered Ru(0001) [217].

Spectra of $\mathrm{d}I/\mathrm{d}V$ reveal an average energy of ≈ -2.05 eV (≈ 0.75 eV) for

the HOMO (LUMO) , which corresponds to a HOMO-LUMO gap of $\approx 2.8\,\mathrm{eV}$. As the DBP molecules did not adsorb on on-top (t) sites of the graphene moiré, no shift in molecular orbital energies was found between valley and on top sites. However, small variations ($\approx 0.1\,\mathrm{eV}$) due to different adsorption geometries in the valley regions of the moiré lattice were present. After the main spectroscopic characteristics of DBP adsorbed on all four substrate systems have been discussed, the main differences will be summarized and compared in the following.

Comparison

Table 5.1 summarizes the experimental observations for HOMO and LUMO energies, ε^H and ε^L, the resulting HOMO–LUMO gap width defined as $\Delta = \varepsilon^L - \varepsilon^H$ as well as the HOMO and LUMO resonance widths, δ^H and δ^L, for the different surfaces. Only molecules adsorbed on wire sites of the h-BN-covered Ru(0001) surface are considered in the comparison. The molecular orbital energies are virtually rigid shifted. The energies of HOMO and LUMO of DBP on h-BN are increased by $\approx 0.80\,\mathrm{eV}$ upon changing from Ru(0001) to Pt(111). In the case of adsorption on graphene these shifts are $\approx 0.86\,\mathrm{eV}$ and $\approx 0.98\,\mathrm{eV}$, respectively. As discussed above, spectroscopy was performed on isolated molecules only, therefore the shift is not due to different molecular environments [201]. Moreover, in view of the magnitude of the shift a change of the molecular energies in different electric fields between the tip and the sample [202, 203] is unlikely, too. Therefore, these shifts are compared with work function differences of the surfaces since HOMO and LUMO energies are similarly affected, which is likely due to their alignment with the vacuum level owing to the weak molecule–substrate interaction and comparable to the previous discussed change in molecular orbital energy depending on the different adsorption sites on h-BN.

Work functions reported for h-BN on Ru(0001) and Pt(111) are $4.0 \pm 0.1\,\mathrm{eV}$ [72] and $4.9\,\mathrm{eV}$ [77], respectively. The resulting work function difference of $0.9 \pm 0.1\,\mathrm{eV}$ is in good agreement with the observed molecular orbital energy shift for DBP on the different h-BN-covered surfaces. For DBP on graphene the situation is not as clear, which is due to ambiguous reports on the work function of graphene on Ru(0001) and Pt(111). Work functions of $4.5\,\mathrm{eV}$ [218] and $3.9\,\mathrm{eV}$ [84] have been reported for graphene-covered Ru(0001). For graphene on Pt(111) values for the work function of $\approx 5.6\,\mathrm{eV}$ [219] and $\approx 5.2\,\mathrm{eV}$ [220] have been

	ε^H (eV)	ε^L (eV)	Δ (eV)	δ^H (meV)	δ^L (meV)
h-BN/Ru	-1.82 ± 0.01	1.15 ± 0.01	2.97 ± 0.02	42 ± 3	46 ± 2
graphene/Ru	-2.06 ± 0.08	0.75 ± 0.04	2.81 ± 0.12	102 ± 10	112 ± 4
h-BN/Pt	-1.02 ± 0.04	1.95 ± 0.06	2.97 ± 0.10	39 ± 2	55 ± 2
graphene/Pt	-1.20 ± 0.04	1.73 ± 0.04	2.93 ± 0.08	62 ± 7	118 ± 10

Table 5.1: Summary of spectral characteristics of DBP on the investigated surfaces. Averaged HOMO and LUMO energies, ε^H and ε^L, define the gap width Δ between these orbitals. Orbital resonance widths (δ^H, δ^L) denote the full widths at half maximum of Lorentzian line shapes that were fit to the spectral signatures of HOMO and LUMO.

recorded. Therefore, the HOMO and LUMO energy shifts observed from the same two-dimensional material on the different metal surfaces are comparable with work function differences of the surfaces, which, however, vary between $\approx 0.7\,\text{eV}$ and $\approx 1.7\,\text{eV}$. Additionally, the energy of the molecular orbitals is compared for DBP on h-BN and graphene on the same metal surface, where the same rationale as discussed above should be applicable. Comparing the energies of HOMO and LUMO in Table 5.1 shows that for both Ru(0001) and Pt(111) HOMO and LUMO energies shift to lower values upon changing from h-BN to graphene, while the aforementioned work functions have smaller values on h-BN than on graphene. For Ru(0001) the work function is reduced by 0.1 eV – 0.5 eV on h-BN in comparison to the graphene-covered surface. The same trend is found for Pt(111), where the work function on the h-BN-covered surface is smaller by 0.3 eV – 0.7 eV. At first sight this downward shift of energies is not compatible with the presented observations for the molecular orbitals of DBP on the different substrate systems. However, local work function variations, *i. e.*, the change in work function with the actual adsorption site of DBP, have to be considered as well. As discussed above for h-BN-covered Ru(0001) and Pt(111), the local work function decreases by more than 0.4 eV from *w* to *p* sites of the moiré pattern; that is, for molecules adsorbed at *p* regions HOMO and LUMO energies are reduced by more than 0.4 eV in comparison to molecules at *w* sites. Moreover, site-specific work function variations are likewise present on the moiré lattice of graphene [217, 221] and vary on the order of 0.1 eV. Considering these local work function variations as well shows that the observed molecular orbital

energy shifts are compatible with the surface work function changes.

The HOMO–LUMO gap width varies weakly between $\approx 2.8\,\mathrm{eV}$ and $\approx 3.0\,\mathrm{eV}$ because of the essentially rigid shift of the frontier orbital energies on all discussed substrate systems. This gap width is comparable with the value reported for DBP on graphene-covered Ir(111) [12] and lower than for DBP on NaCl-covered Ag(111) [185]. The true gap width that reflects the difference in ionization potential and electron affinity and, thus, considers final-state Coulomb effects is expected to be even larger. Adsorption of a molecule on a surface tends to reduce this gap width due to the polarization of the environment and to the interaction with the molecular image charge [43].

After discussing the energy position of the molecular orbitals upon adsorption on the two-dimensional materials, the spectroscopic linewidth of the orbital signatures is examined. Values of the full width at half maximum (FWHM) are extracted from Lorentzian fits to the molecular orbital resonances. The full widths at half maximum of the molecular orbital resonances are strikingly different for DBP on h-BN and graphene. The HOMO and LUMO spectral line widths are considerably smaller on h-BN than on graphene independent of the metal substrate. In the case of the DBP LUMO on Ru(0001) the linewidth is up to 2 times smaller. The width of the orbital resonance is important for the observation of the Franck-Condon spectroscopic fine structure, which will be discussed in the next section. The strongly different molecular orbital line widths on h-BN and graphene may be related to the electronic structure of the two-dimensional materials on the metal surfaces. A combined experimental and theoretical comparison of h-BN and graphene on Ru(0001) [84] showed that h-BN exhibits dielectric behavior while graphene acts like a metal. As a consequence, the absence of a Fermi surface for h-BN on Ru(0001) [84] guarantees the low molecule–metal hybridization and the resulting sharp molecular orbital resonances. In contrast, the electronic coupling of DBP on graphene to the metal substrate is still present, which represents the effective transport of the injected charge to the substrate, reduces its residence time at the molecule and consequently broadens the molecular orbital resonances. For Pt(111), it is less straightforward to explain the differences in spectral line widths since both h-BN and graphene are considered physisorbed on Pt(111). Indeed, the mixing of Pt d, s-states with h-BN and graphene π-bands is weak [69, 222]. However, recent

photoemission results for graphene on Pt(111) [223] and a comparison of band dispersions in an akin system, h-BN and graphene on Ir(111) [224], lends support to the idea that h-BN on Pt(111) does not exhibit a Fermi surface while graphene does. Therefore, a less effective decay channel for charge carriers injected into DBP on h-BN-covered Pt(111) may tentatively rationalize the sharper molecular orbital resonances than observed from graphene-covered Pt(111).

5.1.4 Conclusions

The decoupling behavior of h-BN and graphene on Pt(111) and Ru(0001) is evaluated by single-molecule $\mathrm{d}I/\mathrm{d}V$ spectroscopy. The experimental data unravel that molecular frontier orbitals are a probe for local variations of the h-BN buffer function, as well as for the work function difference between the different metallic substrate systems. Weakly coupled molecules exhibit a rigid shift of their orbital resonances, which reflects site-dependent work function changes of h-BN. More strongly coupled molecules give rise to additional charge transfer processes that cause the nonuniform alteration of molecular energy levels. Moreover, different linewidth reveal different decoupling characteristics comparing h-BN and graphene on the same metal substrates. The presented results offer an alternative to judge the extent of decoupling due to an intermediate buffer layer.

5.2 Vibrational Properties of an Organic Molecule on Two-Dimensional Materials

As discussed in the previous section, hexagonal boron nitride (h-BN) and graphene are emerging as monatomically thin decoupling layers. While structural aspects of adsorption on h-BN-covered [68] and graphene-covered [225] surfaces have been studied in detail, vibrational spectroscopy at the single-molecule level is scarce. Scanning tunneling spectroscopy (STS) of vibronic levels of 1,3,5-tris(2,2-dicyanovinyl)benzene adsorbed on graphene on h-BN-covered SiO_2 [13], Co-phthalocyanine (Co-Pc) molecules on graphene-covered SiO_2–Si samples [11] as well as on h-BN-covered Ir(111) [158], of conjugated oligophenylenes on h-BN-covered Cu(111) [14] and Mn-Pc on h-BN-covered Rh(111) [15]. In these studies molecular orbitals – the highest occupied MO (HOMO) or the lowest unoccupied MO (LUMO) – appear with a spectroscopic fine structure in differential conductance ($\mathrm{d}I/\mathrm{d}V$, I: tunneling current, V: bias voltage) data, which is assigned to vibronic progression with a single vibrational quantum energy.

The aforementioned spectroscopic results convey the apparently similar behavior of h-BN and graphene as a two-dimensional buffer layer. This emerging picture, however, is surprising since h-BN and graphene have vastly different electronic properties, *e. g.*, h-BN exhibits a direct band gap exceeding 6 eV [226] while graphene is a semimetal [20, 227]. The discrepancy between expectations and available experimental data motivated the low-temperature scanning tunneling microscope (STM) studies presented here, which systematically explore the buffer layer efficiency of h-BN and graphene on different metal surfaces.

5.2.1 Experimental Methods

The experimental procedure and the growth of h-BN and graphene is explained in Chapter 2.4 and 3.1 in detail. DBP molecules were deposited at a low temperature of $\approx 10\,\mathrm{K}$ by directing a molecular beam to the sample mounted in the STM through openings of the cryostat radiation shields. The molecules were sublimated from a Mo crucible heated by an electron beam.

5.2.2 Spectroscopic Results

Hexagonal boron nitride and graphene was epitaxially grown on Ru(0001) and Pt(111), *i. e.*, on metal substrates that exhibit strong (Ru) and weak (Pt) hybridization with h-BN [68] and graphene [90], as discussed previously. For subsequently deposited DBP molecules vibronic progression is observed for both frontier orbitals, HOMO and LUMO, albeit to considerably different extent on h-BN and graphene. On the h-BN-covered surfaces, all orbital and progression resonances exhibit sharp spectral line shapes. In addition, two distinct vibrational energies are extracted from the progression series seen in the Franck-Condon spectra. Moreover, progression of the vibronic levels themselves is observed. In contrast, molecular orbitals and vibronic excitations exhibit broader spectral signatures on the graphene-covered surfaces, a single quantum energy defines the spacing of progression resonances, and progression of vibronic levels is absent.

Ru(0001)

Figure 5.8(a) shows an STM image of h-BN on Ru(0001). The regular periodic pattern is due to a moiré effect of the lattice-mismatched h-BN and Ru(0001), which partitions the surface into pore (p) and wire (w) regions, as described in Chapter 3.1 and is also in agreement with previous reports [72, 228–230]. As discussed in Chapter 5.1, the p and w sites of the moiré lattice have been identified as preferred adsorption sites for DBP [231]. In this section, however, only isolated DBP molecules adsorbed to w domains are considered in the analysis since they stably occupy this adsorption site, insensitive to the injected tunneling current ranging from 10 pA to 100 pA. The submolecular motifs caused by HOMO (left inset to Figure 5.8(a)) and LUMO (right) are seen in STM images recorded at bias voltages falling into the spectral ranges of the HOMO and LUMO peaks in $\mathrm{d}I/\mathrm{d}V$ spectroscopy, labeled H_{00} and L_{00}, respectively, in Figure 5.8(b). Their spatial distribution and energy position is described in the previous section and is in agreement with previous reported studies of DBP on various surfaces [12, 185, 231].

In addition to the sharp molecular orbital resonances H_{00} and L_{00} characterized in Chapter 5.1, spectra of $\mathrm{d}I/\mathrm{d}V$ (Figure 5.8(b)) reveal a rich fine structure for both HOMO ($V < 0\,\mathrm{V}$) and LUMO ($V > 0\,\mathrm{V}$) signatures. The HOMO

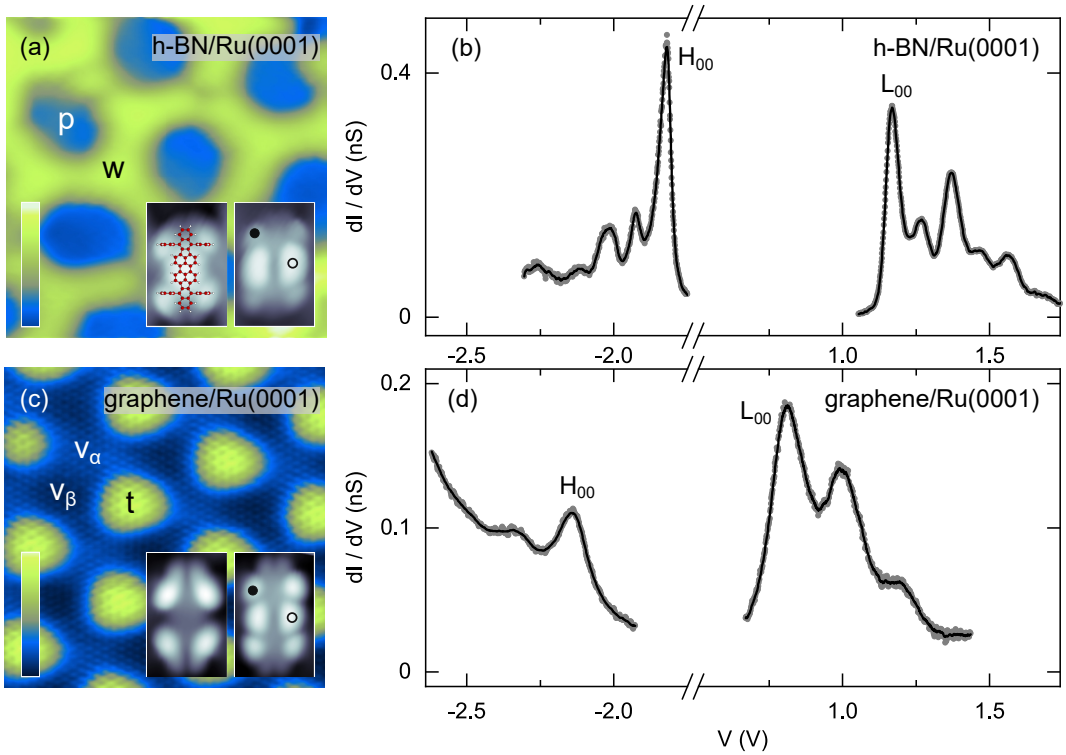

Figure 5.8: STM and STS data for DBP adsorbed on h-BN and graphene on Ru(0001) acquired at 5 K. (a) STM image of a single h-BN sheet on Ru(0001) (bias voltage: −0.47 V, tunneling current: 100 pA, size: 10 nm × 10 nm). The moiré pattern appears as a periodic array of pore (p) and wire (w) regions. The color scale ranges from 0 pm (dark blue) to 243 pm (light yellow). Inset: STM images of a single DBP on h-BN/Ru(0001) acquired with −1.90 V (left) and 1.20 V (right) (50 pA, 2.2 nm × 3.4 nm). The superimposed ball-and-stick model of DBP in the left inset is to scale. (b) $\mathrm{d}I/\mathrm{d}V$ spectra (dots) of DBP HOMO (H_{00}) and LUMO (L_{00}) spectral regions on h-BN-covered Ru(0001) (feedback loop parameters: −2.30 V, 50 pA (HOMO); 1.92 V, 50 pA (LUMO); modulation: 5 $\mathrm{mV_{rms}}$, 754 Hz). The solid lines represent smoothed data. The individual spectra were recorded atop the molecular sites marked as a dot (•, HOMO) and a circle (∘, LUMO) in the right inset to (a). (c) Atomically resolved STM image of graphene on Ru(0001) (1.27 V, 50 pA, 10 nm × 10 nm). The moiré superlattice is visible as protrusions (t) and depressions (v_α, v_β). The color scale ranges from 0 pm (dark blue) to 124 pm (light yellow). Inset: STM images of a single DBP on graphene-covered Ru(0001) acquired with −2.50 V (left) and 1.00 V (right) (50 pA, 2.2 nm × 3.4 nm). (d) Like (b), for DBP on graphene-covered Ru(0001) (feedback loop parameters: −2.68 V, 50 pA (HOMO); 1.47 V, 50 pA (LUMO); modulation: 5 $\mathrm{mV_{rms}}$, 754 Hz).

spectroscopic feature was best observed in spectroscopy atop the phenyl groups, while the LUMO is spatialy located at the side of the central molecular backbone [12, 231]. Figure 5.8(b) presents spectroscopic data that are composed of two individual spectra. The additional satellite peaks to H_{00} and L_{00} are nearly equidistantly spaced, which makes vibronic progression likely to be at the origin of these sidebands, which will be discussed later. Spectra obtained for DBP adsorbed on p sites reveal a similar spectroscopic fine structure due to vibronic progression, albeit rigidly shifted with respect to w site spectra due to local work function variations and charge transfer processes, as discussed in Chapter 5.1.

Importantly, the alternating heights of adjacent sideband peaks are not compatible with the expected Franck-Condon behavior [47, 48] and a uniform Huang-Rhys factor [232]. In the case of one vibrational mode with a single Huang-Rhys factor a monotonously decreasing peak intensity of the sideband peaks would be expected (see also Chapter 2.8). This discrepancy will be resolved below by allowing two groups of molecular vibrations with distinct energies and Huang-Rhys factors to participate in the vibronic progression.

In comparison to the results obtained on hBN-covered Ru(0001), a different structure of vibronic sidebands emerges on the graphene-covered surface. DBP prefers adsorption to the valley regions of the moiré lattice labeled as v_α and v_β. The $\mathrm{d}I/\mathrm{d}V$ spectra of HOMO and LUMO (Figure 5.8(d)) differ strongly from their counterparts obtained on h-BN (Figure 5.8(b)). The increased width of orbital and sideband resonances is most striking. In addition, the spectroscopic fine structure is not as pronounced as observed on h-BN. Only a reduced number of satellite peaks are visible. However, the mutual peak separations hint at vibronic progression with only a single vibrational quantum energy.

Pt(111)

In addition to the results obtained for DBP adsorbed on h-BN and graphene on Ru(0001), the same experiments were carried out on Pt(111), which will be discussed and compared next.

Figure 5.9 summarizes the results obtained for h-BN and graphene on Pt(111). In Figure 5.9(a) an STM image shows the h-BN mesh with its clearly visible honeycomb unit cell, as discussed previously. The insets to Figure 5.9(a) present STM images of DBP on h-BN-covered Pt(111) acquired with bias voltages in the

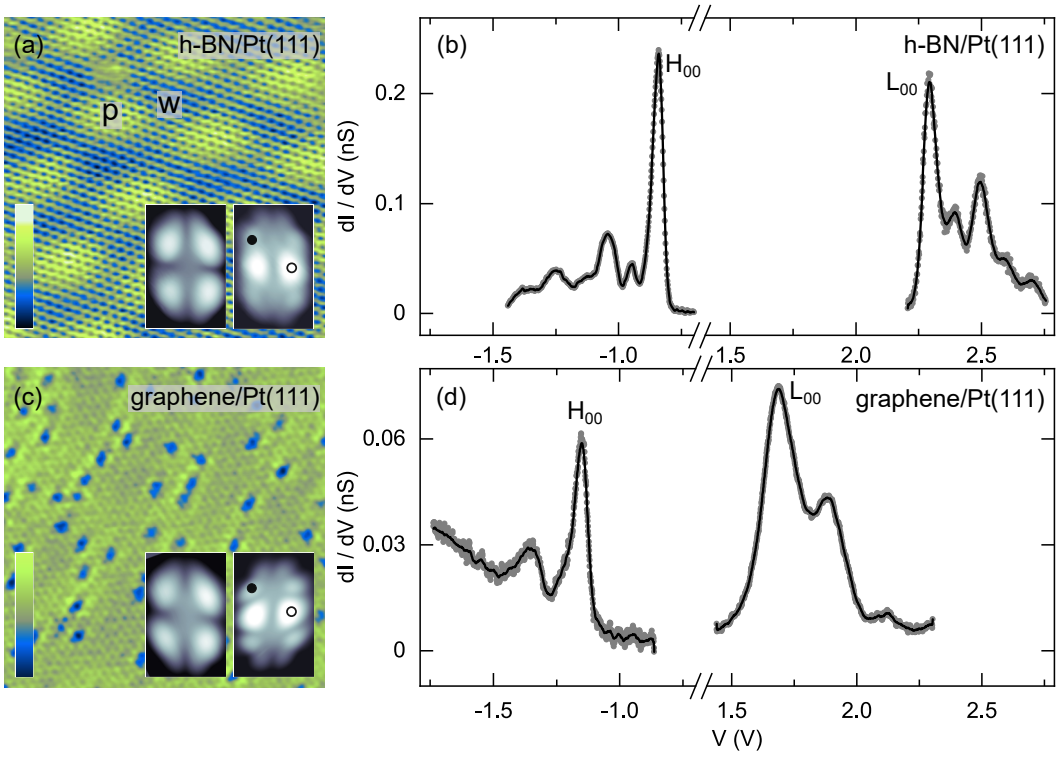

Figure 5.9: STM and STS data for DBP adsorbed on h-BN and graphene on Pt(111) acquired at 5 K. (a) STM image of a single h-BN sheet on Pt(111) (0.01 V, 400 nA, 10 nm × 10 nm). The honeycomb unit cell of the mesh is visible together with the moiré pattern partitioning the surface into pore (p) and wire (w) regions. The color scale ranges from 0 pm (black) to 105 pm (white). Inset: STM images of a single DBP on h-BN-covered Pt(111) acquired with −0.95 V (left) and 2.10 V (right) (50 pA, 2.2 nm × 3.4 nm). (b) dI/dV spectra (dots) of DBP HOMO (H_{00}) and LUMO (L_{00}) spectral regions on h-BN-covered Pt(111) (feedback loop parameters: −1.44 V, 50 pA (HOMO); 2.78 V, 50 pA (LUMO); modulation: 5 $\mathrm{mV_{rms}}$, 754 Hz). The solid lines represent smoothed data. The individual spectra were acquired atop the molecular sites indicated by a dot (•, HOMO) and a circle (∘, LUMO) in the right inset to (a). (c) STM image of graphene on Pt(111) (0.01 V, 100 nA, 10 nm × 10 nm). The color scale ranges from 0 pm (dark blue) to 55 pm (yellow). Inset: STM images of a single DBP on graphene-covered Pt(111) acquired with −1.90 V (left) and 2.10 V (right) (50 pA, 2.2 nm × 3.4 nm). (d) Like (b), for DBP on graphene-covered Pt(111) (feedback loop parameters: −1.80 V, 20 pA (HOMO); 2.30 V, 20 pA (LUMO); modulation: 5 $\mathrm{mV_{rms}}$, 754 Hz).

range of the HOMO (left) and LUMO (right) peaks in dI/dV spectra, referred to as, respectively, H_{00} and L_{00} in Figure 5.9(b). The submolecular motifs are

similar to those observed from DBP on h-BN and graphene on Ru(0001) (Figure 5.8(a,c)). Figure 5.9(b) shows a $\mathrm{d}I/\mathrm{d}V$ spectrum that is composed of two individual spectra, one obtained atop the phenyl group ($V < 0\,\mathrm{V}$) and the other recorded atop one side of the central backbone ($V > 0\,\mathrm{V}$). The satellite peaks to H_{00} and L_{00} are due to vibronic progression, as will be scrutinized below. Again, similar to h-BN on Ru(0001), molecular vibrational modes with two distinct quantum energies will be demonstrated to cause the Franck-Condon spectra.

Graphene on Pt(111) (Figure 5.9(c)) exhibits irregularly distributed depressions that are most likely due to Pt(111) lattice vacancies [82] or C impurities embedded in the Pt(111) surface [83]. For graphene on Pt(111) the HOMO and LUMO spatial distributions of DBP (insets to Figure 5.9(c)) are akin to the data obtained for the molecule on h-BN-covered Pt(111).

Despite the weak graphene–Pt(111) coupling the spectroscopic data of DBP on graphene-covered Pt(111) deviate clearly from the findings observed for DBP adsorbed on the h-BN-covered surface. The reduced number of satellite peaks to both the HOMO and LUMO signatures, which are assigned to vibronic progression resonance, too, is most obvious. The second-order progression is virtually absent from the HOMO and very weak for the LUMO. Moreover, the mutual distance of resonances evidences the presence of only a single vibrational energy, rather than two as observed for h-BN.

5.2.3 Vibrational Progression

Next, the spectroscopic sidebands to H_{00} and L_{00} are explained. As mentioned above, the observed nearly equidistant separation of the resonances hints at the mechanism of vibronic progression being operative. First, the HOMO and LUMO spectroscopic fine structure of DBP on h-BN-covered Ru(0001) (Figure 5.10(a)) will be explained within the Franck-Condon picture [47, 48].

Figure 5.10(b) schematically shows the excitation of vibrations in the Franck-Condon model for the case of electron attachment to the LUMO. The tunneling electron excites the neutral molecule M^0 to the singly negative charged molecular state M^-. It therefore transiently charges the molecule during the tunneling process. As DBP is adsorbed on the decoupling h-BN layer, the attached electron exhibits an extended residence time at the molecule, which further enables

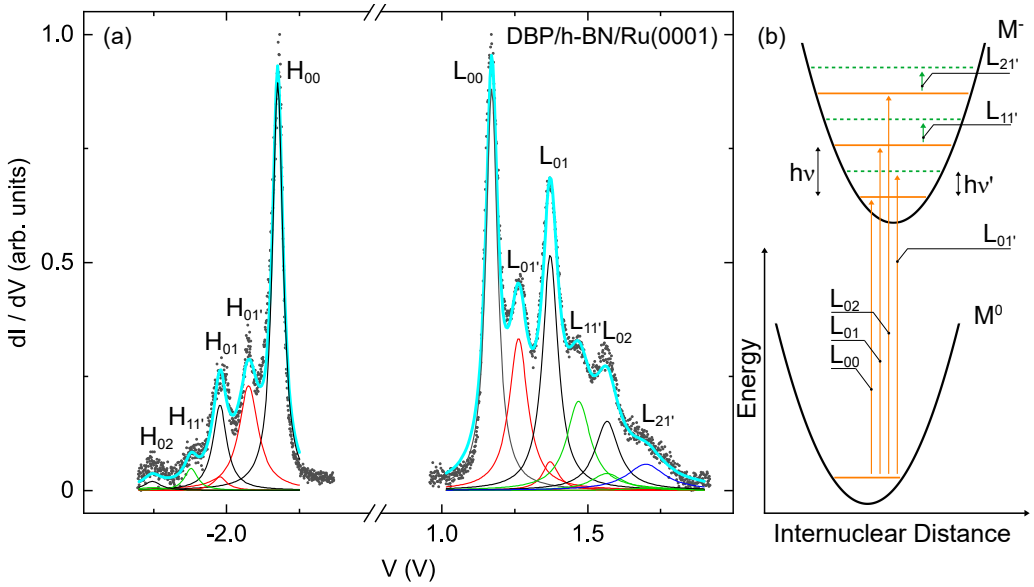

Figure 5.10: Description of STS data using vibronic progression in the Franck-Condon picture. (a) $\mathrm{d}I/\mathrm{d}V$ data (dots) of Figure 5.8b after considering an exponential background and normalizing peak heights of H_{00} and L_{00} to unity. The thick solid line is a fit to the data using a superposition of Lorentzians (thin lines), which is discussed in detail in the text. (b) Illustration of vibronic progression (L_{01}, L_{02}, $L_{01'}$) and progression of vibronic levels ($L_{11'}$, $L_{21'}$) of the LUMO in the Franck-Condon picture. M^0 and M^- denote the molecule in its, respectively, neutral and transient negative charge state. Vertical arrows mark transitions and are horizontally offset for clarity. Index n in L_{nm} denotes the initial state for the vibronic transition, the vibrational ground state of M^0 ($n = 0$) or the first ($n = 1$) and second ($n = 2$) vibrationally excited state of M^- with energy $\mathrm{h}\nu$; index m marks the final state where primed quantum numbers indicate the vibrational excitation of M^- with energy $\mathrm{h}\nu'$.

an efficient coupling to the molecular vibrations in the transient charge state. Therefore, M^- may be in its vibrational ground state or in a vibrationally excited state. In the former case, the transition is labeled L_{00}, while in the latter case, the transition reads L_{0m}, with m denoting the quantum number of vibrational excitations with energies $\mathrm{h}\nu$ ($m = 1, 2$) or $\mathrm{h}\nu'$ ($m = 1', 2'$). The peak heights of the vibronic resonances resulting from transitions of the vibrational ground state of M^0 to the kth vibrationally excited state of M^- obey a Poisson distribution

$$\iota_{\alpha k} = \exp(-S_\alpha)\frac{S_\alpha^k}{k!} \tag{5.1}$$

where $\alpha \in \{\nu, \nu'\}$ denotes the frequency of the involved molecular vibration and integer $k \geq 0$ the vibrational quantum number. The Huang-Rhys factor S_α may be extracted from the normalized spectroscopic data by comparing the heights of the first-order vibronic sideband peak ($\iota_{\alpha 1}$) and the molecular orbital spectroscopic signature (I_0),

$$S_\alpha = \frac{\iota_{\alpha 1}}{I_0}. \tag{5.2}$$

Normalized data were obtained by setting the peak height of the main electronic transitions H_{00} and L_{00} to unity and by consideration of an exponential background, which is explained in Appendix D.

By comparing the peak intensity of adjacent vibronic sidebands of DBP on the h-BN-covered surfaces (Figure 5.8(b), Figure 5.9(b), Figure 5.10(a)), it is evident that the distribution of peak heights deviates from a Poisson distribution with a uniform Huang-Rhys factor according to equation 5.1. Therefore, the observed Franck-Condon spectrum is assumed to be the result of two sets of vibrational modes with distinct frequencies $\nu \neq \nu'$, each with its own Huang-Rhys factor, S_ν and $S_{\nu'}$. The evaluation of mutual peak distances within the LUMO spectral line shape results in one group of vibrational quanta exhibiting energies around $\mathrm{h}\nu = 199 \pm 3\,\mathrm{meV}$. The second group of molecular vibrational modes has energies around $\mathrm{h}\nu' = 99 \pm 3\,\mathrm{meV}$, found by a linear fit of the respective vibronic sideband spectroscopic signatures.

The peak intensities for transition $L_{01'}$ can be analyzed using equation 5.2 and normalized $\mathrm{d}I/\mathrm{d}V$ data (Figure 5.10(a)), the Huang-Rhys factor of this group reads as $S_{\nu'} \approx 0.32$ (Table 5.2). The transition $L_{02'}$ at $\varepsilon^L + 2 \cdot \mathrm{h}\nu'$ nearly coincides with transition L_{01} at $\varepsilon^L + 1 \cdot \mathrm{h}\nu$ due to $\nu' \approx \nu/2$. The finite peak height of $L_{02'}$ must therefore be considered, as described below, in order to extract the Huang-Rhys factor of the group of vibrational modes with frequency ν, which reads $S_\nu \approx 0.57$.

Due to the small value of $S_{\nu'}$ the peak heights of transitions $L_{0m'}$ with $m' > 2$ do not contribute to the Franck-Condon spectrum significantly. The intensity of the transition $L_{03'}$ with $S_{\nu'} \approx 0.32$ will already be less than 1% of the initial transition L_{00}. Surprisingly, sidebands are yet observed at $\varepsilon^L + 3 \cdot \mathrm{h}\nu'$ ($L_{11'}$) and $\varepsilon^L + 5 \cdot \mathrm{h}\nu'$ ($L_{21'}$). These sidebands are rationalized in terms of the progression of vibronic levels at $\varepsilon^L + 1 \cdot \mathrm{h}\nu$ and $\varepsilon^L + 2 \cdot \mathrm{h}\nu$, induced by vibrational quanta

with energy $\mathrm{h}\nu'$. This effect is often referred to as progression of vibronic progression and was previously reported for C_{60} [233], metalloporphyrins [234] and naphthalocyanine molecules [235].

The spectroscopic data will now be described by a model consisting of the superposition of Lorentzian line shapes, in order to further corborate the idea of observed vibrational sidebands. In particular, two sets of vibrational modes with distinct frequencies $\nu \neq \nu'$ will be included in the description.

The superposition of Lorentzians reads

$$\Lambda(V) = \sum_{i=1}^{N} a_i \lambda_i (V - V_i) + \sum_{k=1}^{N'} b_k \lambda_k (V - V_k) \tag{5.3}$$

where N (N') denotes the maximum order of vibronic progression due to vibrations with frequency ν (ν') visible in the $\mathrm{d}I/\mathrm{d}V$ spectra. The individual Lorentzian line shapes are

$$\lambda_{i,k}(V - V_{i,k}) = \frac{1}{\pi} \cdot \frac{\gamma_{i,k}}{(V - V_{i,k})^2 + \gamma_{i,k}^2} \tag{5.4}$$

that are peaked at $V_{i,k} = \varepsilon_{i,k}/\mathrm{e}$ with $\varepsilon_i = \varepsilon^L + i \cdot \mathrm{h}\nu$ and $\varepsilon_k = \varepsilon^L + k \cdot \mathrm{h}\nu'$; $\gamma_{i,k}$ denotes the half width at half maximum.

In order to corroborate the idea that vibronic progression is operative, the Lorentzian peak heights, $a_i/(\pi\gamma_i)$ and $b_k/(\pi\gamma_k)$, are expected to obey the Poisson distribution of equation 5.1 with distinct Huang-Rhys factors S_ν and $S_{\nu'}$. Therefore, Huang-Rhys factors S_ν and $S_{\nu'}$ have to be extracted from the experimental data. To this end, the Huang-Rhys factor $S_{\nu'}$ for the progression series with smaller energy $\mathrm{h}\nu'$ was determined from transition $L_{01'}$ using equation 5.2. With $S_{\nu'}$ at hand, the progression series due to modes with energies $\approx \mathrm{h}\nu'$, namely $L_{01'}$, $L_{02'}$, ..., was calculated. In particular, the peak height for transition L_{01} at energy $\varepsilon^L + 1 \cdot \mathrm{h}\nu$ was corrected by subtraction of the peak height for transition $L_{02'}$ at $\varepsilon^L + 2 \cdot \mathrm{h}\nu' \approx \varepsilon^L + 1 \cdot \mathrm{h}\nu$, as the peak intensity consists of the sum of the individual peak intensities of the transition L_{02} and $L_{02'}$. The Huang-Rhys factor for the progression series due to modes with energies $\approx \mathrm{h}\nu$ therefore reads $S_\nu = (\iota_{01} - \iota_{02'})/I_0$. However, the model does not yet describe the observed vibrational sidebands in total.

The progression of vibronic levels was taken into account in the model by calculating the progression series of the levels at $\varepsilon^L + 1 \cdot \mathrm{h}\nu$ and $\varepsilon^L + 2 \cdot \mathrm{h}\nu$ caused by vibrational modes with energies $\approx \mathrm{h}\nu'$. To this end a superposition of Lorentzians at $\varepsilon^L + 1 \cdot \mathrm{h}\nu + k \cdot \mathrm{h}\nu'$ and $\varepsilon^L + 2 \cdot \mathrm{h}\nu + k \cdot \mathrm{h}\nu'$ ($k \geq 1$) was added to the fit function. The peak heights of the Lorentzians were calculated by equation 5.1 using $S_{\nu'}$ as the relevant Huang-Rhys factor.

Indeed, including Lorentzian resonances in the fit at $\varepsilon^L + 1 \cdot \mathrm{h}\nu + m \cdot \mathrm{h}\nu'$, $\varepsilon^L + 2 \cdot \mathrm{h}\nu + m \cdot \mathrm{h}\nu'$ with peak heights evolving according to equation 5.1 with Huang-Rhys factor $S_{\nu'}$ leads to a good description of the experimental data (Figure 5.10(a)). A similar fit procedure was used for the HOMO-related vibronic progression (Figure 5.10(a), $V < 0\,\mathrm{V}$). Within the uncertainty margins the same groups of vibrational modes, $\mathrm{h}\nu = 201 \pm 5\,\mathrm{meV}$ and $\mathrm{h}\nu' = 97 \pm 5\,\mathrm{meV}$, cause the vibronic progression (H_{01}, H_{02}, $H_{01'}$) and progression of vibronic levels ($H_{11'}$).

The analysis of the satellite resonances of DBP on h-BN-covered Pt(111) (Figure 5.11(a)) has been performed analogously, revealing a similar progression of vibronic progression. Consequently, vibrational energies were extracted by linear fit to the spectroscopic resonances, resulting in energies of $\mathrm{h}\nu = 207 \pm 8\,\mathrm{meV}$ and $\mathrm{h}\nu' = 102 \pm 4\,\mathrm{meV}$ for the HOMO, $\mathrm{h}\nu = 196 \pm 6\,\mathrm{meV}$ and $\mathrm{h}\nu' = 98 \pm 3\,\mathrm{meV}$ for the LUMO. The Huang-Rhys factors for the respective vibrational quanta was found to be $S_{\nu'} \approx 0.32$ and $S_{\nu} \approx 0.52$ for the LUMO and $S_{\nu'} \approx 0.18$ and $S_{\nu} \approx 0.2$ for the HOMO.

In the case of the graphene-covered surfaces (Figure 5.11(b,c)) only one vibrational mode is observed in the vibronic peak series. Therefore, the model is reduced to only one set of Lorentzian peaks for the transitions L_{01}, L_{02}, ... with a distinct Huang-Rhys factor S_{ν}. For DBP adsorbed on graphene-covered Pt(111) (Figure 5.11(b)) vibronic progression of the DBP HOMO and LUMO with quantum energies of $207 \pm 5\,\mathrm{meV}$ and $210 \pm 7\,\mathrm{meV}$ were extracted, respectively. The corresponding Huang-Rhys factors are $S_{\nu} \approx 0.25$ for the HOMO and $S_{\nu} \approx 0.51$ for the LUMO.

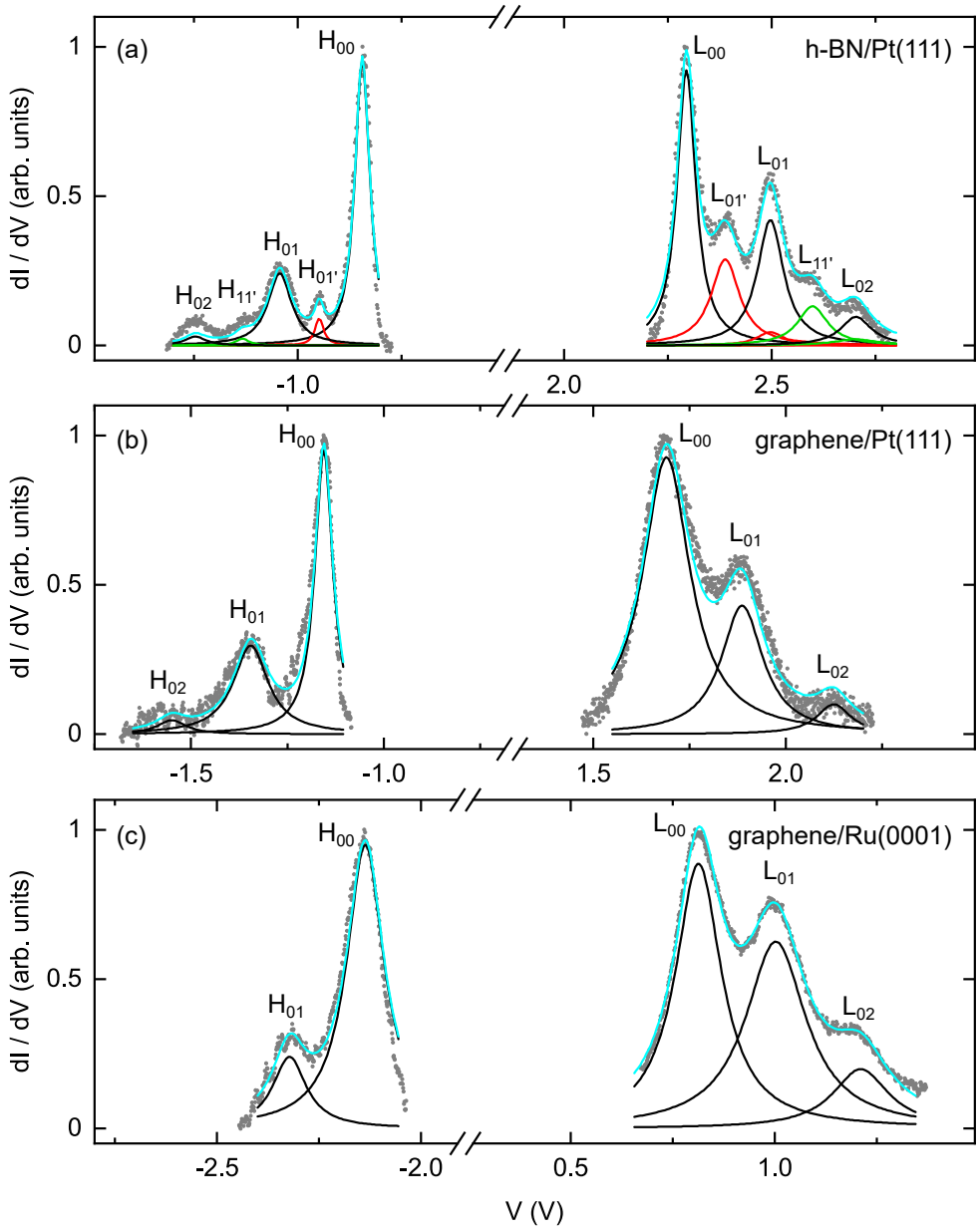

Figure 5.11: $\mathrm{d}I/\mathrm{d}V$ spectra (dots) of DBP after consideration of an exponential background together with the Franck-Condon fit (thick solid line). Thin solid lines depict individual Lorentzian line shapes used for the fit. (a) Vibronic spectra for HOMO ($V < 0\,\mathrm{V}$) and LUMO ($V > 0\,\mathrm{V}$) of DBP on h-bN-covered Pt(111). (b) Like (a) for graphene-covered Pt(111). (c) Like (a) for graphene-covered Ru(0001).

	S_{ν}^{H}	S_{ν}^{L}	$S_{\nu'}^{H}$	$S_{\nu'}^{L}$
h-BN/Ru	0.21 ± 0.03	0.57 ± 0.03	0.21 ± 0.02	0.32 ± 0.01
graphene/Ru	0.24 ± 0.05	0.72 ± 0.04	—	—
h-BN/Pt	0.20 ± 0.03	0.52 ± 0.04	0.18 ± 0.03	0.32 ± 0.04
graphene/Pt	0.25 ± 0.02	0.51 ± 0.04	—	—

Table 5.2: Collection of Huang-Rhys factors $S_{\nu,\nu'}^{H,L}$ for the vibronic progression of DBP HOMO (H) and LUMO (L) induced by molecular vibrations with frequencies ν, ν' on the different surfaces.

Similarly, on graphene-covered Ru(0001) (Figure 5.11(c)) the vibrational energies are found as 175 ± 20 meV for the HOMO and 198 ± 7 meV for the LUMO, with Huang-Rhys factors for the HOMO (LUMO) of $S_\nu \approx 0.24$ ($S_\nu \approx 0.72$).

Within the uncertainty margins the vibrational modes causing the vibronic progression are the same for the two frontier orbitals on the different substrate systems. The vibrational modes with energy ≈ 100 meV are compatible with out-of-plane C–H bending modes of the phenyl groups and the dibenzoperiflanthene backbone as well as in-plane C ring angular deformations of the backbone, while vibrations with energy ≈ 200 meV can be ascribed to C–C stretching modes of the phenyl groups and the backbone as well as in-plane C–H bending modes of the backbone [199]. In principle, different modes could be responsible for the progression in different orbitals. The matching of symmetries between vibrational and electronic states was demonstrated to be favorable for the occurrence of vibronic progression [12].

5.2.4 Conclusions

In conclusion, two prominent two-dimensional materials, h-BN and graphene, that are emerging as equally well suited buffer layers for adsorbed molecules exhibit clearly different decoupling behavior, irrespective of the metal substrate they hybridize with. While the dielectric nature of h-BN favors the observation of sharp orbital resonances, the metallic character of graphene impedes a similarly effective decoupling. Moreover, molecular orbitals lying well inside the band gap of the dielectric two-dimensional material are expected to exhibit pronounced vibronic progression. Materials with wide band gaps, such as h-BN, are therefore

evidenced as the most appropriate buffer layers for future experiments that strive for exploring the extent to which genuine gas-phase molecular properties can be preserved after adsorption on a substrate surface.

CHAPTER 6

Conclusions and Prospects

The first part of this dissertation explores and characterizes the growth and structure of graphene and hexagonal boron nitride (h-BN) on two metal substrates Pt(111) and Ru(0001). The different strength of interaction results in weakly and strongly corrugated surfaces on Pt(111) and Ru(0001), respectively. Here, an efficient growth method for the growth of h-BN using borazane as a precursor molecule was developed as an *in situ* preparation method, which is applicable in different UHV applications in the future.

Successively, a method for the fabrication of heterostructures of graphene and h-BN by the sequential growth on an intermediate Pt layer is developed on the Pt(111) surface. The successful intercalation of Pt beneath h-BN as well as the presence of graphene on the surface indicates the suitability of this preparation technique. Additional to a moiré resulting from the interaction of h-BN and Pt(111), an additional hexagonal structure emerges on the heterostructure by lowering the tip-sample distance. At the time of writing this thesis different reconstructions of residual Pt atoms were considered to explain those observed structures. In the transition regions of the heterostructure to monolayer graphene, phonon signals have been observed, which most likely originate from out-of-plane h-BN phonons at the K-point of the Brillouin zone and subsequently couple to the top graphene layer.

This preparation technique was also used previously for the growth of bilayer graphene on Pt(111) [116] and is also sufficient for stacking of h-BN and

graphene. Therefore, other combinations of two-dimensional materials can be explored using the same technique as a blueprint in future experiments.

The grown two-dimensional materials are now used to evaluate the decoupling behavior of h-BN and graphene on Pt(111) and Ru(0001) by single-molecule $\mathrm{d}I/\mathrm{d}V$ spectroscopy. The experimental data unravel that molecular frontier orbitals are a probe for local variations of the h-BN buffer function, as well as for the work function difference between the different metallic substrate systems. Weakly coupled molecules exhibit a rigid shift of orbital resonances, which reflects site-dependent work function changes of h-BN. More strongly coupled molecules give rise to additional charge transfer processes that cause the nonuniform alteration of molecular energy levels. The presented results offer an alternative to judge the extent of decoupling due to an intermediate buffer layer as well as a probe of local work function variations on sample surfaces.

Graphene and h-BN used as buffer layers for adsorbed molecules exhibit clearly different decoupling behaviors, irrespective of the metal substrate they hybridize with. Different linewidth reveal different decoupling characteristics comparing h-BN and graphene on the same metal substrates. While the dielectric nature of h-BN favors the observation of sharp orbital, resonances the metallic character of graphene impedes a similarly effective decoupling. Moreover, molecular orbitals lying well inside the band gap of the dielectric two-dimensional material are expected to exhibit pronounced vibronic progression. Materials with wide band gaps, such as h-BN, are therefore evidenced as the most appropriate buffer layers for future experiments that strive for exploring the extent to which genuine gas-phase molecular properties can be preserved after adsorption on a substrate surface.

Those surprisingly different decoupling characteristics judged by the comparison of graphene and h-BN could be explored further by including other buffer layers like transition metal dichalcogenides in future studies. Recently, MoS_2 has been used as an efficient decoupling layer for molecules giving rise to high-resolution molecular spectra [17, 18]. An extended comparison could give further insights into the requirements of buffer layers used as decoupling layers for adsorbed molecules.

Appendix

A Pt Orientation on the Pt(111) Surface

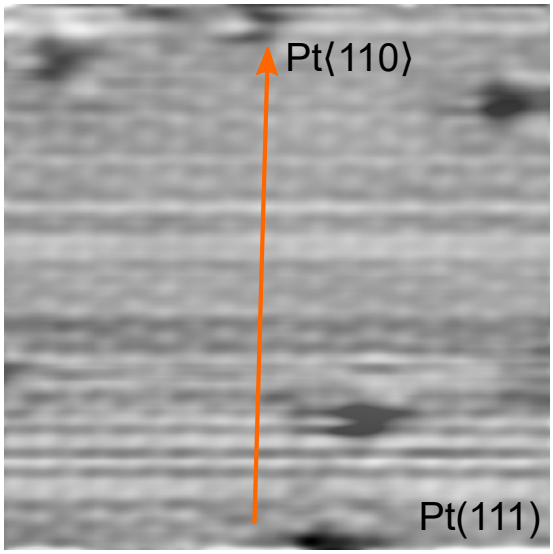

Figure A: STM image of Pt(111) with atomic resolution acquired at 80 K (10 mV, 300 nA, 5 nm × 5 nm). The Pt⟨110⟩ direction is indicated with an orange arrow.

STM image of the Pt(111) substrate with atomic resolution acquired at 80 K in order to identify the Pt⟨110⟩ direction. Because of a remaining possible drift due to thermal contraction, the Pt⟨110⟩ direction is only used as a estimate and can vary by about $\pm(5-10)^\circ$.

B Reference Spectra of 2D-Materials

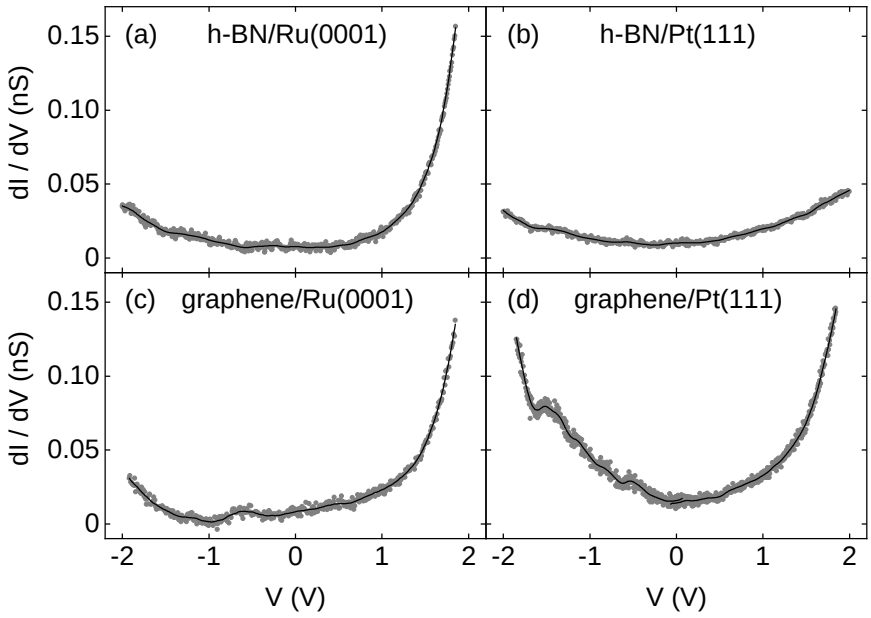

Figure B: Spectra of $\mathrm{d}I/\mathrm{d}V$ acquired atop (a) h-BN on Ru(0001) (1.92 V, 50 pA), (b) h-BN on Pt(111) (2.40 V, 50 pA), (c) graphene on Ru(0001) (1.92 V, 100 pA), (d) graphene on Pt(111) (−1.92 V, 100 pA for the spectral region covering occupied states; 1.92 V, 100 pA for the spectral region covering unoccupied states). The bias voltage modulation was 5 $\mathrm{mV_{rms}}$, 754 Hz in all cases.

Reference spectra of $\mathrm{d}I/\mathrm{d}V$ acquired atop clean h-BN and graphene on the different metal surfaces are presented in Figure B. They show that in the bias voltage range relevant to the spectroscopy of vibronic progression the substrate electronic structure is essentially featureless. In the experiments, spectroscopy of the clean two-dimensional materials was perpetually performed to ensure a constant status of the probe.

C dI/dV Maps of DBP on h-BN-covered Pt(111)

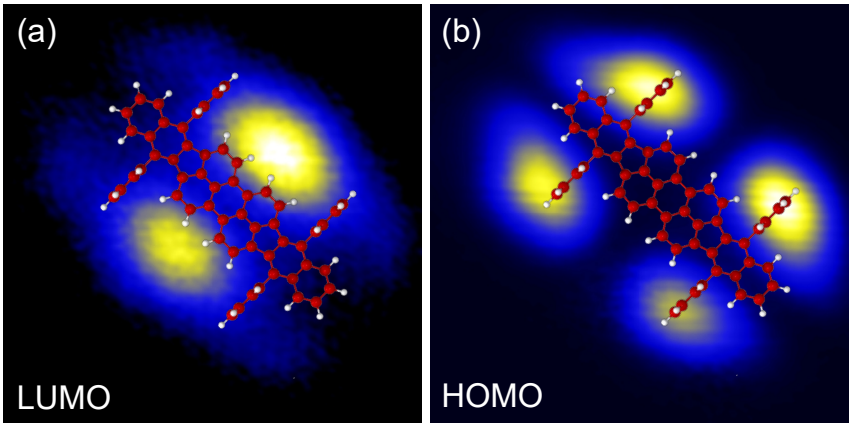

Figure C: dI/dV maps of a single DBP molecule adsorbed on h-BN-covered Pt(111) recorded in constant height mode. The feedback loop was opened placing the tip on a molecular site with a high spectroscopic signal to ensure a sufficient tip-sample distance. (a) Spatial distribution of the LUMO ($V = 2.1\,\mathrm{V}$, $3\,\mathrm{nm} \times 3\,\mathrm{nm}$, $V_{mod,rms} = 20\,\mathrm{mV}, f = 754\,\mathrm{Hz}$). (b) Spatial distribution of the HOMO ($V = -0.9\,\mathrm{V}$, $3\,\mathrm{nm} \times 3\,\mathrm{nm}$, $V_{mod,rms} = 20\,\mathrm{mV}, f = 754\,\mathrm{Hz}$).

dI/dV maps of a single DBP molecule adsorbed on h-BN-covered Pt(111) recorded in constant height mode reveal the spatial distribution of the molecular frontier orbitals of DBP. The HOMO is spatially localized at the four phenyl groups of the DBP molecule, while the LUMO is located at the side of the molecular backbone.

D Consideration of an Exponential Background

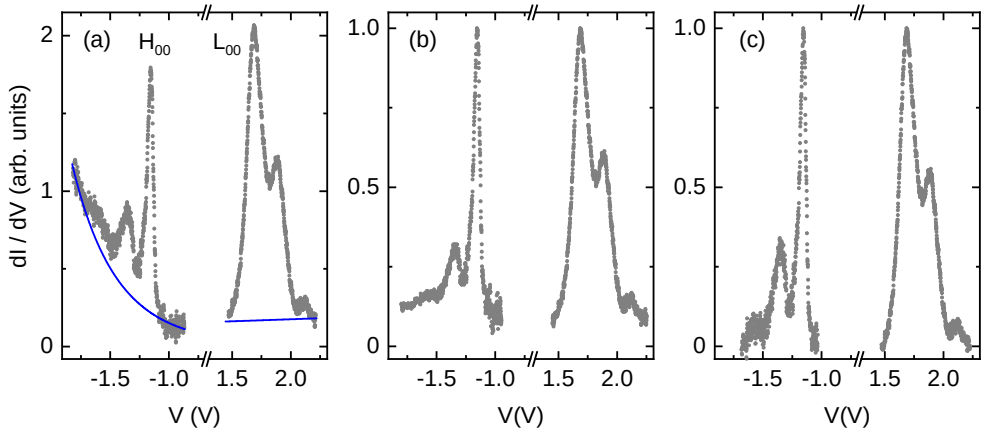

Figure D: (a) Raw $\mathrm{d}I/\mathrm{d}V$ spectra (dots) showing the occupied ($V < 0\,\mathrm{V}$) and unoccupied ($V > 0\,\mathrm{V}$) states of DBP adsorbed on graphene-covered Pt(111) together with an exponential background (solid line) according to eq 1 (feedback loop parameters: $-1.80\,\mathrm{V}$, $20\,\mathrm{pA}$ ($V < 0\,\mathrm{V}$); $2.30\,\mathrm{V}$, $20\,\mathrm{pA}$ ($V > 0\,\mathrm{V}$)). The two individual spectra were acquired atop a phenyl group ($V < 0\,\mathrm{V}$) and the side of the central backbone ($V > 0\,\mathrm{V}$). HOMO and LUMO are denoted H_{00} and L_{00}, respectively. (b) Spectra of (a) divided by the exponential background. (c) Spectra of (a) after subtraction of the exponential background.

In order to obtain reliable information on peak positions, widths and heights, the Franck-Condon description of $\mathrm{d}I/\mathrm{d}V$ spectra presented in the main text requires the consideration of the transmission factor of the tunneling barrier. Assuming a one-dimensional tunneling barrier with trapezoidal shape and barrier height $\bar{\Phi} = (\Phi_\mathrm{t} + \Phi_\mathrm{s})/2$ ($\Phi_\mathrm{t,s}$: work functions of tip and sample) [236, 237] the background in $\mathrm{d}I/\mathrm{d}V$ spectra is expected to follow the transmission factor of the tunneling barrier, *i. e.*, takes the form

$$\beta(V) = \beta_0 \cdot \exp\left(\beta_1 \cdot \sqrt{\bar{\Phi} + \mathrm{e}V}\right) \tag{1}$$

with fit parameters β_0, β_1 and the elementary charge e. This background was fit to spectroscopic data for sufficiently large $|V|$, *i. e.*, outside the bias voltage interval where orbital and vibronic resonances are present. The average work function was set to $\bar{\Phi} = 4\,\mathrm{eV}$. Exemplarily, the exponential background function is depicted for the HOMO and LUMO spectral region of DBP on graphene-

covered Pt(111) in Figure D(a).

In a next step, raw $\mathrm{d}I/\mathrm{d}V$ data were divided by $\beta(V)$, individually for $V < 0\,\mathrm{V}$ and $V > 0\,\mathrm{V}$, according to a density-of-states convolution technique previously reported [238]. Figure D(b) shows these normalized data. In many spectra the exponential variation of the background was very weak (Figure D(b), $V > 0\,\mathrm{V}$). Dividing such spectra by $\beta(V)$ (Figure D(b)) or subtracting $\beta(V)$ (Figure D(c)) from raw $\mathrm{d}I/\mathrm{d}V$ yielded comparable data sets. While in the case of division a nearly constant nonzero baseline has to be considered in the subsequent fit of Lorentzian line shapes to the data, subtraction yields a baseline of zero. The data depicted in Figure D(b,c) were additionally normalized, where the peak heights of H_{00} and L_{00} were set to unity. Importantly, Huang-Rhys factors extracted from differently treated raw data varied within the uncertainty margins given in Table 5.2.

List of Figures

List of Tables

Abbreviations

CVD	chemical vapor deposition
DOS	density of states
DBP	dibenzotetraphenylperiflanthene
DFT	density functional theory
fcc	face centered cubic
FWHM	full width at half maximum
h-BN	hexagonal boron nitride
hcp	hexagonal close-packed
HOMO	highest occupied molecular orbital
IETS	inelastic electron tunneling spectroscopy
LA	acoustic longitudinal phonon mode
LUMO	lowest unoccupied molecular orbital
MESD	minaturized energy storage devices
OLED	organic light emitting diode
STM	scanning tunneling microscope
STS	scanning tunneling spectroscopy
UHV	ultra high vacuum
ZA	acoustic out-of-plane phonon mode

List of Peer-Reviewed Publications

- Mehler, A.; Néel, N. and Kröger, J.
  Dissimilar Decoupling Behavior of Two-Dimensional Materials on Metal Surfaces
  The Journal of Physical Chemistry Letters, 2020, **11**, 5204-5211

- Rothe, K.; Mehler, A.; Néel, N. and Kröger, J.
  Scanning tunneling microscopy and spectroscopy of rubrene on clean and graphene-covered metal surfaces
  Beilstein Journal of Nanotechnology, 2020, **11**, 1157-1167

- Mehler, A.; Néel, N. and Kröger, J.
  Probing site-dependent decoupling of hexagonal boron nitride with molecular frontier orbitals
  Journal of Vacuum Science & Technology A, 2019, **37**, 061404

- Halle, J.; Mehler, A.; Néel, N.and Kröger, J.
  Preparation of graphene bilayers on platinum by sequential chemical vapour deposition
  Phys. Chem. Chem. Phys., 2019, **21**, 3140-3144

- Mehler, A.; Néel, N.; Bocquet, M.-L. and Kröger, J.
  Exciting vibrons in both frontier orbitals of a single hydrocarbon molecule on graphene
  Journal of Physics: Condensed Matter, 2018, **31**, 065001

- Mehler, A.; Kirchhuebel, T.; Néel, N.; Sojka, F.; Forker, R.; Fritz, T. and Kröger, J.
  Ordered Superstructures of a Molecular Electron Donor on Au(111)
  Langmuir, 2017, **33**, 6978-6984

Bibliography

[1] G. Binnig, H. Rohrer, C. Gerber, and E. Weibel. Surface Studies by Scanning Tunneling Microscopy. *Physical Review Letters*, 49(1):57–61, 1982.

[2] V. Madhavan, W. Chen, T. Jamneala, M. Crommie, and N. Wingreen. Tunneling into a Single Magnetic Atom: Spectroscopic Evidence of the Kondo Resonance. *Science*, 280(5363):567–569, 1998.

[3] S. Nadj-Perge, I. K. Drozdov, J. Li, H. Chen, S. Jeon, J. Seo, A. H. MacDonald, B. A. Bernevig, and A. Yazdani. Observation of Majorana fermions in ferromagnetic atomic chains on a superconductor. *Science*, 346(6209): 602–607, 2014.

[4] M.-X. Wang, C. Liu, J.-P. Xu, F. Yang, L. Miao, M.-Y. Yao, C. L. Gao, C. Shen, X. Ma, X. Chen, Z.-A. Xu, Y. Liu, S.-C. Zhang, D. Qian, J.-F. Jia, and Q.-K. Xue. The Coexistence of Superconductivity and Topological Order in the Bi_2Se_3 Thin Films. *Science*, 336(6077):52–55, 2012.

[5] X. H. Qiu, G. V. Nazin, and W. Ho. Vibrationally Resolved Fluorescence Excited with Submolecular Precision. *Science*, 299(5606):542–546, 2003.

[6] W. H. B. C. Stipe, M. A. Rezaei. Single-Molecule Vibrational Spectroscopy and Microscopy. *Science*, 280:1732–1735, 1998.

[7] S. Zhang. Review of Modern Field Effect Transistor Technologies for Scaling. *Journal of Physics: Conference Series*, 1617:012054, 2020.

[8] Y. Li, J.-Y. Liu, Y.-D. Zhao, and Y.-C. Cao. Recent advancements of high efficient donor–acceptor type blue small molecule applied for OLEDs. *Materials Today*, 20:258–266, 2017.

[9] S.-J. Zou, Y. Shen, F.-M. Xie, J.-D. Chen, Y.-Q. Li, and J.-X. Tang. Recent advances in organic light-emitting diodes: toward smart lighting and displays. *Materials Chemistry Frontiers*, 4:788–820.

[10] S. Y. An, T. B. Schon, B. T. McAllister, and D. S. Seferos. Design strategies for organic carbonyl materials for energy storage: Small molecules, oligomers, polymers and supramolecular structures. *EcoMat*, 2(4):12055, 2020.

[11] S. Bouvron, R. Maurand, A. Graf, P. Erler, L. Gragnaniello, M. Skripnik, D. Wiedmann, C. Engesser, C. Nef, W. Fu, C. Schönenberger, F. Pauly, and M. Fonin. Charge transport in a single molecule transistor probed by scanning tunneling microscopy. *Nanoscale*, 10:1487–1493, 2018.

[12] A. Mehler, N. Néel, M.-L. Bocquet, and J. Kröger. Exciting vibrons in both frontier orbitals of a single hydrocarbon molecule on graphene. *Journal of Physics: Condensed Matter*, 31(6):065001, 2018.

[13] A. Riss, S. Wickenburg, L. Z. Tan, H.-Z. Tsai, Y. Kim, J. Lu, A. J. Bradley, M. M. Ugeda, K. L. Meaker, K. Watanabe, T. Taniguchi, A. Zettl, F. R. Fischer, S. G. Louie, and M. F. Crommie. Imaging and Tuning Molecular Levels at the Surface of a Gated Graphene Device. *ACS Nano*, 8(6):5395–5401, 2014.

[14] C.-A. Palma, S. Joshi, T. Hoh, D. Ecija, J. V. Barth, and W. Auwärter. Two-Level Spatial Modulation of Vibronic Conductance in Conjugated Oligophenylenes on Boron Nitride. *Nano Letters*, 15(4):2242–2248, 2015.

[15] L. Liu, T. Dienel, R. Widmer, and O. Gröning. Interplay between Energy-Level Position and Charging Effect of Manganese Phthalocyanines on an Atomically Thin Insulator. *ACS Nano*, 9(10):10125–10132, 2015.

[16] X. H. Qiu, G. V. Nazin, and W. Ho. Vibronic States in Single Molecule Electron Transport. *Phys. Rev. Lett.*, 92:206102, 2004.

[17] N. Krane, C. Lotze, G. Reecht, L. Zhang, A. L. Briseno, and K. J. Franke. High-Resolution Vibronic Spectra of Molecules on Molybdenum Disulfide Allow for Rotamer Identification. *ACS Nano*, 12(11):11698–11703, 2018.

[18] G. Reecht, N. Krane, C. Lotze, L. Zhang, A. L. Briseno, and K. J. Franke. Vibrational Excitation Mechanism in Tunneling Spectroscopy beyond the Franck-Condon Model. *Physical Review Letters*, 124(11), 2020.

[19] K. S. Novoselov, A. K. Geim, S. V. Morozov, D. Jiang, Y. Zhang, S. V. Dubonos, I. V. Grigorieva, and A. A. Firsov. Electric Field Effect in Atomically Thin Carbon Films. *Science*, 306(5696):666–669, 2004.

[20] K. S. Novoselov, A. K. Geim, S. V. Morozov, D. Jiang, M. I. Katsnelson, I. V. Grigorieva, S. V. Dubonos, and A. A. Firsov. Two-dimensional gas of massless Dirac fermions in graphene. *Nature*, 438:197 – 200, 2005.

[21] K. S. Novoselov, V. I. Falko, L. Colombo, P. R. Gellert, M. G. Schwab, and K. Kim. A roadmap for graphene. *Nature*, 490:192–200, 2012.

[22] L. H. Li and Y. Chen. Atomically Thin Boron Nitride: Unique Properties and Applications. *Advanced Functional Materials*, 26(16):2594–2608, 2016.

[23] K. Watanabe, T. Taniguchi, and H. Kanda. Direct-bandgap properties and evidence for ultraviolet lasing of hexagonal boron nitride single crystal. *Nature*, 3:404–409, 2004.

[24] G. Cassabois, P. Valvin, and B. Gil. Hexagonal boron nitride is an indirect bandgap semiconductor. *Nature Photonics*, 10:262–266, 2016.

[25] S.-K. Kim, H. Cho, M. J. Kim, H.-J. Lee, J. hyung Park, Y.-B. Lee, H. C. Kim, C. W. Yoon, S. W. Nam, and S. O. Kang. Efficient catalytic conversion of ammonia borane to borazine and its use for hexagonal boron nitride (white graphene). *Journal of Materials Chemistry A*, 1:1976–1981.

[26] L. Britnell, R. V. Gorbachev, R. Jalil, B. D. Belle, F. Schedin, A. Mishchenko, T. Georgiou, M. I. Katsnelson, L. Eaves, S. V. Morozov, N. M. R. Peres, J. Leist, A. K. Geim, K. S. Novoselov, and L. A. Ponomarenko. Field-Effect Tunneling Transistor Based on Vertical Graphene Heterostructures. *Science*, 335(6071):947–950, 2012.

[27] S. I. AL-Saedi, A. J. Haider, A. N. Naje, and N. Bassil. Improvement of Li-ion batteries energy storage by graphene additive. *Energy Reports*, 6: 64–71, 2020.

[28] I. H. Son, J. H. Park, S. Park, K. Park, S. Han, J. Shin, S.-G. Doo, Y. Hwang, H. Chang, and J. W. Choi. Graphene balls for lithium rechargeable batteries with fast charging and high volumetric energy densities. *Nature Communications*, 8(1):1561, 2017.

[29] M. A. Hassan, A. Sen, T. Zaman, and M. Mostari. Emergence of graphene as a promising anode material for rechargeable batteries: a review. *Materials Today Chemistry*, 11:225–243, 2019.

[30] H. Liu, G. Zhang, X. Zheng, F. Chen, and H. Duan. Emerging miniaturized energy storage devices for microsystem applications: from design to

integration. *International Journal of Extreme Manufacturing*, 2(4):042001, 2020.

[31] A. Nimbalkar and H. Kim. Opportunities and Challenges in Twisted Bilayer Graphene: A Review. *Nano-Micro Letters*, 12(1):126, 2020.

[32] M. Yankowitz, Q. Ma, P. Jarillo-Herrero, and B. J. LeRoy. van der Waals heterostructures combining graphene and hexagonal boron nitride. *Nature Reviews Physics*, 1(2):112–125, 2019.

[33] B. Voigtländer. *Scanning Probe Microscopy*. Springer Berlin Heidelberg, 2015.

[34] J. Bardeen. Tunnelling from a Many-Particle Point of View. *Physical Review Letters*, 6(2):57–59, 1961.

[35] M. Passoni, F. Donati, A. Li Bassi, C. S. Casari, and C. E. Bottani. Recovery of local density of states using scanning tunneling spectroscopy. *Phys. Rev. B*, 79:045404, 2009.

[36] C. J. Chen. Theory of scanning tunneling spectroscopy. *Journal of Vacuum Science & Technology A: Vacuum, Surfaces, and Films*, 6(2):319–322, 1988.

[37] J. Tersoff and D. R. Hamann. Theory and Application for the Scanning Tunneling Microscope. *Phys. Rev. Lett.*, 50(25):1998–2001, 1983.

[38] J. Tersoff and D. R. Hamann. Theory of the scanning tunneling microscope. *Phys. Rev. B*, 31:805–813, 1985.

[39] A. Gustafsson, N. Okabayashi, A. Peronio, F. J. Giessibl, and M. Paulsson. Analysis of STM images with pure and CO-functionalized tips: A first-principles and experimental study. *Phys. Rev. B*, 96:085415, 2017.

[40] J. Kröger, L. Limot, H. Jensen, R. Berndt, S. Crampin, and E. Pehlke. Surface state electron dynamics of clean and adsorbate-covered metal surfaces studied with the scanning tunnelling microscope. *Progress in Surface Science*, 80(1):26 – 48, 2005.

[41] A. T. N'Diaye, J. Coraux, T. N. Plasa, C. Busse, and T. Michely. Structure of epitaxial graphene on Ir(111). *New J. Phys.*, 10(4):043033, 2008.

[42] J. Halle. *Intercalation of Graphene: Inelastic Excitations, Bilayer Growth, and Superstructures*. PhD thesis, TU Ilmenau, 2019.

[43] I. F. Torrente, K. J. Franke, and J. I. Pascual. Spectroscopy of C_{60} single molecules: the role of screening on energy level alignment. *Journal of Physics: Condensed Matter*, 20(18):184001, 2008.

[44] N. Krane. *Investigation and Utilization of Molybdenum Disulfide as Decoupling Layer on Au(111)*. PhD thesis, Freie Universität Berlin, 2019.

[45] L. Bartels, G. Meyer, K.-H. Rieder, D. Velic, E. Knoesel, A. Hotzel, M. Wolf, and G. Ertl. Dynamics of Electron-Induced Manipulation of Individual CO Molecules on Cu(111). *Physical Review Letters*, 80(9):2004–2007, 1998.

[46] S. Joshi, F. Bischoff, R. Koitz, D. Ecija, K. Seufert, A. P. Seitsonen, J. Hutter, K. Diller, J. I. Urgel, H. Sachdev, J. V. Barth, and W. Auwärter. Control of Molecular Organization and Energy Level Alignment by an Electronically Nanopatterned Boron Nitride Template. *ACS Nano*, 8(1):430–442, 2014.

[47] J. Franck and E. G. Dymond. Elementary processes of photochemical reactions. *Transactions of the Faraday Society*, 21(February):536, 1926.

[48] E. Condon. A Theory of Intensity Distribution in Band Systems. *Phys. Rev.*, 28:1182–1201, 1926.

[49] P. W. Atkins and J. de Paula. *Physikalische Chemie*. Wiley-VCH GmbH, 2013. ISBN 3527332472.

[50] J. W. Gadzuk. Inelastic resonance scattering, tunneling, and desorption. *Phys. Rev. B*, 44:13466–13477, 1991.

[51] N. S. Wingreen, K. W. Jacobsen, and J. W. Wilkins. Inelastic scattering in resonant tunneling. *Phys. Rev. B*, 40:11834–11850, 1989.

[52] N. S. Wingreen, K. W. Jacobsen, and J. W. Wilkins. Resonant Tunneling with Electron-Phonon Interaction: An Exactly Solvable Model. *Phys. Rev. Lett.*, 61:1396–1399, 1988.

[53] Z. Lin, A. Mcnamara, Y. Liu, K. sik Moon, and C.-P. Wong. Exfoliated hexagonal boron nitride-based polymer nanocomposite with enhanced thermal conductivity for electronic encapsulation. *Composites Science and Technology*, 90:123–128, 2014.

[54] C. Berger, Z. Song, T. Li, X. Li, A. Y. Ogbazghi, R. Feng, Z. Dai, A. N. Marchenkov, E. H. Conrad, P. N. First, and W. A. de Heer. Ultrathin Epitaxial Graphite: 2D Electron Gas Properties and a Route toward Graphene-based Nanoelectronics. *The Journal of Physical Chemistry B*, 108(52):19912–19916, 2004.

[55] F. H. Farwick zum Hagen, D. M. Zimmermann, C. C. Silva, C. Schlueter, N. Atodiresei, W. Jolie, A. J. Martínez-Galera, D. Dombrowski, U. A. Schröder, M. Will, P. Lazić, V. Caciuc, S. Blügel, T.-L. Lee, T. Michely, and C. Busse. Structure and Growth of Hexagonal Boron Nitride on Ir(111). *ACS Nano*, 10(12):11012–11026, 2016.

[56] A. T. N'Diaye, M. Engler, C. Busse, D. Wall, N. Buckanie, F.-J. M. zu Heringdorf, R. van Gastel, B. Poelsema, and T. Michely. Growth of graphene on Ir(111). *New Journal of Physics*, 11(2):023006, 2009.

[57] K. K. Kim, S. M. Kim, and Y. H. Lee. A new horizon for hexagonal boron nitride film. *Journal of the Korean Physical Society*, 64(10):1605–1616, 2014.

[58] S. Lizzit and A. Baraldi. High-resolution fast X-ray photoelectron spectroscopy study of ethylene interaction with Ir(111): From chemisorption to dissociation and graphene formation. *Catalysis Today*, 154(1-2):68–74, 2010.

[59] M. Paffett, R. Simonson, P. Papin, and R. Paine. Borazine adsorption and decomposition at Pt(111) and Ru(001) surfaces. *Surface Science*, 232(3): 286–296, 1990.

[60] A. Nagashima, N. Tejima, Y. Gamou, T. Kawai, and C. Oshima. Electronic states of monolayer hexagonal boron nitride formed on the metal surfaces. *Surface Science*, 357-358:307–311, 1996.

[61] M. Corso, W. Auwärter, M. Muntwiler, A. Tamai, T. Greber, and J. Osterwalder. Boron Nitride Nanomesh. *Science*, 303(5655):217–220, 2004.

[62] W. Auwärter, T. Kreutz, T. Greber, and J. Osterwalder. XPD and STM investigation of hexagonal boron nitride on Ni(111). *Surface Science*, 429 (1-3):229–236, 1999.

[63] M. A. Wahab, H. Zhao, and X. D. Yao. Nano-confined ammonia borane for chemical hydrogen storage. *Frontiers of Chemical Science and Engineering*, 6(1):27–33, 2012.

[64] Y. J. Choi, Y. Xu, W. J. Shaw, and E. C. E. Rönnebro. Hydrogen Storage Properties of New Hydrogen-Rich BH_3NH_3-Metal Hydride (TiH_2, ZrH_2, MgH_2, and/or CaH_2) Composite Systems. *The Journal of Physical Chemistry C*, 116(15):8349–8358, 2012.

[65] F. H. Stephens, V. Pons, and R. T. Baker. Ammonia–borane: the hydrogen source par excellence? *Dalton Trans.*, 25(25):2613–2626, 2007.

[66] S. Frueh, R. Kellett, C. Mallery, T. Molter, W. S. Willis, C. King'ondu, and S. L. Suib. Pyrolytic Decomposition of Ammonia Borane to Boron Nitride. *Inorganic Chemistry*, 50(3):783–792, 2011.

[67] F. Baitalow, J. Baumann, G. Wolf, K. Jaenicke-Rößler, and G. Leitner. Thermal decomposition of B–N–H compounds investigated by using combined thermoanalytical methods. *Thermochimica Acta*, 391(1-2):159–168, 2002.

[68] W. Auwärter. Hexagonal boron nitride monolayers on metal supports: Versatile templates for atoms, molecules and nanostructures. *Surface Science Reports*, 74(1):1 – 95, 2019.

[69] A. B. Preobrajenski, A. S. Vinogradov, M. L. Ng, E. Ćavar, R. Westerström, A. Mikkelsen, E. Lundgren, and N. Mårtensson. Influence of chemical interaction at the lattice-mismatched $h-$BN/Rh(111) and $h-$BN/Pt(111) interfaces on the overlayer morphology. *Phys. Rev. B*, 75: 245412, 2007.

[70] R. Laskowski and P. Blaha. Ab initio study of $h-$BN nanomeshes on Ru(001), Rh(111), and Pt(111). *Phys. Rev. B*, 81:075418, 2010.

[71] M. Paffett, R. Simonson, P. Papin, and R. Paine. Borazine adsorption and decomposition at Pt(111) and Ru(001) surfaces. *Surface Science*, 232(3): 286 – 296, 1990.

[72] A. Goriachko, He, M. Knapp, H. Over, M. Corso, T. Brugger, S. Berner, J. Osterwalder, and T. Greber. Self-Assembly of a Hexagonal Boron Nitride Nanomesh on Ru(0001). *Langmuir*, 23(6):2928–2931, 2007.

[73] S. Berner, M. Corso, R. Widmer, O. Groening, R. Laskowski, P. Blaha, K. Schwarz, A. Goriachko, H. Over, S. Gsell, M. Schreck, H. Sachdev, T. Greber, and J. Osterwalder. Boron Nitride Nanomesh: Functionality from a Corrugated Monolayer. *Angewandte Chemie International Edition*, 46(27):5115–5119, 2007.

[74] S. Koch, M. Langer, S. Kawai, E. Meyer, and T. Glatzel. Contrast inversion of the h-BN nanomesh investigated by nc-AFM and Kelvin probe force microscopy. *Journal of Physics: Condensed Matter*, 24(31):314212, 2012.

[75] E. N. Voloshina, E. Fertitta, A. Garhofer, F. Mittendorfer, M. Fonin, A. Thissen, and Y. S. Dedkov. Electronic structure and imaging contrast of graphene moiré on metals. *Scientific Reports*, 3:1072, 2013.

[76] A. Preobrajenski, M. Nesterov, M. L. Ng, A. Vinogradov, and N. Mårtensson. Monolayer $h-$BN on lattice-mismatched metal surfaces: On the formation of the nanomesh. *Chemical Physics Letters*, 446(1):119 – 123, 2007.

[77] A. Nagashima, N. Tejima, Y. Gamou, T. Kawai, and C. Oshima. Electronic Structure of Monolayer Hexagonal Boron Nitride Physisorbed on Metal Surfaces. *Phys. Rev. Lett.*, 75:3918–3921, 1995.

[78] E. Rokuta, Y. Hasegawa, K. Suzuki, Y. Gamou, C. Oshima, and A. Nagashima. Phonon Dispersion of an Epitaxial Monolayer Film of Hexagonal Boron Nitride on Ni(111). *Phys. Rev. Lett.*, 79:4609–4612, 1997.

[79] P. Merino, M. Švec, A. L. Pinardi, G. Otero, and J. A. Martín-Gago. Strain-Driven Moiré Superstructures of Epitaxial Graphene on Transition Metal Surfaces. *ACS Nano*, 5(7):5627–5634, 2011.

[80] A. B. Preobrajenski, M. L. Ng, A. S. Vinogradov, and N. Mårtensson. Controlling graphene corrugation on lattice-mismatched substrates. *Phys. Rev. B*, 78:073401, 2008.

[81] D. Pacilé, P. Leicht, M. Papagno, P. M. Sheverdyaeva, P. Moras, C. Carbone, K. Krausert, L. Zielke, M. Fonin, Y. S. Dedkov, F. Mittendorfer, J. Doppler, A. Garhofer, and J. Redinger. Artificially lattice-mismatched graphene/metal interface: Graphene NiIr(111). *Phys. Rev. B*, 87:035420, 2013.

[82] G. Otero, C. González, A. L. Pinardi, P. Merino, S. Gardonio, S. Lizzit, M. Blanco-Rey, K. Van de Ruit, C. F. J. Flipse, J. Méndez, P. L. de Andrés, and J. A. Martín-Gago. Ordered Vacancy Network Induced by the Growth of Epitaxial Graphene on Pt(111). *Phys. Rev. Lett.*, 105:216102, 2010.

[83] D. Pudikov, E. Zhizhin, A. Rybkin, and A. Shikin. Graphene fabrication via carbon segregation through transition metal films. *Thin Solid Films*, 648:120 – 127, 2018.

[84] T. Brugger, S. Günther, B. Wang, J. H. Dil, M.-L. Bocquet, J. Osterwalder, J. Wintterlin, and T. Greber. Comparison of electronic structure and template function of single-layer graphene and a hexagonal boron nitride nanomesh on Ru(0001). *Phys. Rev. B*, 79:045407, 2009.

[85] B. Wang, M.-L. Bocquet, S. Marchini, S. Günther, and J. Wintterlin. Chemical origin of a graphene moiré overlayer on Ru(0001). *Physical Chemistry Chemical Physics*, 10(24):3530, 2008.

[86] S. Marchini, S. Günther, and J. Wintterlin. Scanning tunneling microscopy of graphene on Ru(0001). *Phys. Rev. B*, 76:075429, 2007.

[87] E. Sutter, D. P. Acharya, J. T. Sadowski, and P. Sutter. Scanning tunneling microscopy on epitaxial bilayer graphene on ruthenium (0001). *Applied Physics Letters*, 94(13):133101, 2009.

[88] S. J. Altenburg, J. Kröger, B. Wang, M.-L. Bocquet, N. Lorente, and R. Berndt. Graphene on Ru(0001): Contact Formation and Chemical Reactivity on the Atomic Scale. *Phys. Rev. Lett.*, 105:236101, 2010.

[89] J. Halle, N. Néel, and J. Kröger. Tailoring Intercalant Assemblies at the Graphene–Metal Interface. *Langmuir*, 35(7):2554–2560, 2019.

[90] J. Wintterlin and M.-L. Bocquet. Graphene on metal surfaces. *Surf. Sci.*, 603(10):1841 – 1852, 2009.

[91] K. F. McCarty, P. J. Feibelman, E. Loginova, and N. C. Bartelt. Kinetics and thermodynamics of carbon segregation and graphene growth on Ru(0001). *Carbon*, 47(7):1806–1813, 2009.

[92] E. McCann and M. Koshino. The electronic properties of bilayer graphene. *Reports on Progress in Physics*, 76(5):056503, 2013.

[93] K. S. Kim, A. L. Walter, L. Moreschini, T. Seyller, K. Horn, E. Rotenberg, and A. Bostwick. Coexisting massive and massless Dirac fermions in symmetry-broken bilayer graphene. *Nature Materials*, 12(10):887–892, 2013.

[94] A. V. Bommel, J. Crombeen, and A. V. Tooren. LEED and Auger electron observations of the SiC(0001) surface. *Surface Science*, 48(2):463–472, 1975.

[95] C. Riedl, C. Coletti, and U. Starke. Structural and electronic properties of epitaxial graphene on SiC(0 0 0 1): a review of growth, characterization, transfer doping and hydrogen intercalation. *Journal of Physics D: Applied Physics*, 43(37):374009, 2010.

[96] C. Oshima and A. Nagashima. Ultra-thin epitaxial films of graphite and hexagonal boron nitride on solid surfaces. *Journal of Physics: Condensed Matter*, 9(1):1–20, 1997.

[97] D. Usachov, V. K. Adamchuk, D. Haberer, A. Grüneis, H. Sachdev, A. B. Preobrajenski, C. Laubschat, and D. V. Vyalikh. Quasifreestanding single-layer hexagonal boron nitride as a substrate for graphene synthesis. *Physical Review B*, 82(7), 2010.

[98] M. Yankowitz, J. Xue, and B. J. LeRoy. Graphene on hexagonal boron nitride. *Journal of Physics: Condensed Matter*, 26(30):303201, 2014.

[99] C. R. Dean, A. F. Young, I. Meric, C. Lee, L. Wang, S. Sorgenfrei, K. Watanabe, T. Taniguchi, P. Kim, K. L. Shepard, and J. Hone. Boron nitride substrates for high-quality graphene electronics. *Nature Nanotechnology*, 5(10):722–726, 2010.

[100] J. Xue, J. Sanchez-Yamagishi, D. Bulmash, P. Jacquod, A. Deshpande, K. Watanabe, T. Taniguchi, P. Jarillo-Herrero, and B. J. LeRoy. Scanning tunnelling microscopy and spectroscopy of ultra-flat graphene on hexagonal boron nitride. *Nature Materials*, 10(4):282–285, 2011.

[101] R. Decker, Y. Wang, V. W. Brar, W. Regan, H.-Z. Tsai, Q. Wu, W. Gannett, A. Zettl, and M. F. Crommie. Local Electronic Properties of Graphene on a BN Substrate via Scanning Tunneling Microscopy. *Nano Letters*, 11(6):2291–2295, 2011.

[102] W. Yang, G. Chen, Z. Shi, C.-C. Liu, L. Zhang, G. Xie, M. Cheng, D. Wang, R. Yang, D. Shi, K. Watanabe, T. Taniguchi, Y. Yao, Y. Zhang, and G. Zhang. Epitaxial growth of single-domain graphene on hexagonal boron nitride. *Nature Materials*, 12(9):792–797, 2013.

[103] A. Nagashima, Y. Gamou, M. Terai, M. Wakabayashi, and C. Oshima. Electronic states of the heteroepitaxial double-layer system: Graphite/monolayer hexagonal boron nitride/Ni(111). *Physical Review B*, 54(19):13491–13494, 1996.

[104] C. Oshima, A. Itoh, E. Rokuta, T. Tanaka, K. Yamashita, and T. Sakurai. A hetero-epitaxial-double-atomic-layer system of monolayer graphene/monolayer h-BN on Ni(111). *Solid State Communications*, 116 (1):37–40, 2000.

[105] T. Kawasaki, T. Ichimura, H. Kishimoto, A. A. Akbar, T. Ogawa, and C. Oshima. Double atomic layers of graphene/monolayer h-BN on Ni(111) studied by scanning tunneling microscopy and scanning tunneling spectroscopy. *Surface Review and Letters*, 09(03n04):1459–1464, 2002.

[106] C. Bjelkevig, Z. Mi, J. Xiao, P. A. Dowben, L. Wang, W.-N. Mei, and J. A. Kelber. Electronic structure of a graphene/hexagonal-BN heterostructure grown on Ru(0001) by chemical vapor deposition and atomic layer deposition: extrinsically doped graphene. *Journal of Physics: Condensed Matter*, 22(30):302002, 2010.

[107] Z. Liu, L. Song, S. Zhao, J. Huang, L. Ma, J. Zhang, J. Lou, and P. M. Ajayan. Direct Growth of Graphene/Hexagonal Boron Nitride Stacked Layers. *Nano Letters*, 11(5):2032–2037, 2011.

[108] Q. Li, M. Liu, Y. Zhang, and Z. Liu. Hexagonal Boron Nitride-Graphene Heterostructures: Synthesis and Interfacial Properties. *Small*, 12(1):32–50, 2015.

[109] H. Wang, F. Liu, W. Fu, Z. Fang, W. Zhou, and Z. Liu. Two-dimensional heterostructures: fabrication, characterization, and application. *Nanoscale*, 6(21):12250–12272, 2014.

[110] X. Ding, G. Ding, X. Xie, F. Huang, and M. Jiang. Direct growth of few layer graphene on hexagonal boron nitride by chemical vapor deposition. *Carbon*, 49(7):2522–2525, 2011.

[111] M. Son, H. Lim, M. Hong, and H. C. Choi. Direct growth of graphene pad on exfoliated hexagonal boron nitride surface. *Nanoscale*, 3(8):3089, 2011.

[112] H. Arjmandi-Tash. In situ growth of graphene on hexagonal boron nitride for electronic transport applications. *Journal of Materials Chemistry C*, 8 (2):380–386, 2020.

[113] S. Tang, H. Wang, Y. Zhang, A. Li, H. Xie, X. Liu, L. Liu, T. Li, F. Huang, X. Xie, and M. Jiang. Precisely aligned graphene grown on hexagonal boron nitride by catalyst free chemical vapor deposition. *Scientific Reports*, 3(1), 2013.

[114] S. Tang, G. Ding, X. Xie, J. Chen, C. Wang, X. Ding, F. Huang, W. Lu, and M. Jiang. Nucleation and growth of single crystal graphene on hexagonal boron nitride. *Carbon*, 50(1):329–331, 2012.

[115] N. Mishra, V. Miseikis, D. Convertino, M. Gemmi, V. Piazza, and C. Coletti. Rapid and catalyst-free van der Waals epitaxy of graphene on hexagonal boron nitride. *Carbon*, 96:497–502, 2016.

[116] J. Halle, A. Mehler, N. Néel, and J. Kröger. Preparation of graphene bilayers on platinum by sequential chemical vapour deposition. *Phys. Chem. Chem. Phys.*, 21:3140–3144, 2019.

[117] S. W. Holman, R. R. Lawrence, and L. Barr. Melting Points of Aluminum, Silver, Gold, Copper, and Platinum. *Proceedings of the American Academy of Arts and Sciences*, 31:218, 1895.

[118] M. Garnica, M. Schwarz, J. Ducke, Y. He, F. Bischoff, J. V. Barth, W. Auwärter, and D. Stradi. Comparative study of the interfaces of graphene and hexagonal boron nitride with silver. *Physical Review B*, 94(15):155431, 2016.

[119] A. Goriachko, Y. B. He, and H. Over. Complex Growth of NanoAu on BN Nanomeshes Supported by Ru(0001). *The Journal of Physical Chemistry C*, 112(22):8147–8152, 2008.

[120] R. Drost, A. Uppstu, F. Schulz, S. K. Hämäläinen, M. Ervasti, A. Harju, and P. Liljeroth. Electronic States at the Graphene–Hexagonal Boron Nitride Zigzag Interface. *Nano Letters*, 14(9):5128–5132, 2014.

[121] M. Cattelan, B. Markman, G. Lucchini, P. K. Das, I. Vobornik, J. A. Robinson, S. Agnoli, and G. Granozzi. New Strategy for the Growth of Complex Heterostructures Based on Different 2D Materials. *Chemistry of Materials*, 27(11):4105–4113, 2015.

[122] W. Auwärter, M. Muntwiler, T. Greber, and J. Osterwalder. Co on h - BN/Ni(111): from island to island-chain formation and Co intercalation. *Surface Science*, 511(1-3):379–386, 2002.

[123] A. Fedorov, C. S. Praveen, N. I. Verbitskiy, D. Haberer, D. Usachov, D. V. Vyalikh, A. Nefedov, C. Wöll, L. Petaccia, S. Piccinin, H. Sachdev, M. Knupfer, B. Büchner, S. Fabris, and A. Grüneis. Efficient gating of epitaxial boron nitride monolayers by substrate functionalization. *Physical Review B*, 92(12):125440, 2015.

[124] Y. Zhang, Y. Zhang, D. Ma, Q. Ji, W. Fang, J. Shi, T. Gao, M. Liu, Y. Gao, Y. Chen, L. Xu, and Z. Liu. Mn atomic layers under inert covers of graphene and hexagonal boron nitride prepared on Rh(111). *Nano Research*, 6(12):887–896, 2013.

[125] N. I. Verbitskiy, A. V. Fedorov, G. Profeta, A. Stroppa, L. Petaccia, B. Senkovskiy, A. Nefedov, C. Wöll, D. Y. Usachov, D. V. Vyalikh, L. V. Yashina, A. A. Eliseev, T. Pichler, and A. Grüneis. Atomically precise semiconductor—graphene and hBN interfaces by Ge intercalation. *Scientific Reports*, 5(1):17700, 2015.

[126] M. Will, N. Atodiresei, V. Caciuc, P. Valerius, C. Herbig, and T. Michely. A Monolayer of Hexagonal Boron Nitride on Ir(111) as a Template for Cluster Superlattices. *ACS Nano*, 12(7):6871–6880, 2018.

[127] X. Feng, S. Maier, and M. Salmeron. Water Splits Epitaxial Graphene and Intercalates. *Journal of the American Chemical Society*, 134(12):5662–5668, 2012.

[128] G. Kresse and J. Hafner. Norm-conserving and ultrasoft pseudopotentials for first-row and transition elements. *Journal of Physics: Condensed Matter*, 6(40):8245–8257, 1994.

[129] G. Kresse and J. Furthmüller. Efficient iterative schemes forab initiototal-energy calculations using a plane-wave basis set. *Physical Review B*, 54 (16):11169–11186, 1996.

[130] J. P. Perdew, K. Burke, and M. Ernzerhof. Generalized Gradient Approximation Made Simple. *Physical Review Letters*, 77(18):3865–3868, 1996.

[131] P. E. Blöchl. Projector augmented-wave method. *Physical Review B*, 50 (24):17953–17979, 1994.

[132] S. Grimme. Semiempirical GGA-type density functional constructed with a long-range dispersion correction. *Journal of Computational Chemistry*, 27(15):1787–1799, 2006.

[133] A. R. Sandy, S. G. J. Mochrie, D. M. Zehner, G. Grübel, K. G. Huang, and D. Gibbs. Reconstruction of the Pt(111) surface. *Physical Review Letters*, 68(14):2192–2195, 1992.

[134] G. Grübel, K. G. Huang, D. Gibbs, D. M. Zehner, A. R. Sandy, and S. G. J. Mochrie. Reconstruction of the Pt(111) surface: X-ray-scattering measurements. *Physical Review B*, 48(24):18119–18139, 1993.

[135] M. Bott, M. Hohage, T. Michely, and G. Comsa. Pt(111) reconstruction induced by enhanced Pt gas-phase chemical potential. *Physical Review Letters*, 70(10):1489–1492, 1993.

[136] M. Hohage, T. Michely, and G. Comsa. Pt(111) network reconstruction: structure, growth and decay. *Surface Science*, 337(3):249–267, 1995.

[137] J. Halle, N. Néel, and J. Kröger. Filling the Gap: Li-Intercalated Graphene on Ir(111). *The Journal of Physical Chemistry C*, 120(9):5067–5073, 2016.

[138] C. Virojanadara, S. Watcharinyanon, A. A. Zakharov, and L. I. Johansson. Epitaxial graphene on6H-SiCand Li intercalation. *Physical Review B*, 82 (20), 2010.

[139] H. W. Kim, W. Ko, J. Ku, I. Jeon, D. Kim, H. Kwon, Y. Oh, S. Ryu, Y. Kuk, S. W. Hwang, and H. Suh. Nanoscale control of phonon excitations in graphene. *Nature Communications*, 6(7528), 2015.

[140] N. Néel, C. Steinke, T. O. Wehling, and J. Kröger. Inelastic electron tunneling into graphene nanostructures on a metal surface. *Physical Review B*, 95(16):161410, 2017.

[141] G. J. Slotman, G. A. de Wijs, A. Fasolino, and M. I. Katsnelson. Phonons and electron-phonon coupling in graphene-h-BN heterostructures. *Annalen der Physik*, 526(9-10):381–386, 2014.

[142] M. Endlich, A. Molina-Sánchez, L. Wirtz, and J. Kröger. Screening of electron-phonon coupling in graphene on Ir(111). *Physical Review B*, 88 (20):205403, 2013.

[143] S. Jung, M. Park, J. Park, T.-Y. Jeong, H.-J. Kim, K. Watanabe, T. Taniguchi, D. H. Ha, C. Hwang, and Y.-S. Kim. Vibrational Properties of h-BN and h-BN-Graphene Heterostructures Probed by Inelastic Electron Tunneling Spectroscopy. *Scientific Reports*, 5(1):16642, 2015.

[144] G. S. N. Eliel, M. V. O. Moutinho, A. C. Gadelha, A. Righi, L. C. Campos, H. B. Ribeiro, P.-W. Chiu, K. Watanabe, T. Taniguchi, P. Puech, M. Paillet, T. Michel, P. Venezuela, and M. A. Pimenta. Intralayer and interlayer

electron–phonon interactions in twisted graphene heterostructures. *Nature Communications*, 9(1):1221, 2018.

[145] A. Righi, S. D. Costa, H. Chacham, C. Fantini, P. Venezuela, C. Magnuson, L. Colombo, W. S. Bacsa, R. S. Ruoff, and M. A. Pimenta. Graphene Moiré patterns observed by umklapp double-resonance Raman scattering. *Physical Review B*, 84(24):241409, 2011.

[146] V. Carozo, C. M. Almeida, E. H. M. Ferreira, L. G. Cançado, C. A. Achete, and A. Jorio. Raman Signature of Graphene Superlattices. *Nano Letters*, 11:4527–4534, 2011.

[147] A. Righi, P. Venezuela, H. Chacham, S. D. Costa, C. Fantini, R. S. Ruoff, L. Colombo, W. S. Bacsa, and M. A. Pimenta. Resonance Raman spectroscopy in twisted bilayer graphene. *Solid State Communications*, 175-176: 13–17, 2013.

[148] V. Carozo, C. M. Almeida, B. Fragneaud, P. M. Bedê, M. V. O. Moutinho, J. Ribeiro-Soares, N. F. Andrade, A. G. S. Filho, M. J. S. Matos, B. Wang, M. Terrones, R. B. Capaz, A. Jorio, C. A. Achete, and L. G. Cançado. Resonance effects on the Raman spectra of graphene superlattices. *Physical Review B*, 88(8):085401, 2013.

[149] H.-Q. Song, Z. Liu, and D.-B. Zhang. Interlayer vibration of twisted bilayer graphene: A first-principles study. *Physics Letters A*, 383:2628–2632, 2019.

[150] J. Halle, N. Néel, M. Fonin, M. Brandbyge, and J. Kröger. Understanding and Engineering Phonon-Mediated Tunneling into Graphene on Metal Surfaces. *Nano Letters*, 18(9):5697–5701, 2018.

[151] H. C. Manoharan, C. P. Lutz, and D. M. Eigler. Quantum mirages formed by coherent projection of electronic structure. *Nature*, 403(6769):512–515, 2000.

[152] Q. Li, X. Li, B. Miao, L. Sun, G. Chen, P. Han, and H. Ding. Kondo-free mirages in elliptical quantum corrals. *Nature Communications*, 11(1):1400, 2020.

[153] J. W. Gadzuk and M. Plihal. Quantum mirages in scanning tunneling spectroscopy of Kondo adsorbates: Vibrational signatures. *Physical Review B*, 68(23):235413, 2003.

[154] T. Frederiksen, K. J. Franke, A. Arnau, G. Schulze, J. I. Pascual, and N. Lorente. Dynamic Jahn-Teller effect in electronic transport through single C_{60} molecules. *Phys. Rev. B*, 78:233401, 2008.

[155] Y. Wang, J. Kröger, R. Berndt, and H. Tang. Molecular Nanocrystals on Ultrathin NaCl Films on Au(111). *Journal of the American Chemical Society*, 132(36):12546–12547, 2010.

[156] F. Matino, G. Schull, F. Köhler, S. Gabutti, M. Mayor, and R. Berndt. Electronic decoupling of a cyclophane from a metal surface. *Proceedings of the National Academy of Sciences*, 108(3):961–964, 2011.

[157] T. P. A. Ruberu, H. R. Albright, B. Callis, B. Ward, J. Cisneros, H.-J. Fan, and J. Vela. Molecular Control of the Nanoscale: Effect of Phosphine–Chalcogenide Reactivity on CdS–CdSe Nanocrystal Composition and Morphology. *ACS Nano*, 6(6):5348–5359, 2012. PMID: 22519805.

[158] F. Schulz, R. Drost, S. K. Hämäläinen, and P. Liljeroth. Templated Self-Assembly and Local Doping of Molecules on Epitaxial Hexagonal Boron Nitride. *ACS Nano*, 7(12):11121–11128, 2013.

[159] N. Pavliček, I. Swart, J. Niedenführ, G. Meyer, and J. Repp. Symmetry Dependence of Vibration-Assisted Tunneling. *Phys. Rev. Lett.*, 110:136101, 2013.

[160] N. Hauptmann, C. Hamann, H. Tang, and R. Berndt. Soft-Landing Electrospray Deposition of the Ruthenium Dye N3 on Au(111). *The Journal of Physical Chemistry C*, 117(19):9734–9738, 2013.

[161] F. Schwarz, Y. F. Wang, W. A. Hofer, R. Berndt, E. Runge, and J. Kröger. Electronic and Vibrational States of Single Tin-Phthalocyanine Molecules in Double Layers on Ag(111). *The Journal of Physical Chemistry C*, 119 (27):15716–15722, 2015.

[162] E. Tsiper, Z. Soos, W. Gao, and A. Kahn. Electronic polarization at surfaces and thin films of organic molecular crystals: PTCDA. *Chemical Physics Letters*, 360(1):47 – 52, 2002.

[163] S. Berner, M. de Wild, L. Ramoino, S. Ivan, A. Baratoff, H.-J. Güntherodt, H. Suzuki, D. Schlettwein, and T. A. Jung. Adsorption and two-dimensional phases of a large polar molecule: Sub-phthalocyanine on Ag(111). *Phys. Rev. B*, 68:115410, 2003.

[164] T. Schwieger, H. Peisert, and M. Knupfer. Direct observation of interfacial charge transfer from silver to organic semiconductors. *Chemical Physics Letters*, 384(4):197 – 202, 2004.

[165] J. Repp, G. Meyer, S. M. Stojković, A. Gourdon, and C. Joachim. Molecules on Insulating Films: Scanning-Tunneling Microscopy Imaging of Individual Molecular Orbitals. *Phys. Rev. Lett.*, 94:026803, 2005.

[166] J. Repp, G. Meyer, F. E. Olsson, and M. Persson. Controlling the Charge State of Individual Gold Adatoms. *Science*, 305(5683):493–495, 2004.

[167] Y. Wang, R. Yamachika, A. Wachowiak, M. Grobis, and M. F. Crommie. Tuning fulleride electronic structure and molecular ordering via variable layer index. *Nat. Mater.*, 7:194 – 197, 2008.

[168] Y. Wang, J. Kröger, R. Berndt, and W. Hofer. Structural and Electronic Properties of Ultrathin Tin–Phthalocyanine Films on Ag(111) at the Single-Molecule Level. *Angewandte Chemie International Edition*, 48 (7):1261–1265, 2009.

[169] M. Häming, C. Scheuermann, A. Schöll, F. Reinert, and E. Umbach. Coverage dependent organic–metal interaction studied by high-resolution core level spectroscopy: SnPc (sub)monolayers on Ag(111). *Journal of Electron Spectroscopy and Related Phenomena*, 174(1):59 – 64, 2009.

[170] T. G. Gopakumar, T. Brumme, J. Kröger, C. Toher, G. Cuniberti, and R. Berndt. Coverage-Driven Electronic Decoupling of Fe-Phthalocyanine from a Ag(111) Substrate. *The Journal of Physical Chemistry C*, 115(24): 12173–12179, 2011.

[171] A. J. Heinrich, J. A. Gupta, C. P. Lutz, and D. M. Eigler. Single-Atom Spin-Flip Spectroscopy. *Science*, 306(5695):466–469, 2004.

[172] C. F. Hirjibehedin, C. P. Lutz, and A. J. Heinrich. Spin Coupling in Engineered Atomic Structures. *Science*, 312(5776):1021–1024, 2006.

[173] C. F. Hirjibehedin, C.-Y. Lin, A. F. Otte, M. Ternes, C. P. Lutz, B. A. Jones, and A. J. Heinrich. Large Magnetic Anisotropy of a Single Atomic Spin Embedded in a Surface Molecular Network. *Science*, 317(5842):1199–1203, 2007.

[174] A. F. Otte, M. Ternes, K. von Bergmann, S. Loth, H. Brune, C. P. Lutz, C. F. Hirjibehedin, and A. J. Heinrich. The role of magnetic anisotropy in the Kondo effect. *Nature Physics*, 4:847 – 850, 2008.

[175] A. F. Otte, M. Ternes, S. Loth, C. P. Lutz, C. F. Hirjibehedin, and A. J. Heinrich. Spin Excitations of a Kondo-Screened Atom Coupled to a Second Magnetic Atom. *Phys. Rev. Lett.*, 103:107203, 2009.

[176] S. Baumann, W. Paul, T. Choi, C. P. Lutz, A. Ardavan, and A. J. Heinrich. Electron paramagnetic resonance of individual atoms on a surface. *Science*, 350(6259):417–420, 2015.

[177] P. Willke, Y. Bae, K. Yang, J. L. Lado, A. Ferrón, T. Choi, A. Ardavan, J. Fernández-Rossier, A. J. Heinrich, and C. P. Lutz. Hyperfine interaction of individual atoms on a surface. *Science*, 362(6412):336–339, 2018.

[178] E. Ćavar, M.-C. Blüm, M. Pivetta, F. Patthey, M. Chergui, and W.-D. Schneider. Fluorescence and Phosphorescence from Individual C_{60} Molecules Excited by Local Electron Tunneling. *Phys. Rev. Lett.*, 95: 196102, 2005.

[179] Z. C. Dong, X. L. Zhang, H. Y. Gao, Y. Luo, C. Zhang, L. G. Chen, R. Zhang, X. Tao, Y. Zhang, J. L. Yang, and J. G. Hou. Generation of molecular hot electroluminescence by resonant nanocavity plasmons. *Nature Photonics*, 4:50–54, 2009.

[180] C. Chen, P. Chu, C. A. Bobisch, D. L. Mills, and W. Ho. Viewing the Interior of a Single Molecule: Vibronically Resolved Photon Imaging at Submolecular Resolution. *Phys. Rev. Lett.*, 105:217402, 2010.

[181] Y. Zhang, Y. Luo, Y. Zhang, Y.-J. Yu, Y.-M. Kuang, L. Zhang, Q.-S. Meng, Y. Luo, J.-L. Yang, Z.-C. Dong, and J. G. Hou. Visualizing coherent intermolecular dipole-dipole coupling in real space. *Nature*, 531:623–627, 2016.

[182] B. Doppagne, M. C. Chong, E. Lorchat, S. Berciaud, M. Romeo, H. Bulou, A. Boeglin, F. Scheurer, and G. Schull. Vibronic Spectroscopy with Submolecular Resolution from STM-Induced Electroluminescence. *Phys. Rev. Lett.*, 118:127401, 2017.

[183] Y. Zhang, Q.-S. Meng, L. Zhang, Y. Luo, Y.-J. Yu, B. Yang, Y. Zhang, R. Esteban, J. Aizpurua, Y. Luo, J.-L. Yang, Z.-C. Dong, and J. G.

Hou. Sub-nanometre control of the coherent interaction between a single molecule and a plasmonic nanocavity. *Nature Communications*, 8:15225, 2017.

[184] H. Imada, K. Miwa, M. Imai-Imada, S. Kawahara, K. Kimura, and Y. Kim. Single-Molecule Investigation of Energy Dynamics in a Coupled Plasmon-Exciton System. *Phys. Rev. Lett.*, 119:013901, 2017.

[185] J. Kröger, B. Doppagne, F. Scheurer, and G. Schull. Fano Description of Single-Hydrocarbon Fluorescence Excited by a Scanning Tunneling Microscope. *Nano Letters*, 18(6):3407–3413, 2018.

[186] B. Doppagne, M. C. Chong, H. Bulou, A. Boeglin, F. Scheurer, and G. Schull. Electrofluorochromism at the single-molecule level. *Science*, 361(6399):251–255, 2018.

[187] G. Chen, Y. Luo, H. Gao, J. Jiang, Y. Yu, L. Zhang, Y. Zhang, X. Li, Z. Zhang, and Z. Dong. Spin-Triplet-Mediated Up-Conversion and Crossover Behavior in Single-Molecule Electroluminescence. *Phys. Rev. Lett.*, 122:177401, 2019.

[188] K. Kimura, K. Miwa, H. Imada, M. Imai-Imada, S. Kawahara, J. Takeya, M. Kawai, M. Galperin, and Y. Kim. Selective triplet exciton formation in a single molecule. *Nature*, 570:210 – 213, 2019.

[189] P. Liljeroth, J. Repp, and G. Meyer. Current-Induced Hydrogen Tautomerization and Conductance Switching of Naphthalocyanine Molecules. *Science*, 317(5842):1203–1206, 2007.

[190] F. Donati, Q. Dubout, G. Autès, F. Patthey, F. Calleja, P. Gambardella, O. V. Yazyev, and H. Brune. Magnetic Moment and Anisotropy of Individual Co Atoms on Graphene. *Phys. Rev. Lett.*, 111:236801, 2013.

[191] S. J. Altenburg and R. Berndt. Tungsten–hydrogen complexes on graphene on Ir(111). *New Journal of Physics*, 16(9):093047, 2014.

[192] S. J. Altenburg, M. Lattelais, B. Wang, M.-L. Bocquet, and R. Berndt. Reaction of Phthalocyanines with Graphene on Ir(111). *Journal of the American Chemical Society*, 137(29):9452–9458, 2015.

[193] N. Néel, M. Lattelais, M.-L. Bocquet, and J. Kröger. Depopulation of Single-Phthalocyanine Molecular Orbitals upon Pyrrolic-Hydrogen Abstraction on Graphene. *ACS Nano*, 10(2):2010–2016, 2016.

[194] J. Cho, J. Smerdon, L. Gao, z. Süzer, J. R. Guest, and N. P. Guisinger. Structural and Electronic Decoupling of C_{60} from Epitaxial Graphene on SiC. *Nano Letters*, 12(6):3018–3024, 2012.

[195] M. Scardamaglia, S. Lisi, S. Lizzit, A. Baraldi, R. Larciprete, C. Mariani, and M. G. Betti. Graphene-Induced Substrate Decoupling and Ideal Doping of a Self-Assembled Iron-phthalocyanine Single Layer. *The Journal of Physical Chemistry C*, 117(6):3019–3027, 2013.

[196] W. Dou, S. Huang, R. Q. Zhang, and C. S. Lee. Molecule–substrate interaction channels of metal-phthalocyanines on graphene on Ni(111) surface. *The Journal of Chemical Physics*, 134(9):094705, 2011.

[197] Y. Wang, K. Wu, J. Kröger, and R. Berndt. Review Article: Structures of phthalocyanine molecules on surfaces studied by STM. *AIP Advances*, 2 (4):041402, 2012.

[198] M. Endlich, S. Gozdzik, N. Néel, A. L. da Rosa, T. Frauenheim, T. O. Wehling, and J. Kröger. Phthalocyanine adsorption to graphene on Ir(111): Evidence for decoupling from vibrational spectroscopy. *The Journal of Chemical Physics*, 141(18):184308, 2014.

[199] G. Rouillé, T. Kirchhuebel, M. Rink, M. Gruenewald, J. Kröger, R. Forker, and T. Fritz. Identification of vibrational excitations and optical transitions of the organic electron donor tetraphenyldibenzoperiflanthene (DBP). *Phys. Chem. Chem. Phys.*, 17:30404–30416, 2015.

[200] T. Kirchhuebel, M. Gruenewald, F. Sojka, S. Kera, F. Bussolotti, T. Ueba, N. Ueno, G. Rouillé, R. Forker, and T. Fritz. Self-Assembly of Tetraphenyldibenzoperiflanthene (DBP) Films on Ag(111) in the Monolayer Regime. *Langmuir*, 32(8):1981–1987, 2016. PMID: 26844381.

[201] J. Kröger, H. Jensen, R. Berndt, R. Rurali, and N. Lorente. Molecular orbital shift of perylenetetracarboxylic-dianhydride on gold. *Chem. Phys. Lett.*, 438(4):249 – 253, 2007.

[202] L. Limot, T. Maroutian, P. Johansson, and R. Berndt. Surface-State Stark Shift in a Scanning Tunneling Microscope. *Phys. Rev. Lett.*, 91:196801, 2003.

[203] J. Kröger, L. Limot, H. Jensen, R. Berndt, and P. Johansson. Stark effect in Au(111) and Cu(111) surface states. *Phys. Rev. B*, 70:033401, 2004.

[204] F. Schulz, R. Drost, S. K. Hämäläinen, T. Demonchaux, A. P. Seitsonen, and P. Liljeroth. Epitaxial hexagonal boron nitride on Ir(111): A work function template. *Phys. Rev. B*, 89:235429, 2014.

[205] H. Ishii, K. Sugiyama, E. Ito, and K. Seki. Energy Level Alignment and Interfacial Electronic Structures at Organic/Metal and Organic/Organic Interfaces. *Advanced Materials*, 11(8):605–625, 1999.

[206] M. Gao, Y. Pan, L. Huang, H. Hu, L. Z. Zhang, H. M. Guo, S. X. Du, and H.-J. Gao. Epitaxial growth and structural property of graphene on Pt(111). *Applied Physics Letters*, 98(3):033101, 2011.

[207] Z. Liang, H. Khosravian, A. Uhl, R. J. Meyer, and M. Trenary. Graphene domain boundaries on Pt(111) as nucleation sites for Pt nanocluster formation. *Surface Science*, 606(21):1643 – 1648, 2012.

[208] H. Dil, J. Lobo-Checa, R. Laskowski, P. Blaha, S. Berner, J. Osterwalder, and T. Greber. Surface Trapping of Atoms and Molecules with Dipole Rings. *Science*, 319(5871):1824–1826, 2008.

[209] M. Ziegler, N. Néel, A. Sperl, J. Kröger, and R. Berndt. Local density of states from constant-current tunneling spectra. *Phys. Rev. B*, 80:125402, 2009.

[210] J. Gómez Díaz, Y. Ding, R. Koitz, A. P. Seitsonen, M. Iannuzzi, and J. Hutter. Hexagonal boron nitride on transition metal surfaces. *Theoretical Chemistry Accounts*, 132(4):1350, 2013.

[211] M. Hirade and C. Adachi. Small molecular organic photovoltaic cells with exciton blocking layer at anode interface for improved device performance. *Appl. Phys. Lett.*, 99(15):153302, 2011.

[212] X. Xiao, J. D. Zimmerman, B. E. Lassiter, K. J. Bergemann, and S. R. Forrest. A hybrid planar-mixed tetraphenyldibenzoperiflanthene C_{70} photovoltaic cell. *Applied Physics Letters*, 102(7):073302, 2013.

[213] Y.-q. Zheng, W. J. Potscavage Jr, T. Komino, M. Hirade, J. Adachi, and C. Adachi. Highly efficient bulk heterojunction photovoltaic cells based on C_{70} and tetraphenyldibenzoperiflanthene. *Appl. Phys. Lett.*, 102(14): 143304, 2013.

[214] C.-W. Chen, Z.-Y. Huang, Y.-M. Lin, W.-C. Huang, Y.-H. Chen, J. Strzalka, A. Y. Chang, R. D. Schaller, C.-K. Lee, and C.-W. Pao. Morphology, molecular stacking, dynamics and device performance correlations of vacuum-deposited small-molecule organic solar cells. *Phys. Chem. Chem. Phys.*, 16(19):8852–8864, 2014.

[215] H. Nakanotani, T. Higuchi, T. Furukawa, K. Masui, K. Morimoto, M. Numata, H. Tanaka, Y. Sagara, T. Yasuda, and C. Adachi. High-efficiency organic light-emitting diodes with fluorescent emitters. *Nat. Commun.*, 5: 4016, 2014.

[216] D. Maccariello, M. Garnica, M. A. Niño, C. Navío, P. Perna, S. Barja, A. L. Vázquez de Parga, and R. Miranda. Spatially Resolved, Site-Dependent Charge Transfer and Induced Magnetic Moment in TCNQ Adsorbed on Graphene. *Chemistry of Materials*, 26(9):2883–2890, 2014.

[217] H. G. Zhang, J. T. Sun, T. Low, L. Z. Zhang, Y. Pan, Q. Liu, J. H. Mao, H. T. Zhou, H. M. Guo, S. X. Du, F. Guinea, and H.-J. Gao. Assembly of iron phthalocyanine and pentacene molecules on a graphene monolayer grown on Ru(0001). *Phys. Rev. B*, 84:245436, 2011.

[218] F. Himpsel, K. Christmann, P. Heimann, D. Eastman, and P. J. Feibelman. Adsorbate band dispersions for C on Ru(0001). *Surface Science*, 115(3): L159 – L164, 1982.

[219] P. Sutter, J. T. Sadowski, and E. Sutter. Graphene on Pt(111): Growth and substrate interaction. *Phys. Rev. B*, 80:245411, 2009.

[220] N. Srivastava, Q. Gao, M. Widom, R. M. Feenstra, S. Nie, K. F. McCarty, and I. V. Vlassiouk. Low-energy electron reflectivity of graphene on copper and other substrates. *Phys. Rev. B*, 87:245414, 2013.

[221] S. J. Altenburg and R. Berndt. Local work function and STM tip-induced distortion of graphene on Ir(111). *New Journal of Physics*, 16(5):053036, 2014.

[222] A. B. Preobrajenski, S. A. Krasnikov, A. S. Vinogradov, M. L. Ng, T. Käämbre, A. A. Cafolla, and N. Mårtensson. Adsorption-induced gap states of $h-$BN on metal surfaces. *Phys. Rev. B*, 77:085421, 2008.

[223] I. I. Klimovskikh, M. M. Otrokov, V. Y. Voroshnin, D. Sostina, L. Petaccia, G. Di Santo, S. Thakur, E. V. Chulkov, and A. M. Shikin. Spin–Orbit

Coupling Induced Gap in Graphene on Pt(111) with Intercalated Pb Monolayer. *ACS Nano*, 11(1):368–374, 2017.

[224] D. Usachov, A. Fedorov, O. Vilkov, V. K. Adamchuk, L. V. Yashina, L. Bondarenko, A. A. Saranin, A. Grüneis, and D. V. Vyalikh. Experimental and computational insight into the properties of the lattice-mismatched structures: Monolayers of *h*-BN and graphene on Ir(111). *Phys. Rev. B*, 86:155151, 2012.

[225] L. Kong, A. Enders, T. S. Rahman, and P. A. Dowben. Molecular adsorption on graphene. *Journal of Physics: Condensed Matter*, 26(44):443001, 2014.

[226] C. Elias, P. Valvin, T. Pelini, A. Summerfield, C. J. Mellor, T. S. Cheng, L. Eaves, C. T. Foxon, P. H. Beton, S. V. Novikov, B. Gil, and G. Cassabois. Direct band-gap crossover in epitaxial monolayer boron nitride. *Nature Communications*, 10:2639, 2019.

[227] I. Meric, M. Y. Han, A. F. Young, B. Ozyilmaz, P. Kim, and K. L. Shepard. Current saturation in zero-bandgap, top-gated graphene field-effect transistors. *Nature Nanotechnology*, 3:654 – 659, 2008.

[228] D. Martoccia, T. Brugger, M. Björck, C. Schlepütz, S. Pauli, T. Greber, B. Patterson, and P. Willmott. h-BN/Ru(0001) nanomesh: A 14-on-13 superstructure with 3.5nm periodicity. *Surface Science*, 604(5):L16 – L19, 2010.

[229] J. Lu, P. S. E. Yeo, Y. Zheng, H. Xu, C. K. Gan, M. B. Sullivan, A. Castro Neto, and K. P. Loh. Step Flow Versus Mosaic Film Growth in Hexagonal Boron Nitride. *Journal of the American Chemical Society*, 135(6): 2368–2373, 2013.

[230] Q. Zhang, Y. Chen, C. Zhang, C.-R. Pan, M.-Y. Chou, C. Zeng, and C.-K. Shih. Bandgap renormalization and work function tuning in MoSe2/hBN/Ru(0001) heterostructures. *Nature Communications*, 7: 13843, 2016.

[231] A. Mehler, N. Néel, and J. Kröger. Probing site-dependent decoupling of hexagonal boron nitride with molecular frontier orbitals. *Journal of Vacuum Science & Technology A*, 37(6):061404, 2019.

[232] K. Huang, A. Rhys, and N. F. Mott. Theory of light absorption and non-radiative transitions in F-centres. *Proceedings of the Royal Society of London. Series A. Mathematical and Physical Sciences*, 204(1078):406–423, 1950.

[233] N. A. Pradhan, N. Liu, and W. Ho. Vibronic Spectroscopy of Single C60 Molecules and Monolayers with the STM. *The Journal of Physical Chemistry B*, 109(17):8513–8518, 2005.

[234] H. J. Lee, J. H. Lee, and W. Ho. Vibronic Transitions in Single Metalloporphyrins. *ChemPhysChem*, 6(5):971–975, 2005.

[235] N. Ogawa, G. Mikaelian, and W. Ho. Spatial Variations in Submolecular Vibronic Spectroscopy on a Thin Insulating Film. *Phys. Rev. Lett.*, 98: 166103, 2007.

[236] J. G. Simmons. Generalized Formula for the Electric Tunnel Effect between Similar Electrodes Separated by a Thin Insulating Film. *Journal of Applied Physics*, 34(6):1793–1803, 1963.

[237] J. G. Simmons. Electric Tunnel Effect between Dissimilar Electrodes Separated by a Thin Insulating Film. *Journal of Applied Physics*, 34(9):2581–2590, 1963.

[238] V. A. Ukraintsev. Data evaluation technique for electron-tunneling spectroscopy. *Phys. Rev. B*, 53:11176–11185, 1996.

Danksagung

Zum Schluss möchte ich mich bei allen Personen bedanken, die mich während der Arbeit an dieser Dissertation unterstützt haben. Mein besonderer Dank gilt dabei Prof. Dr. Jörg Kröger, der mir mit dem Angebot der Promotion die Bearbeitung dieses Themas möglich gemacht hat. Außerdem stand er mir durch die stets sehr gute Betreuung und Hilfe bei jeglichen Fragen zur Seite.

Prof. Dr. Yuriy Dedkov danke ich für die Übernahme eines der Gutachten, sowie für die Unterstützung bei der Interpretation der Heterostrukturen aus Graphen und h-BN in Zusammenarbeit mit Prof. Dr. Elena Voloshina. Weiter danke ich Prof. Dr. Stefan Krischok für die bereitwillige Übernahme eines weiteren Gutachtens dieser Dissertation.

Bei der Arbeitsgruppe Experimentalphysik I möchte ich mich für die stets gute Zusammenarbeit und ertragreichen Diskussionen bedanken. Dabei ist besonders Dr. Nicolas Néel zu nennen, der mir egal ob im Büro oder im Labor immer seine bestmögliche Unterstüzung zukommen lassen hat. Bei den ehemaligen und aktuellen Doktoranden Johannes Halle, Jonathan Brand und Maryam Omidian bedanke ich mich für das stets gute Miteinander während und auch abseits der Arbeit.

Meiner Familie und meinen Freunden danke ich für die bedingungslose Unterstützung während der Anfertigung dieser Dissertation. Ohne sie wäre dieses Projekt nicht möglich gewesen.